FACULTY OF SCIENCE
UNIVERSITY OF COPENHAGEN

PhD Thesis

Nanowire Growth for Photovoltaics

Jeppe Vilstrup Holm

This thesis has been submitted to the PhD School of The Faculty of Science, University of Copenhagen

Academic advisor

Prof. Dr. Jesper Nygård

Referees

Prof. Dr. Helge Weman

Dr. Magnus Borgström

Dr. Søren Stobbe

Submitted

12.09.2013

Contents

1. Introduction

1.1. Abstract

Solar cells commercial success is based on an efficiency/cost calculation. Nanowire solar cells is one of the foremost candidates to implement third generation photo voltaics, which are both very efficient and cheap to produce.

By increasing the number of junctions in solar cells, they can extract more energy per absorbed photon. In ideal multi junction (MJ) solar cells each junction absorb the same number of photons. Current MJ solar cells efficiency is hampered by the fact combining the most complimentary materials, from an absorption standpoint, is impossible due to mismatches in the crystal structure. Nanowires solve this problem, since the small footprint of grown nanowires relaxes the crystal matching constraint. Resonance effects between the light and nanowire causes an inherent concentration of the sunlight into the nanowires, and means that a sparse array of nanowires (less than 5% of the area) can absorb all the incoming light. The resonance effects, as well as a graded index of refraction, also traps the light. The concentration and light trapping means that single junction nanowire solar cells have a higher theoretical maximum efficiency than equivalent planar solar cells, and the crystal growth ability makes the difference even larger for MJ solar cells.

In order to fabricate, characterize, and improve the quality of the nanowire solar cells knowledge of how solar cells function is essential. The interaction between light and semiconductors is described, as well as how a pn-junction works to separate the generated carriers, and some of the important loss processes are discussed.

Nanowire growth is a thin, vertical specialization of normal planar crystal growth. The elementary crystal growth processes adsorption, diffusion, incorporation and nucleation are described with a basis in planar molecular beam epitaxy(MBE).

The strategies that can be used to grow semiconductor nanowires, and the most

used techniques that utilize these strategies are described, with a focus on catalyzed nanowire growth. Heterostructures, both material and doped, are vital for the successful implementation of nanowire solar cells. Both axial and radial heterostructures are discussed with an emphasis on the opportunities and problems they present for nanowire growth.

The current status of nanowire solar cells is discussed beginning with a summary of our own publications.

We have demonstrated the built-in light concentration of nanowires, by growing, contacting and characterizing a solar cell consisting of a single, vertical, gallium arsenide(GaAs) nanowire grown on silicon with a radial p-i-n-junction. The average concentration was ~8, and the peak concentration was ~12.

We have demonstrated how to incorporate phosphorous(P) into Ga-catalyzed nanowire growth, and grown $GaAs_{1-x}P_x$ nanowires with different inclusions of P(x). The incorporation of P was generally higher in nanowires than for planar growth at identical P flux percentage. More interestingly, the percentage of P in the nanowire was found to be a concave function of the percentage of P in the flux, while for planar growth it was a convex function.

1.7eV is the ideal bandgap for a top junction in a dual junction solar cell, where silicon is the bottom junction. This can be obtained with $GaAs_{0.8}P_{0.2}$. We have demonstrated GaAsP nanowires with this composition and further grown a shell surrounding the core with the same composition. The lattice matched GaAsP core-shell nanowire were doped to produce radial p-i-n junctions in each of the nanowires, some of which were removed from their growth substrate and turned into single nanowire solar cells (SNWSC). The best device showed a conversion efficiency of 6.8% under 1.5AMG 1-sun illumination. In order to improve the efficiency a surface passivating shell consisting of highly doped, wide bandgap indium gallium phosphide was grown. The best SNWSC from this batch had an efficiency of 10.2%.

Harvested nanowire solar cells are not the goal, but merely a steppingstone on the way to real solar cells. For nanowire solar cells this means billions of identical vertical nanowires in a large array. This yields new challenges as the nanowires needs to be put into a circuit, and the generated current efficiency extracted. The state of the art is discussed, with a focus on currently employed strategies and the advantages and problems they present.

1.2. Resumé på dansk

Kommercielle solcellers succes er baseret på en effektivitets/pris beregning. Nanotrådssolceller er en af topkandidaterne til at implementerer 3. generations solceller, der både er meget effektive og billige at producere.

Ved at forøge antallet af delceller i solcellen, i såkaldte multi-junction (MJ) solceller, kan der trækkes mere energi ud af hver absorberede photon. I ideelle MJ solceller absorberer hver delcelle det samme antal photoner. Nuværende MJ solcellers effektivitet er dog begrænset af at de materialer der komplimenterer hinanden absorptionsmæssigt ikke kan sættes sammen på grund af forskelle i krystalstrukturen. Nanotråde løser dette problem, da deres lille bundareal slækker kravet om perfekt krystalmatch. Resonanseffekter mellem lys og nanotråde koncentrerer lyset inde i nanotrådene, og betyder at en spredt opstilling af nanotråde (mindre end 5% af arealet) kan absorbere alt det lys der rammer området. Resonanseffekterne i samspil med en glidende overgang af brydningsindekset fanger lyset i nanotrådene. Resultatet er at enkeltdiode nanotrådssolceller har en højere teoretisk maximal effektivitet end tilsvarende flade solceller, og krystaldyrkningsmulighederne forøger effitivitetsfordelen ved brug af nanotårde i MJ solceller.

For at fremstille, karakterisere og forbedre kvaliteten af nanotråds solceller er viden om hvordan solceller virker essentiel. Vekselvirkningen mellem lys og halvleder bliver beskrevet, og desuden hvordan en pn-fotodiode adskiller de genererede ladningsbærere, og nogle af de vigtigste tabsprocesser bliver diskuteret.

Nanotrådsdyrkning er en tynd, lodret specialisering af normal flad krystaldyrkning. De elementære krystaldyrkningsprocesser, nemlig adsorption, diffusion, inkorporation og nukleation bliver beskrevet med udgangspunkt i molekyle stråle epitaxy.

De strategier der bruges til at dyrke halvleder nanotråde og de mest brugte teknikker der udnytter disse strategier bliver beskrevet med fokus på katalyseret nanotrådsdyrkning. Heterostrukturer hvor materialet og/eller doteringen ændres inde i nanotrådene er nødvendige, hvis nanotrådssolceller skal blive en succes. Både axiale og radiale heterostrukturer bliver diskuteret med vægt på de muligheder og problemer de giver nanotrådsdyrkning.

Den nuværende status for nanotråds forskning og udvikling diskuteres startende med et resume af vores egne udgivelser.

Vi har demonstreret nanotrådenes indbyggede lyskoncentration ved at dyrke, kontaktere og karakterisere en solcelle bestående af en enkelt lodretstående gallium arsenid (GaAs) nanotråd dyrket på silicium med en radial p-i-n fotodiode. Den gennemsnitlige koncentration var ~8, og maxkoncentrationen var ~12.

Vi har demonstreret hvordan fosfor (P) indføres i Ga-katalyseret nanotrådsdyrkning og dyrket $GaAs_{1-x}P_x$ nanotråde med forskellige koncentrationer af $P(x)$. Inklusionen af P var generelt højere i nanotråde end i flad dyrkning ved identisk procentdel af P i dyrkningsfluxen. Endnu mere interessant var at procentdelen af P i nanotråden var en konkav funktion af procentdelen af P i fluxen, mens det for flad MBE dyrkning var en konvex funktion.

1,7eV er det ideelle båndgap for en topcelle i en dobbelt-celle solcelle, hvor silicium er bundcellen. Det kan opnås med $GaAs_{0.8}P_{0.2}$. Vi demonstrerede dyrkning af GaAsP nanotråde med denne komposition og dyrkede også en skal rundt om kernen med den samme komposition. Den krystalmatchede GaAsP kerne-skal nanotråd blev doteret så hver nanotråd indeholdt en radial p-i-n fotodiode. Nogle af nanotrådene blev fjernet fra dyrkningsunderlaget og lavet til enkelt nanotråds solceller (ENTSC). Den bedste enhed havde en effektivitet på 6,8% ved 1.5AMG 1-sols belysning. For at forbedre effektiviteten blev overfladen passiveret ved at dyrke en yderligere skal bestående af stærkt doteret, bredt båndgap indium gallium fosfid. Den bedste ENTSC fra denne dyrkning havde en effektivitet på 10,2%.

Høstede nanotrådssolceller er ikke målet for vores forskning, men blot et trin på vejen til ægte solceller. For nanotrådssolceller betyder dette milliarder af identiske nanotråde i næsten uendelige ordnede rækker. Det giver nye udfordringer når nanotrådene skal indsættes i et kredsløb og den genererede strøm effektivt opsamles. Det aktuelle tekniske niveau for nanotrådssolceller bliver diskuteret med fokus på de strategier der for nuværende bruges, samt fordele og problemer for strategierne præsenteres.

1.3. Objectives

The experimental research has been carried out for or in collaboration with a commercial solar cell company. Therefore, the objective for the research has been: Develop nanowire solar cells that can compete with commercial solar cells. The development of solar cell efficiencies are shown in Fig. 1.1. Solar cells commercial potential has traditionally come down to two calculations: Efficiency/cost on the ground (terrestrial), and efficiency/weight in space. The two segments have been serviced by their own types of solar cells. The terrestrial cells have a low cost and low to medium efficiency. The aerospace cell have about twice as high an efficiency as terrestrial cells, but at a cost that is around 100 times higher, Fig. 1.2. In between these two types of solar cells there is a market for solar cells that service products, where a minimum efficiency is required, but the high efficiency cells are too expensive. This market gap is the most likely the initial market for nanowire solar cells.

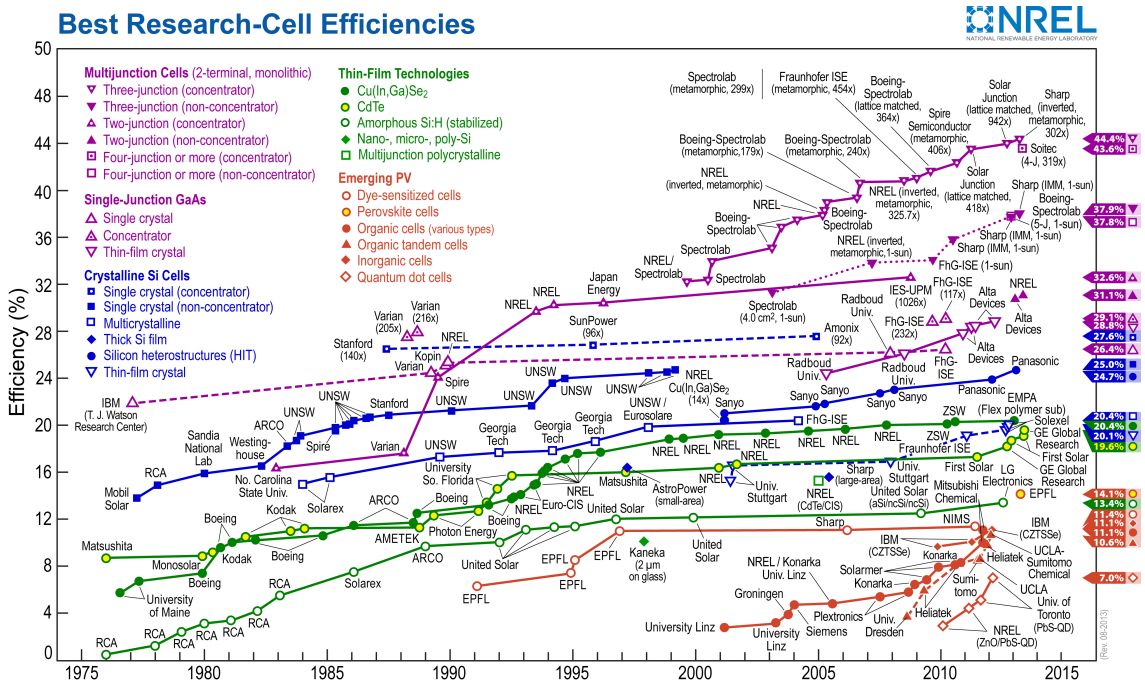

Figure 1.1.: Solar cell efficiency development since 1975. Adapted from [1]

Initially, it is unlikely that solar cells made completely or partially out of nanowires will be close enough to their potential, that they can compete on efficiency with III-V multi junction solar cells or on price with e.g. crystalline silicon solar cells.

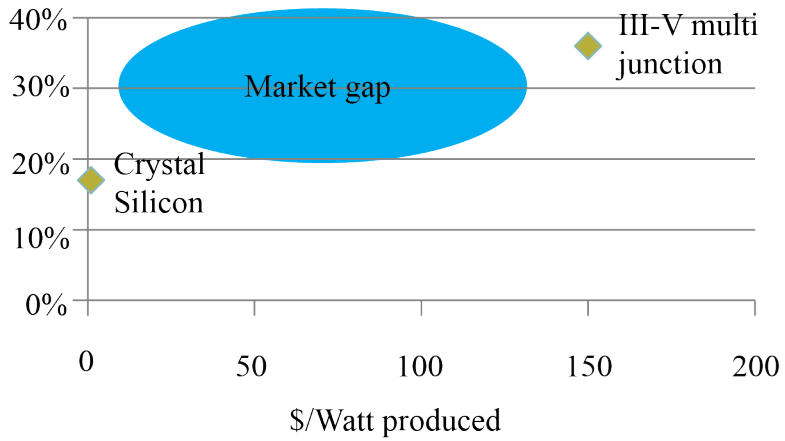

Figure 1.2.: Solar cell market. The current commercial solar cells are either very expensive and highly efficient or cheap and not very efficient. Between these approaches a market gap exist, which nanowire solar cells potentially can fill.

Nanowire solar cells, however, have the potential to combine the two technologies, since the nanowires have the ability to combine cheap silicon with high efficiency III-V solar material. This can mean growing nanowires with a bandgap suitable for single junction cell, or with a bandgap that in combination with a solar cell in silicon produces a good dual-junction solar cell. We have tried both, and the research has produced both nanowire solar cells made out of GaAs, which is ideal for a single junction solar cell, and GaAsP with a 1.7eV bandgap, which is ideal for a dual-junction in combination with silicon.

1.4. Acknowledgments

Thanks to my supervisor Jesper Nygård for guidance, and for giving me the opportunity to complete an unorthodox PhD.

Thanks to my former colleagues in SunFlake: Martin Aagesen, Henrik Ingerslev Jørgensen and Morten Schaldemose. We didn't quite succeed commercially, but we did have some interesting years exploring nanowire growth in a difficult direction. Once we wised up some excellent papers came out of the research, so the time was not total a loss.

A huge thank you to our collaborators in other labs. Huiyun Liu's group at University College London, where all the GaAsP nanowires for our publications have been grown and partially characterized. Without the collaboration with UCL the GaAsP-silicon dual-junction research would have been impossible, so I am very grateful for the collaboration and look forward to continued collaboration in the years to come. Anna Fontcuberta i Morral's group at École polytechnique fédérale de Lausanne whose expertise in simulating the absorption of nanostructures and optical characterization setup completely changed and increased the impact of the publication on single vertical GaAs nanowire solar cells.

Thanks to the nanowire growth group at NBI/Q-Dev/SunFlake: Martin Aagesen, Henrik Ingerslev Jørgensen, Peter Krogstrup, Morten Hannibal Madsen, Jesper Nygård and Claus B. Sørensen. Together we figured out how to grow nanowires on the MBE system at the HCØ institute. Some were successful and others not so much, but for a "semi-retired" MBE system built for something else we did allright.

Thanks to Erik Johnson for teaching me how to use the transmission electron microscope, and bringing me to an eye-opening conference with the European research collaboration MACAN. If we had known more about wetting and interfaces, when we started in SunFlake, we would have had a much better shot at succeeding.

Thanks to Susan Stipp and Kim Dalby from the NanoGeoScience group at the Nano-Science Center for attempting to slize through nanoparticles with me. I still hope we can publish the results in time.

Thanks to the people who read and critiqued part of my thesis: Martin Aagesen, Peter Krogstrup, Kasper Grove-Rasmussen, Giulio Ungaretti, and Shivendra Upadhyay.

Thanks to all the people at Center for Quantum Devices for a fun year. I'll be back soon to suck more knowledge out of your brains.

A special thanks to the people that have made sure everything ran smoothly during my time at NBI/Q-Dev: Peter Bidstrup, Inger Jensen, Gitte Michelsen, Jess Martin, Nader Payami and Claus B. Sørensen.

Thanks to my family and friends for support during the work. I'm as surprised, as you are, that this happened. Life is weird.

The research was in part funded by: Danish National Advanced Technology Foundation, EU through FP7-SME programme support to project PolyGlass, A University of Copenhagen Center of Excellence and UNIK Synthetic Biology project

My PhD grant was sponsered by the Danish Strategic Research Council AnaCell project, and the Niels Bohr Institute.

1.5. List of papers and contributions

The papers which have been published in relation to the PhD. They are in listed in order of publication. In the text they are referred to as I,II and III.

I. **Surface-passivated GaAsP single-nanowire solar cells exceeding 10% efficiency grown on silicon**
Jeppe V. Holm*, Henrik I. Jørgensen*, Peter Krogstrup, Jesper Nygård, Huiyun Liu & Martin Aagesen*
Nature Communications, **4**, Article number: 1498 (2013)
I participated in the growth development, characterization and device design. I did most of the device fabrication and solar measurements. I was the primary writer.

II. **Single-nanowire solar cells beyond the Shockley–Queisser limit**
Peter Krogstrup*, Henrik Ingerslev Jørgensen*, Martin Heiss*, Olivier Demichel, **Jeppe V. Holm**, Martin Aagesen, Jesper Nygard & Anna Fontcuberta i Morral
Nature Photonics, **7**, 306-310 (2013)
I helped develop the contacting scheme. I was part of discussions before, during and after device fabrication and solar characterization. I discussed and commented all results and the manuscript.

III. **Self-Catalyzed GaAsP Nanowires Grown on Silicon Substrates by Solid-Source Molecular Beam Epitaxy**
Yunyan Zhang*, Martin Aagesen*, **Jeppe V. Holm**, Henrik I. Jørgensen, Jiang Wu, & Huiyun Liu
Nano Letters, **13**, 3897–3902 (2013)
I participated in the growth development. I performed most of the SEM, TEM and EDX characterization. I discussed and commented all results and the manuscript.

*Equal contributors

1.6. Tables of symbols and abbreviations

Abbreviations

Abbreviation	Full name
2D/3D	Two/Three Dimensional
AM 1.5G	Air Mass 1.5 Global
ARC	Anti-Reflection Coating
As	Arsenic
BEP	Beam Equivalent Pressure
CdTe	Cadmium Telluride
EDX	Energy-Dispersive X-ray Spectroscopy
ENTSC	Enkelt Nanotråds Solceller
FDTD	Finite-Difference Time-Domain
Ga	Gallium
GaAs	Gallium Arsenide
GaAsP	Gallium Arsenide Phosphide
Ge	Germanium
Au	Gold
In	Indium
InSb	Indium Antimony
InAs	Indium Arsenide
InGaP	Indium Gallium Phosphide
InP	Indium Phosphide
ITO	Indium Tin Oxide
MOCVD	Metalorganic Chemical Vapor Deposition
MBE	Molecular Beam Epitaxy
MJ	Multi Junction

Abbreviation	Full name
NW	Nanowire
NWSCA	Nanowire Solar Cell Array
PL	Photo-Luminescence
P	Phosphorous / Fosfor
QE	Quantum Efficiency
RHEED	Reflection High-Energy Electron Diffraction
SEM	Scanning Electron Microscopy
SAE	Selective Area Epitaxy
SAG	Selective Area Growth
SQ	Shockley-Queisser
SRH	Shockley-Read-Hall
Si	Silicon
SNWSC	Single Nanowire Solar Cell
XRD	Small Angle X-ray Diffraction
SCR	Space Charge Region
TEM	Transmission Electron Microscopy
TCO	Transparent Conducting Oxide
TL	Triple-Phase Line
VLS	Vapor Liquid Solid
VS	Vapor Solid
WZ	Wurtzite
ZB	Zinc Blende

Solar cell symbols

Symbol	Name
N_A	Acceptor Concentration
θ_i	Angle of Incidence
$\Omega_{sun}, \Omega_{emit}$	Angle of Sundisc, Emission
$\bar{t}$	Average Time Between Collision
E_g	Bandgap Energy
k_B	Boltzmann Constant
$\frac{\partial n}{\partial y}, \frac{\partial p}{\partial y}$	Concentration Gradient for Electrons, Holes
J_{rec}, J_{gen}	Current Density for Recombination and Thermal Generation
J_m	Current Density at Maximum Powerpoint
J_{dark}	Dark Current Density
J_0	Dark Saturation Current density
$J_{D,n}, J_{D,p}$	Diffusion Current Density for Electron, Holes
D, D_n, D_p	Diffusivity, For electrons, For holes
N_D	Donor Concentration
$\mathbf{v}_{avg,n}, \mathbf{v}_{avg,p}$	Drift Velocity for Electrons, Holes
Δn	Excess electron concentrations
Δp	Excess hole concentrations
η	Efficiency
$\mathbf{E}$	Electric Field
μ	Electron Mobility
q	Elementary Charge
FF	Fill factor
n_0	Free Electron Concentration
p_0	Free Hole Concentration
ν	Frequency
n	Ideality Factor
$n_1, n_2, n_{solar}, n_{air}, n_{ARC}$	Index of Refractions
n_i	Intrinsic Carrier Concentration
I_λ	Irradiance
$\tau, \tau_{Rad}, \tau_{SRH}, \tau_{Aug}, \tau_n, \tau_p$	Lifetime or Recombination Time for Electrons, Holes
I	Light Concentration Factor
J_L	Light Generated Current Density

Symbol	Name
P_m	Maximum Power
l	Mean Free Path Between Collisions
L_n, L_p	Minority Carrier Diffusion Length for Electrons, Holes
μ_n, μ_p	Mobility for Electrons, Holes
v_{oc}	Normalized Open Circuit Voltage
V_{oc}	Open circuit voltage
E_{ph}	Photon Energy
h	Planck's Constant
P_{in}	Power density into cell
P_{out}	Power Density Produced by Solar Cell
T_p	Pyrometer Temperature
R_s	Series Resistance
J_{sc}	Short Circuit Current Density
R_{sh}	Shunt Resistance
c	Speed of Light
T	Temperature
T_c	Thermo Couple Temperature
V	Voltage
V_m	Voltage at Maximum Powerpoint
λ	Wavelength

Crystal growth symbols

Symbol	Name
E_a	Activation Energy
$\frac{\partial n}{\partial x}$	Adatom Density Gradient
J_a	Adatom Diffusion Current
D_a	Adatom Diffusivity
ω^*	Attachment Rate of Atoms
s_c	Atom Area
k_B	Boltzmann Constant
μ_p	Chemical Potential of State p
l^*	Critical Length
n^*	Critical Nucleus Size
E_{des}	Desorption Energy
Γ_{des}	Desorption Rate
τ_{des}	Desorption Time
E_{dif}	Diffusion Energy
Γ_{dif}	Diffusion Rate
$\Delta\mu_{\alpha\beta}$	Difference in Chemical Potential or Supersaturation Between α and β
S	Entropy
ΔG	Gibbs Work of Formation
ΔG^*	Gibbs Critical Work of Formation
G	Gibbs Free Energy
τ_{inc}	Incorporation Time
U	Internal energy
v	Length of Vector
a	Mean Distance Between Adsorption Sites
h	Nucleus Height
l	Nucleus Sidewall Length
N	Number of Particles in Phase
A	Number of Reaction Attempts Per Second
P	Pressure
ϕ	Proportionality Factor
Γ_{Ar}	Rate Constant of a Chemical Reaction

Symbol	Name
χ	Sidewall Energy
γ	Specific Surface Free Energy Per Area
c_1	Steady State Concentration of Single Unit Large Clusters
J_s	Steady State Nucleation Rate
ρ	Steric Factor
ξ_{solid}	Surface Area
τ_{surf}	Surface Time
T	Temperature
n	Number of Atoms
$\nu_{\perp}, \nu_{=}$	Vibrational Frequency Normal, Parallel to Surface
V	Volume
$\Delta\gamma$.	Wetting
Z	Zeldovich Factor

2. Planar Solar Cells

2.1. Introduction

The solar cell shown in Fig. 2.1 basically works as follows: Part of the suns emitted photons hit the solar cell. If a photon has sufficient energy an electron is freed from its place as a valence electron in a crystal bond. The pn-junction separates the electron from the hole it left behind, and the moving carriers power the load in the circuit.

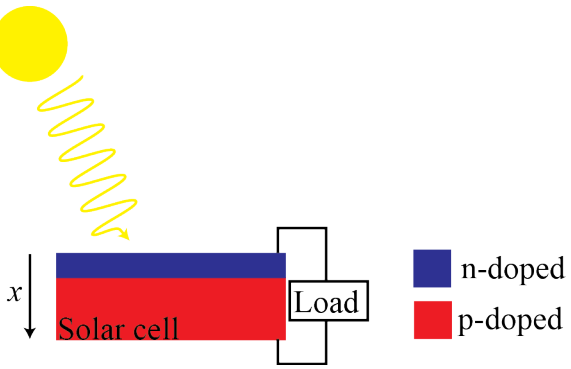

Figure 2.1.: The most basic solar cell consists of a p- and n-doped region, which separates the free carriers created by the sunlight hitting the solar cell. The distance from the front surface is x.

2.2. Solar irradiance

The Sun, almost, emits radiation like a black-body with a temperature of 5777K [2], which means the Sun's irradiance at its surface can be described with Planck's radiation law [3]: $I_\lambda = \frac{2\pi hc^2}{\lambda^5}\left(\frac{1}{e^{\frac{hc}{\lambda k_B T}}-1}\right)$ where k_B is the Boltzmann constant, h is Planck's constant, c is the speed of light, λ is the wavelength, and T is the temperature. The

power is delivered in photons that have the energy: $E_{ph} = h\nu = \frac{hc}{\lambda}$ where ν is the frequency. For solar energy, the first interesting photon flux is the one above the Earth's atmosphere, which is the black line in Fig. 2.2. This is the spectra solar panels on satellites in orbit around Earth on satellites utilize. For solar panels on the Earth's surface the atmosphere's absorption has to be taken into account.

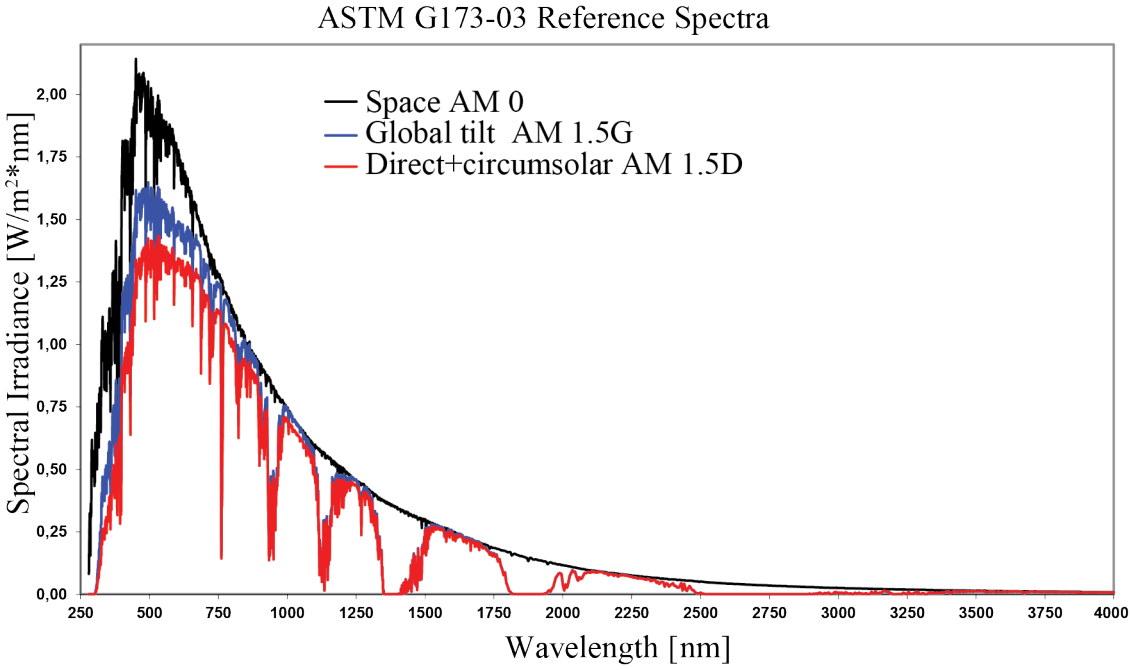

Figure 2.2.: Solar spectrum at various places. The black line is outside Earth's atmosphere and is the reference spectrum AM0. The red line is the direct sunlight light hitting a sun-tilted surface at 37^o on the Earth's surface AM 1.5D. The blue line is light hitting a sun-tilted surface at 37^o including diffuse light and is the reference spectrum AM 1.5G. The AM 1.5G spectrum is the most used reference spectrum. Spectra are adapted from [4].

2.2.1. Atmosphere

The atmosphere's various constituents absorb sunlight at some wavelengths, which means that the spectra reaching the ground has some large dips when compared to the non-filtered spectrum in space, as seen in the red and blue lines in Fig. 2.2. Additionally, the photons experience different atmosphere thicknesses dependent on where in the world the solar cell is situated. Barometric pressure, clouds, pollution, moisture and dust also affects the number of photons hitting a given solar cell.

2.2.2. Air mass 1.5G reference spectrum

If solar cells were tested in natural sunlight, it would be practically impossible to compare them with each other, since the position on Earth, time of year, time of day, weather and atmospheric conditions would impact the tested efficiency. Therefore standard spectra have been decided on. The spectra can be reproduced by lamps with special filters, which makes it possible to compare the performance of different solar cells with each other. In particular, the air mass 1.5 ground (AM 1.5G) standard spectrum is used for simulations on solar cell meant for use on Earth, since it includes both direct and diffuse sunlight, blue line in Fig. 2.2. One of the important aspects of the AM 1.5G reference is that it is normalized to 1000W/m^2. Tests with the AM 1.5G spectrum generally gives a good estimation of the real world performance of single junction solar cells.

Multijunction (MJ) solar cells are more susceptible to variations in spectral differences, since current matching is very important, and light hitting the solar cell directly, since anti-reflection is important (see Sec. 2.6.1). Therefore, MJ solar cells are exclusively used in space and in high sunlight concentration conditions where trackers and orientation systems keep the solar cell constantly facing the Sun. Still, using the real spectrum in the intended deployment position can change the design and yield a few extra % efficiency compared to the standard spectrum.

2.3. Semiconductors

A semiconductor is a material that under certain conditions conduct current and under different conditions is insulating. The specific electronic properties are determined by their material characteristics, and different materials are suited for different uses. The most important semiconductors for solar cells are silicon (Si), germanium (Ge), which are group IV materials, compound III-V materials such as gallium arsenide (GaAs), and II-VI compound materials such as cadmium telluride (CdTe). For solar purposes the most important differences between the semiconductors are the size of the bandgap and whether the bandgap is direct or indirect. These properties can be seen in Fig. 2.3, which gives an overview of the bandgaps available to a solar cell designer working in the group III-IV-V material system.

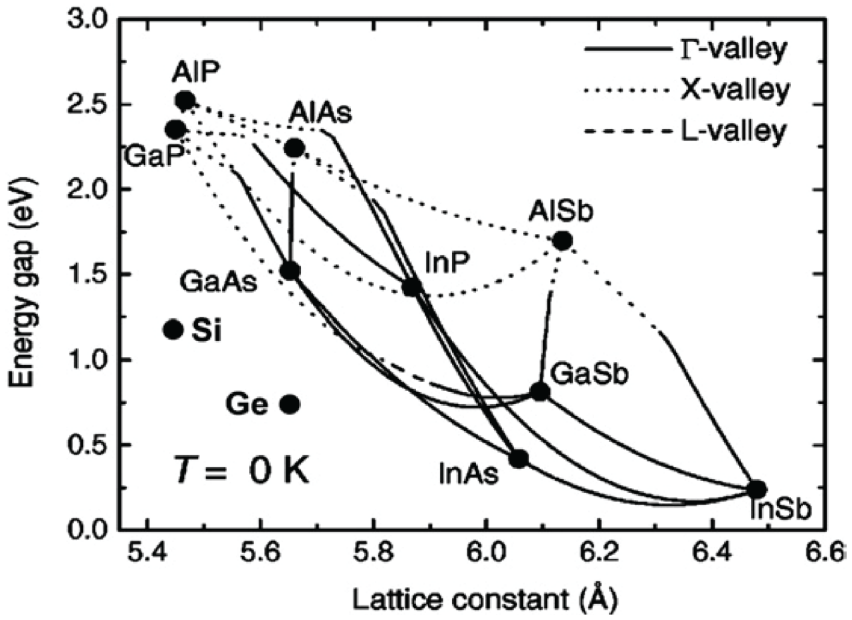

Figure 2.3.: An overview of lattice constants and bandgaps for selected III-V crystals including Si and Ge. The dots indicate the pure materials and the connecting lines are ternary compounds. The solid lines are direct bandgaps, and the dotted are indirect. Si and Ge both have indirect bandgaps. Adapted from Cotal[5].

2.3.1. Bandgap

A material property of any semiconductor is that it contains an electronic bandgap as seen in Fig. 2.4. A bandgap is an energy range in solids where no electron states can exist. The size of the bandgap is the energy distance between the valence band, which is filled with electrons, and the conduction band, which is empty but where electrons can be temporarily excited into. Another way of thinking about the bandgap is that it is the energy required to remove an electron from the outer shell of an atom and become a mobile carrier. The size of the bandgap is given in electron volts and is for e.g. GaAs 1.43eV @ 300K. In intrinsic, or un-doped, semiconductors the Fermi level is in the middle of the bandgap. The Fermi level is defined as the energy level that has a 50% probability of being filled in thermodynamic equilibrium. Indirect bandgap semiconductors require phonon interaction to excite an electron from valence band to conduction band or to recombine the other way.

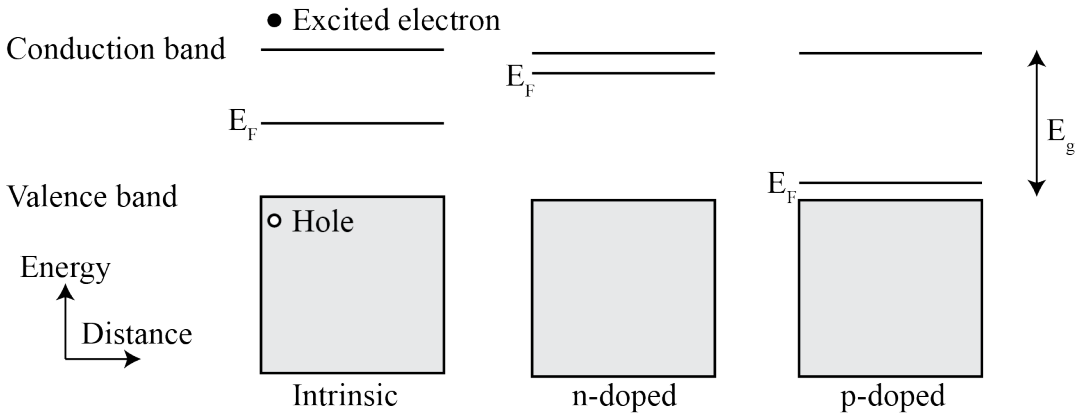

Figure 2.4.: Semiconductor bandgap. The valence band is filled with electrons. The conduction band is empty. The bandgap energy E_g is the minimum energy required to excite an electron from the valence to the conduction band. Excited electrons will leave behind a hole in the valence band. The Fermi level is in the middle of the bandgap for intrinsic semiconductors, in n-doped(p-doped) semiconductors the Fermi level is moved towards the conduction(valence) band.

2.3.2. Intrinsic carriers

Thermal excitation of electrons from the valence band into the conduction band creates a free carrier electron(hole) in the conduction(valence) band. The concentration of these electrons, which is equal to the concentration of holes, is called the intrinsic carrier concentration and is denoted n_i. Since the intrinsic carriers are thermally excited across the bandgap the concentration will be higher for low bandgap materials or when the temperature of the semiconductor is raised.

2.3.3. Doping

The number of intrinsic carriers is generally too low to make effective devices. In order to increase the number of free carriers, as well as design an electronic potential structure within the devices, atoms that are not normally part of the crystal are added during material processing. The semiconductor is then said to be doped and the added atoms are called dopants. If you wish to have more free electrons(holes) in a section of the semiconductor, atoms with more(less) electrons in the outer shells than the atom they replace are added. Atoms with more electrons are called donors and atoms with less electrons are called acceptors. An area with more donors(acceptors) is called n(p)-doped. The Fermi level in a n(p)-doped semicon-

ductor area is shifted towards the conduction(valence) band. The donor(acceptor) concentration is called N_D (N_A). After doping, the doped region will have a higher concentration of one carrier type. This carrier is called the majority carrier, while the carrier with the lowest density is called the minority carrier. It is important to note that the majority carrier in one section can be the minority carrier in a different section. Doping incorporation in planar growth is a mature theoretically and experimentally understood process. This means that the semiconductors doping profile can be exactly controlled, which is extremely important to solar cells.

2.3.4. Equilibrium carrier concentrations

With no applied bias the number of carriers are at the equilibrium concentration. The product of the majority and minority carriers are:

$$n_0 p_0 = n_i^2 \tag{2.1}$$

where n_0 is the free electron concentration and p_0 is the free hole concentration. When semiconductors are doped, the doping concentration is usually several orders of magnitude higher than the intrinsic carrier concentration. From this follows that:

$$\text{n-type:} \quad n_0 = N_D,\ p_0 = \frac{n_i^2}{N_D} \tag{2.2}$$

$$\text{p-type:} \quad p_0 = N_A,\ n_0 = \frac{n_i^2}{N_A} \tag{2.3}$$

where N_D is the donor concentration and N_A is the acceptor concentration. The two equations show that the minority carrier concentration decreases when the semiconductor is highly doped, since e.g. some of the added electrons will occupy unfilled holes and thereby lower the hole concentration.

2.3.5. Light absorption

The sunlight consists of a large number of photons that each have a different energy and wavelength as described in Sec. 2.2. Depending on the relation between the

photon energy and the semiconductors bandgap three things can happen as shown in Fig. 2.5. Photons with an energy lower than the bandgap ($E_{ph} < E_g$) will interact very weakly with the semiconductor and pass through it. Photons with an energy exactly like the bandgap ($E_{ph} = E_g$) have just enough energy to excite an electron into the conduction band and thereby create an electron-hole pair, so this is a very efficient energy conversion. Photons with an energy larger than the bandgap ($E_{ph} > E_g$) will interact strongly with the semiconductor and will create an electron-hole pair. The excess energy imparted to the electron-hole pair will, however, be lost as the electron(hole) quickly thermalizes to the edge of the conduction(valence) band, therefore this is a less efficient energy conversion.

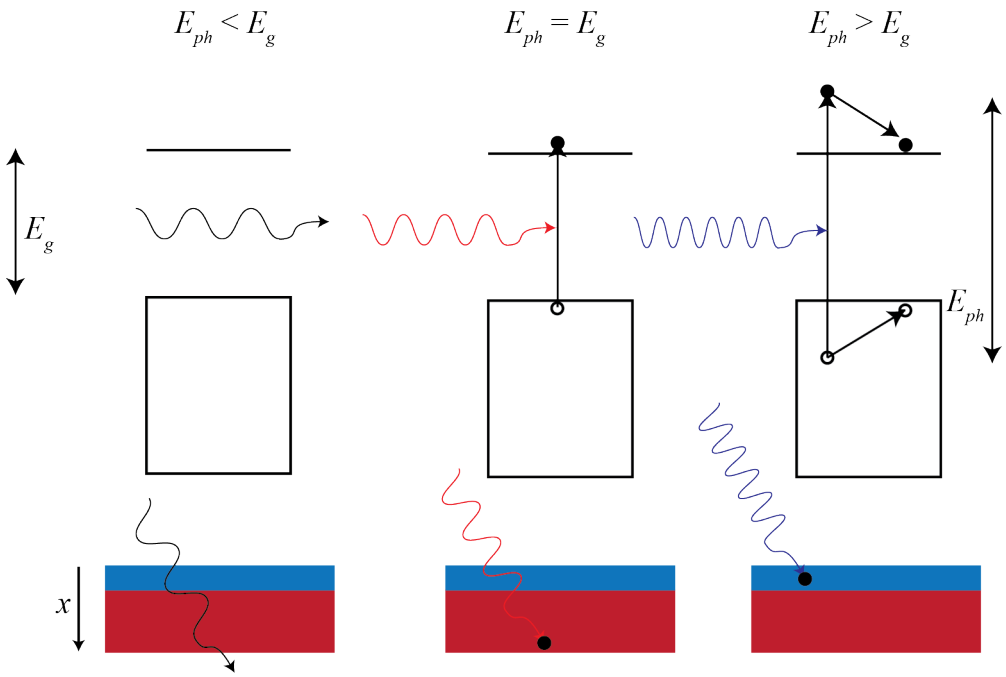

Figure 2.5.: Absorption of light. Top: If $E_{ph} < E_g$ the photon passes through the semiconductor without being absorbed. If $E_{ph} = E_g$ the photon has just enough energy to excite an electron across the bandgap from the valence to the conduction band. If $E_{ph} > E_g$ the photon excites an electron across the bandgap. The additional energy departed to the electron and hole is quickly lost through thermalization as the electron(hole) relaxes to the band edges. Bottom: The low energy photons pass through the solar cell. Photons with energy close to the bandgap interact weakly with the material and are generally absorbed in the bulk of the solar cell. High energy photons interact strongly with the material and are therefore absorbed closer to the solar cells surface.

The absorption of photons raises the carrier concentration above the equilibrium:

$n = n_0 + \Delta n$ and $p = p_0 + \Delta p$ where Δn and Δp are the excess carrier concentrations above the equilibrium.

Due to the heavy doping of most solar cells, the number of majority carriers which are generated by light absorption (excess carriers) is lower than the majority carriers in the semiconductor due to doping. The number of majority carriers are therefore roughly equal to the doping concentration. The opposite is true for minority carriers, as the absorption generated minority carriers (excess carriers) outnumber the equilibrium minority carrier concentration. The minority carrier concentration then becomes equal to the excess carrier concentration:

$$\text{n-type:} \quad n = N_D,\ p \approx \Delta p \tag{2.4}$$

$$\text{p-type:} \quad p = N_A,\ n \approx \Delta n \tag{2.5}$$

2.3.5.1. Absorption depth

Not all photons are absorbed in the first atomic row in the semiconductor. A semiconductors absorption is defined by the absorption coefficient $\alpha = \frac{4\pi k}{\lambda}$, where k is the extinction coefficient and λ is the photons wavelength. High energy photons have a greater likelihood of being absorbed in the top of the semiconductor than low energy photons, which generally travels further in the semiconductor before being absorbed. The absorption depth, which is the inverse of the absorption coefficient α^{-1}, in semiconductors is the length a number of identical photons have to travel before only 37% of the original light intensity is left or their number has dropped by $1/e$. As the photons are absorbed they create electron-hole pairs, and the generation rate can be written as: $G = \alpha N_0 \mathrm{e}^{-\alpha x}$ where N_0 is the photon flux at the surface, and x is the distance from the surface. Different semiconductors have different absorption coefficients, where the greatest factor to take into consideration is whether the semiconductor has a direct or in-direct bandgap, since in-direct bandgap semiconductors also requires phonon interaction for absorption and recombination. In-direct bandgap semiconductors consequently have much longer absorption depths, but also much longer lifetimes for excited carriers.

2.3.6. Carrier movement

Unbound electrons, which are not submitted to an electric field, are free to move in the semiconductor. The free carriers move in a random fashion by going straight until scattering of a lattice atom, as depicted in Fig. 2.6.a. The free carrier movement in a particular semiconductor is characterized by the diffusivity:

$$D = \frac{l^2}{2\bar{t}} \tag{2.6}$$

where l is the mean free path between collisions, which is material dependent, and $\bar{t}$ is the average time between collisions, which is lower at high temperatures. The diffusivity is different for electrons and holes. Barring any interference there will be zero net movement of carriers. There are, however, two ways that carriers can obtain a net movement: Diffusion and drift.

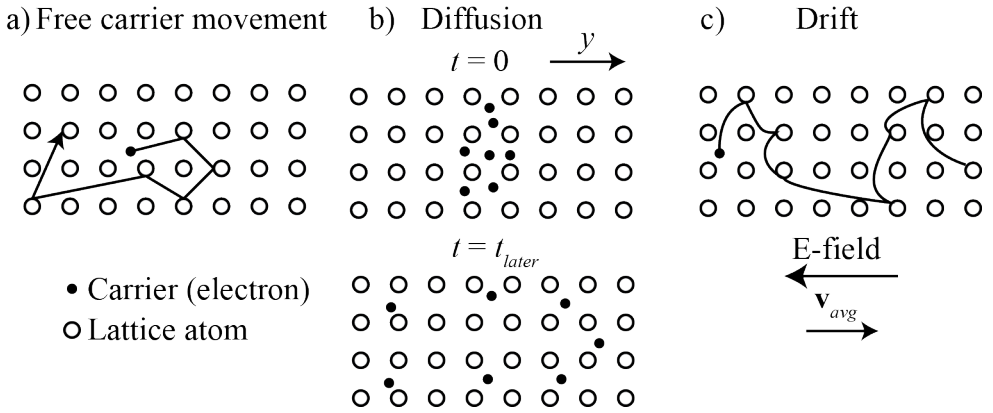

Figure 2.6.: Carrier movement. **a.** Free carrier movement. **b.** Diffusion. A high concentration at $t = 0$ will be dispersed at some later time $t = t_{later}$ through random free carrier movement. **c.** Drift. After each scattering event the movement will be governed by the momentum and the force on the particle by the electric field.

2.3.6.1. Diffusion

If a section of the semiconductor, for some reason e.g. absorption of light, has a higher concentration of carriers than elsewhere, there is a carrier concentration gradient, as in Fig. 2.6.b. The normal random carrier movement will then cause a

net movement against the concentration gradient as defined by Fick's law[6]:

$$J_{D,n} = -D_n \frac{\partial n}{\partial y} \tag{2.7}$$

$$J_{D,p} = -D_p \frac{\partial p}{\partial y} \tag{2.8}$$

where D_n (D_p) is the diffusivity of electrons(holes) and $\frac{\partial n}{\partial y}$ $\left(\frac{\partial p}{\partial y}\right)$ is the electron/hole concentration gradient. Diffusion will automatically cause the carriers to be spread out evenly, if enough time is allowed and no new source of or sinks for carriers are introduced to the semiconductor. It's important to note that diffusion occurs under no electric field and that the diffusivity of electrons and holes can be different.

2.3.6.2. Drift

If an electric field, for some reason e.g. a pn-junction, is present in the semiconductor the field will exert a force on the carriers. The movement of the carriers then becomes the sum of the free carrier movement and the movement dictated by the electric field, as shown in Fig. 2.6.c. On average the carriers will achieve a net movement either with the electric field (holes) or against the electric field (electrons). The average velocity of the electrons(holes) is the drift velocity[7,8]:

$$\mathbf{v}_{avg,n} = -\mu_n \mathbf{E} \tag{2.9}$$

$$\mathbf{v}_{avg,p} = \mu_p \mathbf{E} \tag{2.10}$$

where μ_n (μ_p) is the electron(hole) mobility and $\mathbf{E}$ is the the electric field.

2.3.7. Recombination

If the minority carrier concentration is higher than the equilibrium concentration, recombination processes will return the concentration to equilibrium. There are three main types of recombination: Radiative recombination, Shockley-Read-Hall

(SRH) recombination[9], and Auger recombination[10], as shown in Fig. 2.7. Radiative recombination is impossible to avoid. SRH and Auger recombination should, however, be limited as much as possible.

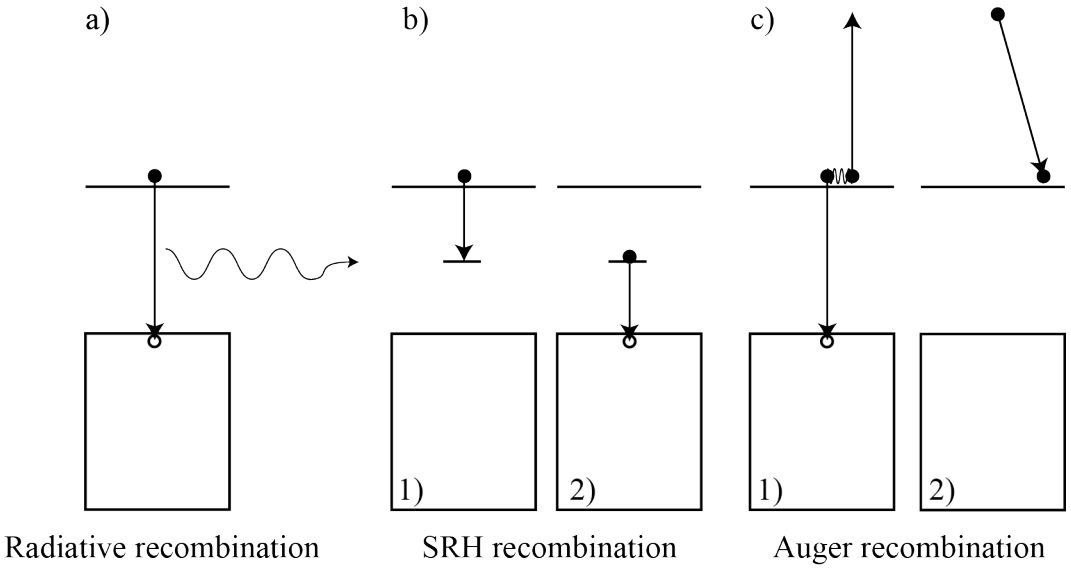

Figure 2.7.: Recombination processes. **a.** Radiative or band-to-band recombination. An electron from the conduction band recombines with a hole in valence band and a photon with the energy of the quasi Fermi level splitting is emitted. **b.** SRH or defect recombination. An electron is caught by a defect in the bandgap. While the electron is trapped in the defect a hole becomes available in the valence band and the electron fills the hole. **c.** Auger recombination. An electron recombines with a hole and the excess energy is transferred to another electron in the conduction band. The high energy electron thermalizes to the band edge afterward.

Radiative recombination, or band-to-band recombination, is when an electron from the conduction band combines with a hole from the valence band and a photon is emitted. The photon carries off the excess energy, and it will therefore have an energy similarly to the bandgap. Because of the photons energy they are generally not reabsorbed in the solar cell and are therefore lost.

SRH recombination is recombination at crystal defects. When a crystal defect creates a trap energy state within the bandgap this state can be occupied by an electron. If there is created a hole in the valence band before the electron leaves the trap state, then the electron fills the hole. Since SRH recombination is dependent on crystal defects, it is a loss mechanism that can be limited by using a pure crystal. SRH is most likely to occur via energy states in the middle of the bandgap, since it requires

involvement of both carrier types, and the rate of state filling is dependent on the energy distance from the band edges.

Auger recombination is when the energy from an electron-hole recombination is transferred to another electron in the conduction band. The receiving electron quickly looses the additional energy through thermalization back to the conduction band edge. Because three carriers are involved, Auger recombination is most important under high carrier concentration, such as heavy doping or under high solar concentration.

For individual minority carriers the three recombination processes define the minority carrier life time:

$$\frac{1}{\tau} = \frac{1}{\tau_{Rad}} + \frac{1}{\tau_{SRH}} + \frac{1}{\tau_{Aug}} \tag{2.11}$$

where τ_{Rad}, τ_{SRH}, and τ_{Aug} are the average recombination times for radiative, SRH, and Auger recombination. An important aspect of the recombination, is that it defines the length a minority carrier can diffuse in a semiconductor:

$$\begin{aligned} L_n &= \sqrt{D_n \tau_n} \\ L_p &= \sqrt{D_p \tau_p} \end{aligned} \tag{2.12}$$

where $\tau_n(\tau_p)$ is the electron(hole) minority carrier lifetime. In-direct bandgaps will have long minority carrier lifetimes, since phonons are involved in the recombination processes. The total recombination rate is dependent on the excess carrier concentration, which is the concentration of carriers in excess of the equilibrium concentration.

2.3.7.1. Surface recombinations

Surface recombination is a special case of SRH defect recombination. At the surface of the semiconductor the crystal lattice is abruptly ended, which leaves a high number of dangling bonds and possibly also contamination from the environment. The dangling bonds and contaminants becomes recombination sites for carriers. Surface recombination can be very detrimental to solar cell performance. This is especially true for small solar cells that have a large surface to volume ratio, since there is

a short distance from where the carriers are generated to the recombination sites at the surface. Nanowire solar cells suffer from this problem, and great care must therefore be taken to reduce the surface recombination to obtain a high quality solar cell.

2.4. pn-junction

When a semiconductor is hit by sunlight the photons will generate electron-hole pairs. In order to extract the imparted energy before the carriers recombine, there have to be set up a system that can separate the generated carriers from each other, and lead them to the leads where the energy can be used. The most used separation system is a pn-junction.

A pn-junction is a semiconductor junction where a p-doped region is in contact with a n-doped region as seen in Fig. 2.8. In pn-junctions the p- and n-side can be made from different semiconductors, which is called heterojunctions, or the p- and n-side can be differently doped regions of the same material, which is called homojunctions.

The junction consist of three parts, a n-doped part unaffected by the junction, a p-doped part unaffected by the junction, and the central region called the space charge region (SCR), see Fig. 2.8a. Since the two sides in the junction has a large surplus of either electrons or holes, there is a density gradient across the junction. The density gradient causes electrons(holes) to diffuse from the n-doped(p-doped) side across the junction. The movement of electrons(holes) leaves behind the charged atom, or ions, see Fig. 2.8.b. The charge difference creates an electric field in the SCR from the n-side to the p-side Fig. 2.8.c. The electric field exerts a force on the carriers, which in equilibrium is balanced with the diffusion "force", so that there is no net movement of carriers across the junction. The Fermi level has, due to the doping, been moved towards the conduction(valence) band in the n-doped(p-doped) side. When the p-side and n-side are joined the bands bends across the junction, since the Fermi level has to be constant across the junction in equilibrium Fig. 2.8.d.

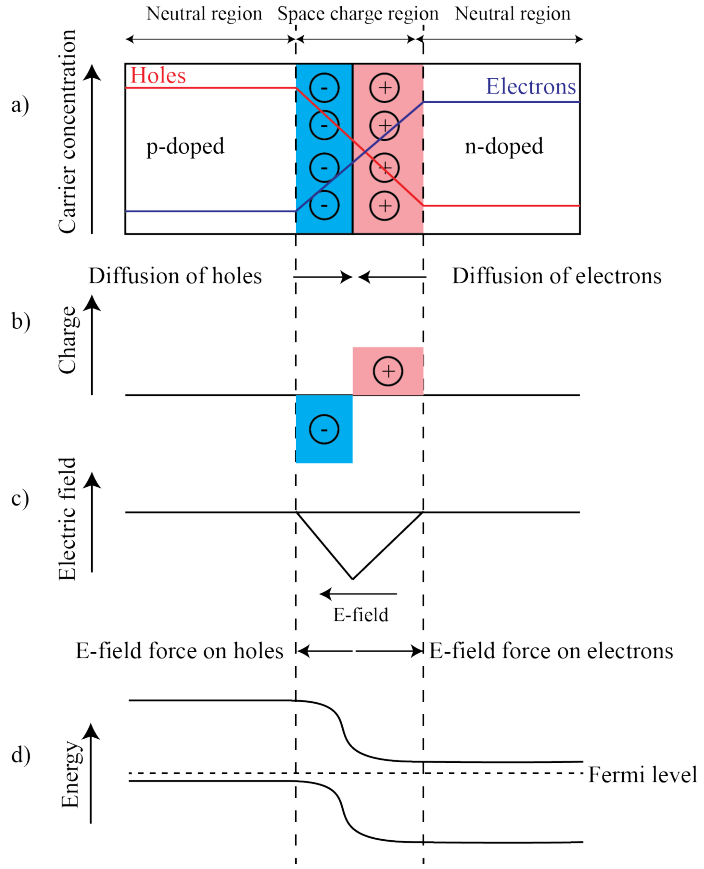

Figure 2.8.: pn-junction at equilibrium. **a.** The n-doped(p-doped) region has a surplus of electrons(holes) but are neutrally charged. **b.** Electrons(holes) diffuse against their concentration gradient and leave behind two charged regions. **c.** The charged ions creates an electric field which exerts a force on the electrons(holes), that in equilibrium is balanced with the diffusion "force". **d.** The bands are bend in the SCR in order to have a constant Fermi level across the junction.

2.4.1. Dark behavior

A pn-junction behaves as a diode, and the current density can be written as[11]:

$$J_{dark} = J_{rec} - J_{gen} = J_0 \left(\exp\left(\frac{qV}{nk_BT} \right) - 1 \right) \tag{2.13}$$

where $J_{rec} = J_0 \exp\left(\frac{qV}{nk_BT}\right)$ is the recombination current density, $J_{gen} = J_0$ is the thermal generation current density and is independent of V, J_0 is the dark saturation current density or leakage current density, q is the elementary charge, V is the voltage, k_B is Boltzmann constant, T is the temperature, and n is the ideality factor, which tells us how close the junction's behavior is to an ideal diode ($n = 1$).

For solar cells, J_{dark} is the current density that will flow under no illumination, which is why it is referred to as the dark current. J_o is a signature of the individual diode, and will be constant under constant temperature. J_{rec} is called the recombination current, since it is caused by minority carrier at the edge of the SCR that diffuse into the neutral sections and recombine with the majority carriers. J_{gen} is called the thermal generation current, since it is caused by minority carriers generated in the doped sections that drift across the junction. A curve that shows the current density-voltage relation under dark conditions can be seen in Fig. 2.10.a.

2.5. Solar cell behavior

When the pn-junction is illuminated electron-hole pairs are created by the photons as shown in Fig. 2.9. If the carriers are created inside the SCR, or within a diffusion length so they are able to diffuse into it, they are separated by the built-in electric field across the SCR. If electron-hole pairs are created away from the SCR the minority carriers will recombine before they can be caught. If the carriers reach all the way to the external load, they deliver the energy qV, where V is the voltage applied to the solar cell.

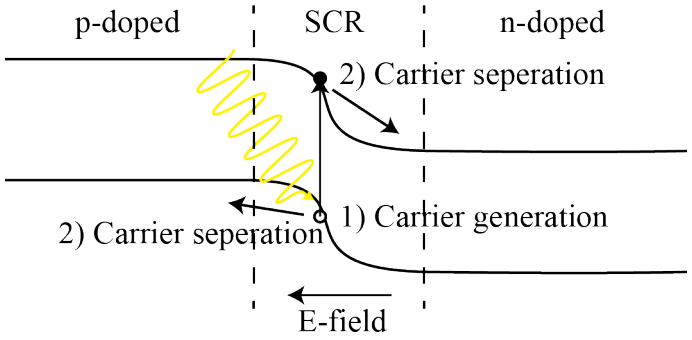

Figure 2.9.: Solar cell behavior. 1) Electron-hole pairs are generated by photons hitting the solar cell. 2) Carriers generated in the SCR or within a diffusion of the SCR edge are separated by the built-in electric field.

The relation between the power that hits the solar cell and the power that the solar cell produces is called the efficiency:

$$\eta = \frac{P_{out}}{P_{in}} \tag{2.14}$$

where P_{in} is the power density hitting the solar cell and P_{out} is the power density produced by the solar cell. Power density is preferred over absolute power, since it makes it easier to compare solar cells with different surface areas. P_{in} for installed solar cells is the photons reaching them from the sun, whereas laboratory solar cells are struck by photons from man-made light sources, as described in Sec. 2.2. The P_{out} we are most interested in, is the maximum power, P_m, available under operation. P_m can be written in a number of ways:

$$P_m = J_m V_m = J_{sc} V_{oc} FF \tag{2.15}$$

where J_m and V_m are the current density and voltage at the maximum powerpoint, J_{sc} is the short circuit current, which is the current drawn when the solar cell terminals are connected, V_{oc} is the open circuit voltage, which is the voltage when the terminals are not connected or under infinite load, and FF is the fill factor, which is a quality factor that shows how efficiently the generated power can be extracted and corrects between $J_m V_m$ and $J_{sc} V_{oc}$. A better understanding of the parts of P_m can be gleamed if we look at an idealized J-V curve for a solar cell, Fig. 2.10.a.

2.5.1. Ideal solar cell equations

For ideal pn-junctions under illumination, the current density is given by:

$$J = J_0 \left(\exp\left(\frac{qV}{nkT} \right) - 1 \right) - J_L \tag{2.16}$$

where $J_L \approx J_{sc}$ is the current density generated under illumination. From Eqn. 2.16 it can be seen that the current generated by light has the opposite sign of the dark current, and that the current generated by light is generally independent of the voltage. The open circuit voltage is found at the voltage where the dark and light currents are equal. By setting Eqn. 2.16 equal to zero and isolating V we find the ideal open circuit voltage:

$$V_{oc} = \frac{nk_B T}{q} \ln\left(\frac{J_L}{J_0} + 1 \right) \tag{2.17}$$

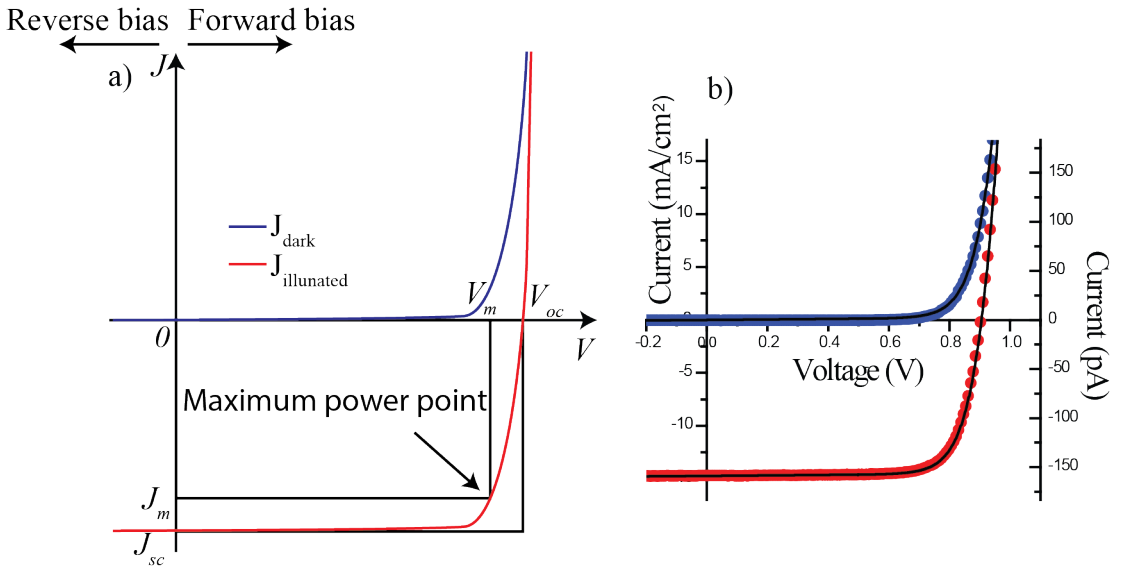

Figure 2.10.: a. Idealized solar cell JV-curves under dark and illuminated conditions. The illuminated curve is basically the dark curve shifted down by the $J_L \approx J_{sc}$. The maximum power P_m that can be extracted is the area of the largest box that can fit inside the illuminated JV-curve. The difference between $J_{sc}V_{oc}$ and J_mV_m is the fill factor FF. Negative voltage is called reverse bias, whereas positive voltage is called forward bias. **b.** Measurement of highest efficiency single nanowire solar cell (SNWSC) from [I]

The V_{oc} is mainly defined by the ideality factor and dark saturation current J_0, since the light generated current J_L is mostly unaffected by the voltage. Even though a high ideality factor would seem to give a very high V_{oc} secondary effects will counteract this. The ideal fill factor can be described by the the empirical expression[12]:

$$FF = \frac{v_{oc} - \ln(v_{oc} + 0.72)}{v_{oc} + 1} \tag{2.18}$$

where $v_{oc} = \frac{qV_{oc}}{nk_BT}$ is the normalized open circuit voltage. It is interesting to see that the ideal fill factor is increased at higher V_{oc}, which e.g. is true for higher bandgap materials and under concentrated sunlight. On the other hand, the ideal fill factor is reduced at high diode ideality factors n. The real fill factor will additionally be reduced by series resistance and shunt resistance.

2.5.2. Detailed balance or Shockley-Queisser limit

The detailed balance limit is a theoretical maximum efficiency for solar cells that was first proposed by Shockley and Queisser[13], which is why it is normally called the Shockley-Queisser (SQ) limit. The limit is calculated by using a few key assumptions:

1. P_{in} is the solar spectrum, or possibly a reference spectrum.
2. One bandgap: The solar cell material must contain exactly one energy gap that perfectly separates filled energy states from empty energy states.
3. Perfect absorption: Every photon with an energy: $E_{ph} \geq E_g$ will be absorbed and create exactly one electron-hole pair.
4. Perfect collection: All generated carriers are collected.
5. Only band-to-band radiative recombination.
6. Constant cell temperature.
7. Steady state.

The calculation will not be presented here but the results can be seen in Fig. 2.11. I will recommend Steve Byrnes's SQ-limit web page, where Python and Matematica codes to calculate the bandgap-dependent SQ-limit for η, V_{oc}, J_{sc}, FF as well as an illustration of key losses can be found[14]. Few values for selected bandgaps have been pulled out and shown in Tab. 2.1. Similarly the detailed balance limit for MJ solar cells can be found by adding bandgaps[15,16].

Semiconductor	E_g[eV]	η[%]	J_{sc}[mA/cm^2]	V_{oc}[V]	FF
Silicon	1.1	32	45	0.8	0.92
GaAs	1.4	33	33	1.1	0.93
GaAsP	1.7	29	22	1.45	0.95

Table 2.1.: Selected values of key parameters according to the SQ-limit using the AM 1.5G spectrum as input.[14]

2.6. Loss mechanisms

The chapter has so far been concerned with idealized semiconductors and solar cells. When regarding realistic solar cells, a number of loss mechanisms has to be taken

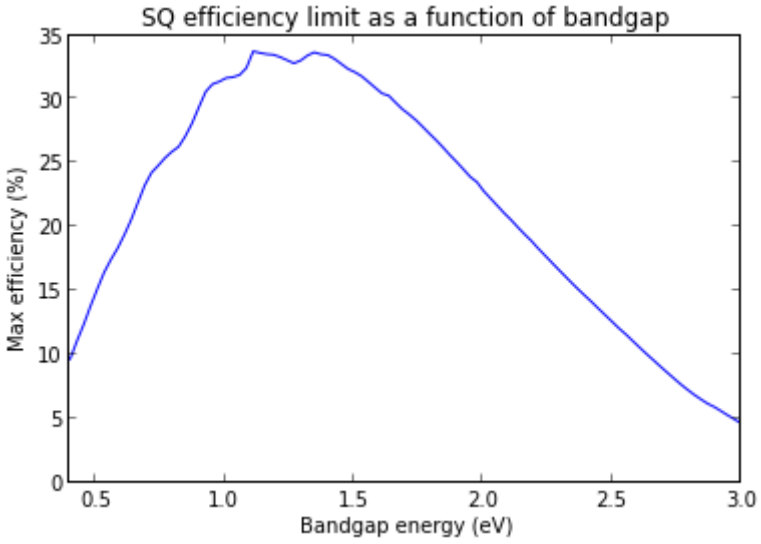

Figure 2.11.: Shockley-Queisser limit for different bandgaps under AM 1.5G illumination. Adapted from [14]

into account, and the solar cell has to be designed to avoid or reduce the losses in order to approach the ideal case. There are three main loss areas: Optical losses due to photons not being absorbed in the solar cell, connection losses, which are losses that occur for solar cells in electrical circuits, and recombination losses, which are carriers that recombine before they are collected.

2.6.1. Optical losses

Optical looses occur when photons in the correct energy range hitting the solar cell are not absorbed. There are tree types of optical losses as shown in Fig. 2.12.a: The loss due to photons hitting the top metallic contact, photons being reflected by the top surface, or photons passing trough the cell without being absorbed.

In order to extract the carriers from the solar cell, an electrical connection must be established in both ends. The top connection, or top contact, will take up some space at the front of the solar cell, and any photon hitting this surface will be reflected or absorbed in the contact. The area of the top contact is kept as small as possible, but a smaller top contact area will increase the series resistance, so there is a tradeoff in cell design. An additional semi-transparent top contact covering the whole surface can also be applied, to increase the series resistance. This will yield additional loses, since it will only transmit around 90% of the light.

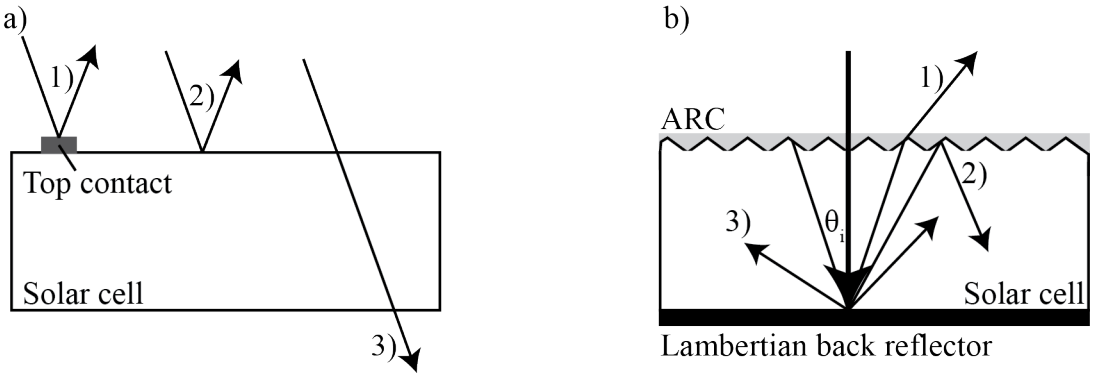

Figure 2.12.: a. The three optical loses in un-optimized solar cells. 1) Photons being reflected by or absorbed in the top contact. 2) Photons being reflected on the front surface. 3) Photons passing through the solar cell without being absorbed. **b.** Solar cell with antireflecting coating, textured front surface (should be randomizing, but is drawn ordered), and Lambertian back reflector . 1) Light hitting the top surface from below with an angle less than $\theta_i = \sin^{-1}(\frac{n_{solar}}{n_{air}})$ can leave the solar cell. 2) Light hitting the top surface with an angle higher than θ_i will be reflected back into the solar cell. 3) The average path length for photons inside the solar cell is $4n_{solar}^2 \cdot thickness$.

When light moves from a medium with one index of refraction n_1 to another medium with a different index of refraction n_2, some of the light will be reflected dependent on the wavelength and angle of incidence. There are two main ways of reducing this reflection: Surface texturing or by applying an anti-reflection coating (ARC). An ARC consist of a thin layer of a material with an index of refraction with the value: $n_{ARC} = \sqrt{n_{air} n_{solar}}$. If the thickness of the coating is $\frac{1}{4}\lambda_f$, all the light with the wavelength λ_f hitting the solar cell directly will be transmitted into the solar cell. The further away a photon's wavelength is from the ideal the greater the likelihood of reflection is, therefore the ARC thickness is selected to transmit the most possible power. Unless the solar cell is constantly held towards the sun, a lot of the light throughout the day will hit the cell at an angle, and the ARC is less efficient at larger angles. The ARC's sensitivity to wavelengths and angles can be reduced by having move than one layer of ARC coating with gradually increasing index of refraction. Usually a two layer ARC is used in a tradeoff between efficiency and cost. Since light is reflected at the same angle they hit surfaces, by texturing the surface you increase the likelihood of a reflected photon hitting the surface twice and being transmitted on the second attempt.

In order to absorb all photons that enter the solar cell, the material need to be thick

enough for all photons to be absorbed. There is, however, a limit to how thick you can make a cell. Aside from the cost of the material, you also need to absorb the photons and create the carriers within a diffusion length of the pn-junction, or the carriers will recombine before being extracted. Therefore, it is ideal to have a solar cell that is physically thin but optically deep, which is obtained by employing light trapping. The simplest light trapping adds a mirror to the back of the solar cell, which effectively doubles the optical path. By surface texturing the front surface the light will refract of the front surface and experience a longer path in the solar cell. By surface texturing the back mirror, as well as the front surface, the optical path length can be significantly enhanced as the light will move back and forth multiple times without exiting the solar cell. In the ideal case it is possible to enhance the optical path length by $4n_{solar}^2$ by using a Lambertian back reflector[17], so if the thickness of the solar cell is t the light will travel an average length of $4n_{solar}^2 \cdot thickness$ in the solar cell. A Lambertian reflector is a completely randomizing reflector and the $4n_{solar}^2$ optical path enhancement is called the Lambertian limit, which is the limit when using ray-tracing to describe the optical pathway. Perfect texturing is very expensive to produce, but many commercial solar cells have simple texturing incorporated.

2.6.2. Resistive losses

When inserting the solar cell into a circuit, additional loss mechanisms are introduced. A model circuit schematic for a solar cell is shown in Fig. 2.13. There are two resistors in the schematic: The series resistance R_s, which is series connected and the shunt resistance R_{sh}, which is connected in parallel with the diode(s). The resistances primarily affect the fill factor. Their influence is easy to see when looking at a solar cells JV-curve, as shown in Fig. 2.14. If R_s is increased the slope at the "voltage" end of the curve towards the V_{oc} will be shallower, which results in a decreased maximum power square. Although the slope of the curve is strongly affected the absolute value of the V_{oc} is not affected. A good approximation of R_s can be extracted from a JV-curve by taking the slope at V_{oc}. A decreased R_{sh} will result in a steeper slope at the "current" end of the curve. R_{sh} can be extracted from the JV-curve by using the slope at J_{sc}. A low R_{sh} can be caused by a short circuit that circumvent the solar diode, which especially for nanowire solar cells can be a real concern. Such a short circuit can be hard to find visually, but will be easy

to spot in an electrical measurement, since the solar cell will act more like a resistor than a diode.

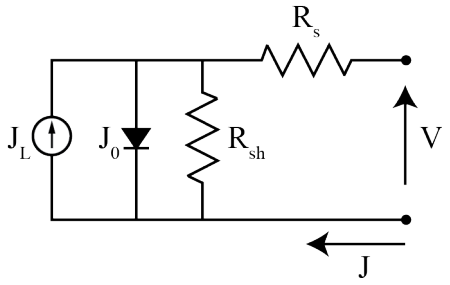

Figure 2.13.: Solar cell schematic. In parallel with the solar energy converter is the normal diode which produces the dark current. The shunt resistance R_{sh} is also parallel to the solar converter, and the series resistance R_s is series connected.

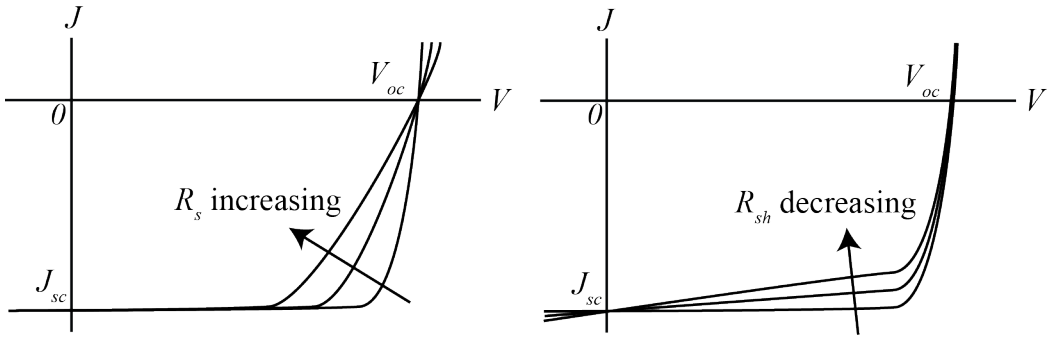

Figure 2.14.: Resistance effects on JV-curve. Increased R_s primarily affects the "voltage" end of the JV-curve, where a swallower slope is the result. Decreased R_{sh} primarily affects the "current" end of the JV-curve, where a steeper slope is the result. Both resistances primarily affect the FF, since neither V_{oc} or J_{sc} are affected much when they are changed.

2.6.3. Recombination losses

Carriers recombine as descried in Sec. 2.3.7, and the recombination of carriers before they are extracted and utilized is a very important loss process in solar cells. In order to avoid detrimental recombination, carriers must be created within a diffusion length of the junctions, so the carriers can diffuse to the junction and be extracted. If there are recombination centers in the proximity of the junction the carriers must also be created closer to the junction than the recombination center, since the centers act as sinks for carriers and cause diffusion towards them. If the recombination

velocity at the recombination site is low the diffusion "pull" will be less, and the carriers can be created closer to the recombination site and still be collected by the junction. High energy photons are usually absorbed quickly, so they are more subject to surface recombination, whereas low energy photons are more subject to bulk and rear contact recombination. Every lost carrier is a carrier that does not contribute to the generated current. Therefore there is a one-to-one correspondence between reduction in current and recombined carriers.

2.6.3.1. Voltage effect

The effect of recombination on the voltage is very complicated. The voltage (Eqn. 2.17) is dependent on the saturation current J_0, and J_0 depends on the fundamental semiconductor parameters, which in turn depends on the recombination. The saturation current for the simplest case, the wide-base pn-junction, is[18]:

$$J_0 = qn_i^2 \left(\frac{\sqrt{D_n}}{\sqrt{\tau_n} N_A} + \frac{\sqrt{D_p}}{\sqrt{\tau_p} N_D} \right) \tag{2.19}$$

This case is not true for most solar cells, however, the affect on J_0 by the material parameters remain, and we can gleam some insight from this idealized case. Since J_0 is working against the J_L we want as small a J_0 as possible. From Eqn. 2.19 this would require small $D_n(D_p)$ or large $\tau_n\,(\tau_p)$ or $N_A\,(N_D)$. We can't do anything about the diffusivities $(D_n\,(D_p))$, which are set by the material and temperature. The minority carrier lifetimes $(\tau_n\,(\tau_p))$ are decreased by any sort of recombination, but the recombination types we can somewhat control are SRH and Auger recombination. SRH recombinations are reduced by having a low recombination center density in the neighborhood of the junction, which is done by using pure crystals and passivating the surfaces. The Auger recombination is kept low by having a low doping. This creates a trade-off between the need to keep doping low to prevent a low $\tau_n\,(\tau_p)$ and generally having a high doping $N_A\,(N_D)$ as required by Eqn. 2.19. The complexity and interplay between the different material properties that causes recombination and reduces the V_{oc}, makes complete control over the doping profile in solar cells incredibly important if a high V_{oc} is to be obtained.

The reduction in open circuit voltage from the ideal is currently the largest problem for nanowire solar cells performance, and at its heart is poor control and knowledge

of the doping profile and high recombination velocity, since the surface with its recombination centers are very close to the pn-junction. It has been shown that poorly controlled doping levels in GaAs nanowires with a core-shell pn-junction could cost lost more than 0.2V in V_{oc} [19].

2.6.3.2. Ideality factor

The ideality factor n is a measurement, of how close to an ideal diode the junction behavior is. The ideality factor is primarily affected by the various recombination processes, and its value is related to the number of carriers involved in the recombination process: SRH/Band-to-band (low level injection) ($n = 1$), SRH/Band-to-band (high level injection) ($n = 2$), Auger $\left(n = \frac{2}{3}\right)$, and SCR recombination ($n = 2$) [18]. The dominant recombination process can therefore, somewhat, be seen by extracting the ideality factor. The ideality factor can be found by plotting the dark $\ln(J)$-V-curve, since the slope is $\frac{q}{nk_BT}$ as can be seen from:

$$\ln(J) = \ln(J_0) + \frac{q}{nk_BT}V \tag{2.20}$$

The slope at intermediate V values should be used, since the low V behavior is dominated by R_{sh} and high V is dominated by R_s. You should also be vary of the temperature and especially temperature changes during measurements. If $n > 2$, the recombination is so high that the ideal diode equation partially breaks down [20,21]. It is most likely that the number of defects in the SCR region is very high, or that there is an ohmic shunt somewhere in the device. If the contacts are not ohmic, but Schottky diodes, these should also be accounted for in order to find the true ideality factor of the diode.

2.6.3.3. Surface passivisation

There are two types of surface passivisation. The number of defects at the surface can be reduced either by having a very clean surface or the dangling bonds can be passivated by attachment of atoms that satisfy the bonds. The second way is to prevent the carriers from reaching the surface by growing a window layer at the top surface. A window layer is a lattice matched, wide bandgap material, and it should be as thin as possible in order to reduce absorption of photons. In Fig. 2.15 is shown

a band diagram of a pn-junction, where a heavily n-doped, window layer has been inserted at the front. If the window layer is heavily doped it creates a barrier for carriers, which keeps the electrons from reaching the surface and reduces surface recombination.

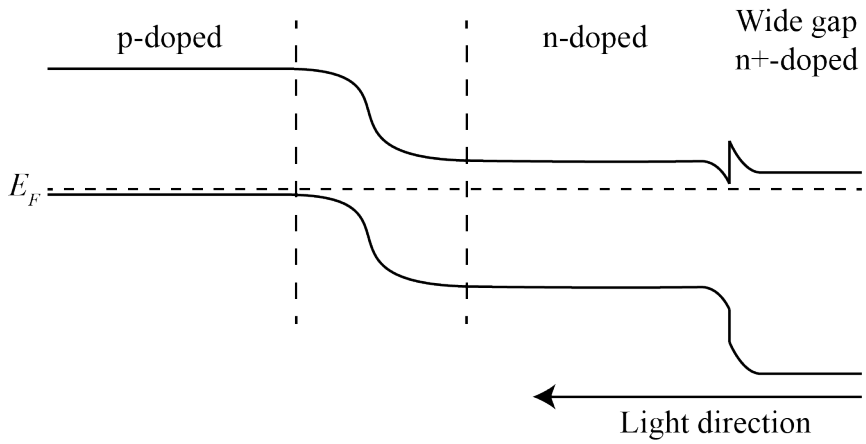

Figure 2.15.: Window layer. A wide bandgap, heavily doped material is placed on the front surface of the solar cell.

2.7. Tunnel junctions

Tunnel junctions are necessary for MJ solar cells, otherwise an opposing, parasitic pn-junction will form between neighboring junctions and reduce the current. By highly doping a pn-junction the width of the SCR is decreased. When the SCR becomes thin enough, the electrons can tunnel from the valence band in the p-side to the conduction band on the n-side. When inserting tunnel junctions into the MJ solar cells the junctions must be made out of a material that has a band gap, which is larger than or equal to the solar junctions above it, since all photons absorbed in the tunnel junction are lost through recombination. If the tunnel junction does not adhere to this bandgap rule, it should be made from a material with a small absorption coefficient so that only few photons are absorbed there. The junction can be quite thin, so unoptimized materials are possible.

3. Crystal Growth

3.1. Introduction

When atoms are brought together at sufficiently low temperatures they form a solid structure. If the structure has no periodic arrangement it is called an amorphous solid. If the structure has a periodic micro structure, and many micro structures or grains form a large structure it is called polycrystalline. If the structure has a periodic micro structure that extends to the whole structure it is called monocrystalline or simply a crystal. Due to the periodic micro structure of three dimensional crystals the macrostructure can be described by a almost unending repetition of its basic building block, which is called the unit cell as seen in Fig. 3.1.

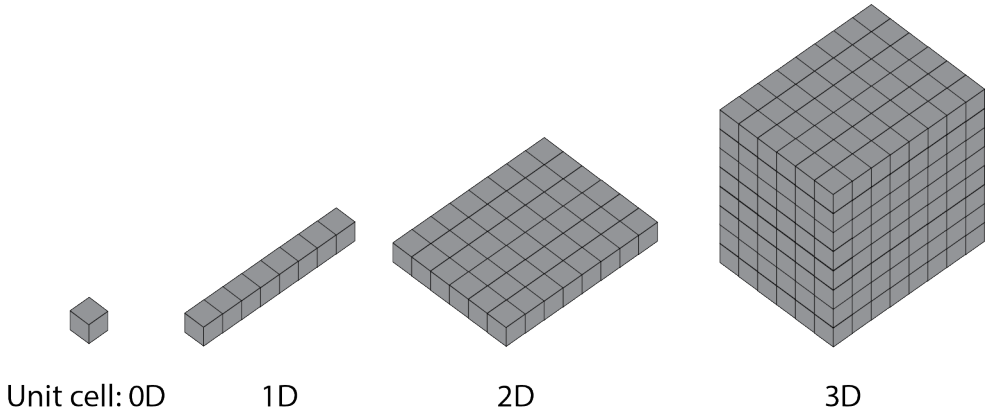

Figure 3.1.: A simple cubic lattice called the Kossel crystal; from the unit cell to three dimension.

By taking billions and billions of unit cells and putting them together in all directions, we are able to grow crystals with very particular physical properties as defined by the atoms in the crystal and the crystal structure. The crystal we are interested in growing and using as the foundation of solar cells are single crystalline semiconductors. For this thesis only the III-V semiconductors, such as GaAs, GaAsP,

InGaP and the group IV semiconductor Si as described in Sec. 2.3 are considered.

There are two ways to describe crystal growth. As a succession of individual atoms involved in a series of processes, or as the interplay between large collections of average atoms. The atomistic description gives a good fundamental understanding of the basic processes involved in crystal growth, and this formalism will be used for a large part of the introduction to crystal growth. This should allow for a good understanding of crystal growth when regarding the atomistic approach, since crystal growth at its heart is the fundamental processes of adsorption/desorption, diffusion and incorporation/dissolution performed billions of times. The atomistic approach, however, has some significant shortcomings especially when trying to predict or explain nanowire growth using computer simulations. There are two reasons for the computational problems: The amount of atoms that has to be taken into account of, and the absolute reaction rates and energies for the different processes are not well known on the atomic scale, especially as a function of experimental growth conditions. The thermodynamic description, or continuum description, is based on phase transitions between large phases. So, rather than individual atoms going through a series of processes, in thermodynamics it is the movement of average atoms and the transitions of average atoms across phase boundaries that decide the growth. Thus, the thermodynamic description is more useful for discussion of experimental results, since e.g. surface energies of crystals and phase transitions can be measured experimentally, whereas e.g. specific energies for individual adsorption sites are only theoretically available. In addition, the theoretical framework for the thermodynamic description of nanowire growth is maturing at the moment, and the work is moving from being used to explain the observed growth to predicting growth.

3.1.1. Transitions

The key processes in crystal growth are governed by transitions, either between positions on the crystals or, in the continuum description, between phases. Therefore, it is instructive to look at a generalized view of transition processes. In 1889 Svante Arrhenius proposed an equation to describe the rate constant of chemical reactions[22]:

$$\Gamma_{Ar} = A \exp\left(-\frac{E_a}{k_B T}\right) \tag{3.1}$$

where Γ_{Ar} is the rate constant of a chemical reaction, A is the number of reaction attempts per second, E_a is the activation energy of the reaction or size of energy barrier for the reaction to occur, k_B is Boltzmann constant and T is the absolute temperature. Though the empirical equation was developed for the chemical reaction between reactants in order to form products in liquids, equations of this form is the basis of crystal growth both for planar growth and nanowire growth.

A generalized transition from one state to another is shown in Fig. 3.2. In the shown transition there is an energy barrier E_a on the transition from state p to q with chemical potentials μ_p and μ_q respectively. If $E_a = 0$ there is no barrier to the transition and every transition attempt from p to q will succeed. There is a difference in the chemical potentials $\Delta\mu = \mu_p - \mu_q$, which means that a transition from q to p has an energy barrier of $E_a + \Delta\mu$. If $\Delta\mu = 0$ the transition from p to q and vice versa would occur with the same probability. We will return to the chemical potential μ later in the chapter.

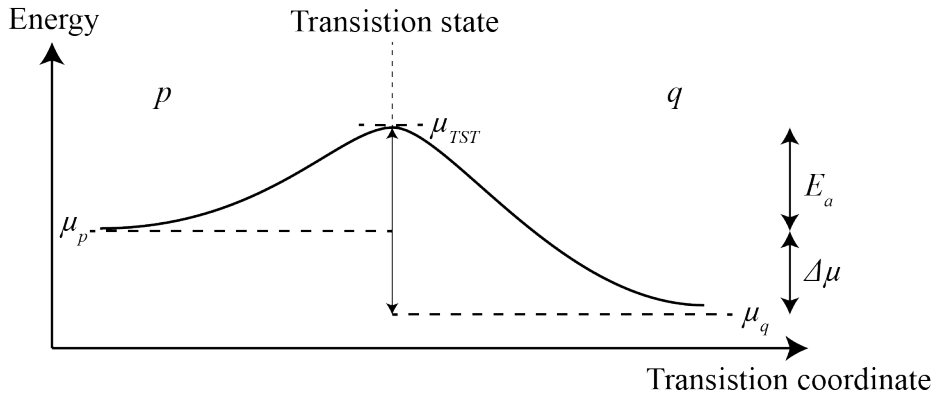

Figure 3.2.: A general transition between state p and q of chemical potential μ_p and μ_q. There is a difference in chemical potential of size: $\Delta\mu = \mu_p - \mu_q$. An energy barrier of E_a has to be overcome for the transition from p to q to take place. In order for the transistion to occur it has to pass through a temporary transistion state with chemical potential μ_{TST}.

3.2. Molecular Beam Epitaxy

The dominant growth systems for nanowire growth are metalorganic chemical vapor deposition (MOCVD) and molecular beam epitaxy (MBE), and this thesis will be centered on MBE growth. MBE is a method for growing high quality crystals, as

illustrated in Fig. 3.3. The growth is performed in a chamber that, using a heat shield and large pumps, is kept at ultra high vacuum ($10^{-10} - 10^{-12}$torr). Molecules or atoms are supplied from very pure sources, kept in special containers called effusion cells, that are heated until the growth species start to sublimate or evaporate from the solid or liquid source. By opening the shutters of the effusion cells the beams are introduced to the chamber. Due to the low pressure of the chamber, and the slow supply of growth species, the growth species movement can be considered as beams rather than a gas, since the particles are so far from each other that they are essentially non-interacting. The mean free paths is on the order of 10^6m at 10^{-10}torr.

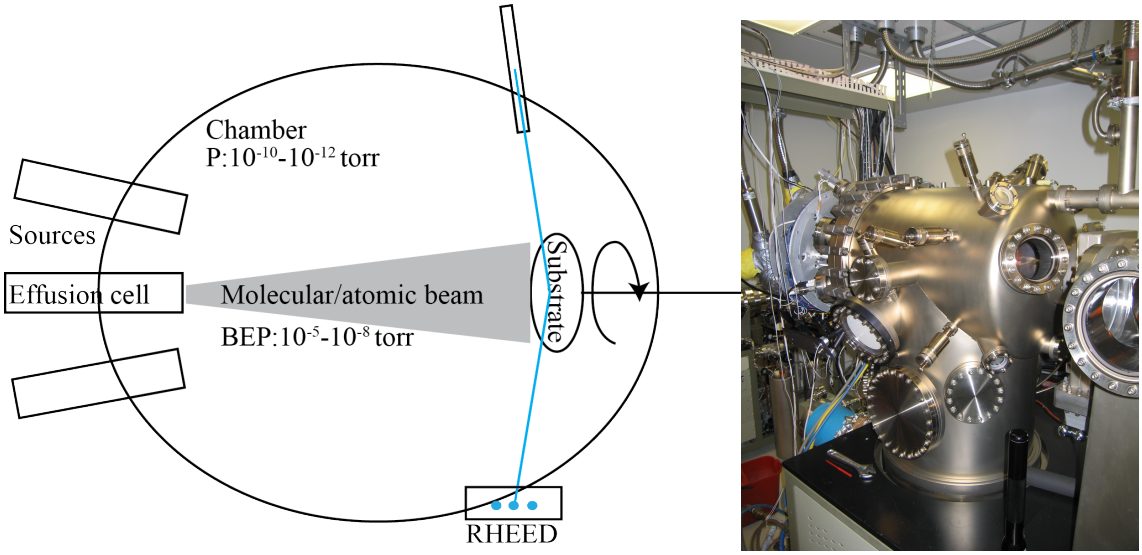

Figure 3.3.: Left: A schematic view of a MBE chamber. **Right:** MBE chamber at NBI. An ultra high vacuum chamber, where sources of very pure materials can be heated to emit a molecular or atomic beam. The beam is pointed at the crystal substrate, which can be rotated and heated to the desired experimental growth temperature. The base pressure of the chamber and beam equivalent pressure (BEP) of the sources can be measured by inserting a pressure gauge at the substrate position. The substrate temperature is measured with a thermocoupler behind the substrate and using a pyrometer from outside the chamber. The in-situ reflection high-energy electron diffraction (RHEED), which probes the surface structure, can also be used to measure the planar crystal growth rate.

Epitaxy means an ordered layer of crystals on top of a crystal, since epi means above and taxis means ordered. The implication is that a foundation for the growth beam is needed, and in MBE growth this foundation is called a substrate. The substrate is a thin crystalline wafer that has been sliced out of a larger ingot. The

slicing produces wafers with particular surfaces most commonly {100} and {111}, but higher index wafers or wafers that are purposely off-cut towards other crystalline directions can also be used. The molecular beams are directed at the substrate, so that the molecules or atoms hit and interact with the substrate. The constitution of and interaction between the substrate and the molecular beams determines what crystal structures are fabricated or grown.

3.3. Planar crystal growth in MBE

MBE growth is one the simplest crystal growth methods, since only pure growth species are involved. There are three phases in planar MBE growth as seen in Fig. 3.4:

1. The vapor phase, which consists of the molecular/atomic beam(s).
2. The adsorbed phase or adsorbate, which are atoms that are bound to the crystal, but can still move around on the surface.
3. The solid phase, which is the growing crystal.

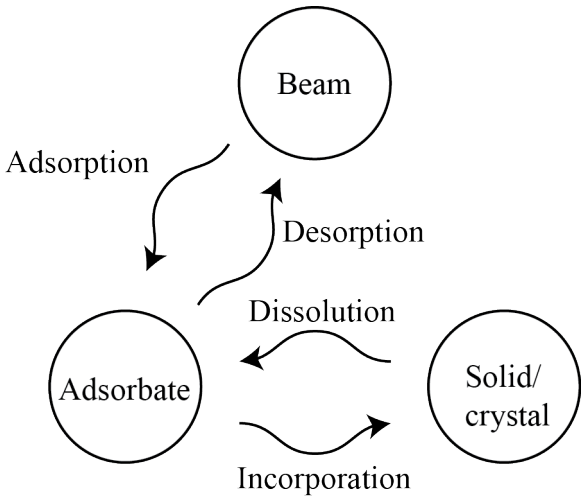

Figure 3.4.: The three phases in planar MBE crystal growth and the phase transition. Molecules/atoms from the beam are first adsorbed, where they can move around on the crystal surface, before they incorporate into the crystal. The transitions are primarily governed by the pressure and temperature in the various phases.

At normal growth conditions the exchange of atoms between vapor and solid will go through the intermediate adsorbate phase, so these phase transitions have been

shown in Fig. 3.4. The adsorbate phase is not a phase in the classical sense, but an intermediate state at the intersection between the vapor and solid phases. It shares many similarities with phases, and it is convenient to use the phase-vocabulary to describe its behavior and transitions between the adsorbate, vapor and solid, so in this thesis it will be referred to as a phase.

3.3.1. Adsorption

When a molecule or atom from the vapor phase hits the substrate they have a probability, through interaction with the substrate and loss of kinetic energy, to become adsorbed on the substrate. Molecules/atoms that are adsorbed, but not stuck in the crystal lattice yet, are called adatoms. There are two types of adsorption: Physiosorption and chemisorption.

Physiosorption or physical adsorption is the weak binding of atoms or molecules to surfaces. The physiosorption is caused by van der Waals forces between atoms in close proximity. Van der Waals forces are caused by mainly attractive forces due to permanent or induced dipoles and repulsive forces due to the Pauli exclusion principle. The sum of the attractive and repulsive forces means that physiosorption can be described as a potential well on the order of 10-100meV, as illustrated in Fig. 3.5. It is important to note that there is no energy barrier to physiosorption, and particles will be caught in the potential well if they loose enough kinetic energy in the interaction with the substrate. In MBE growth, however, it is mostly a transient state for molecules, such as As_2, since the introduced growth material typically can react with the surface atoms and form stronger chemical bonds.

Chemisorption or chemical adsorption is an adsorption where the adatoms and the substrate are bound together via chemical bonds. Chemisorption is a much stronger binding than physiosorption, typically 1-10eV. Unlike physiosorption which has no energy barrier, chemisorption can involve an energy barrier, if there is a need to break chemical bonds before chemisorption can occur, see Fig. 3.5. An example is the breaking of the bond between the two atoms in a physiosorped As_2 molecule before the As atoms can chemisorp to the surface. In practice it is not necessary to categorize which binding mechanism is in play, and in the following the term adsorption will be used instead of physiosorption and chemisorption.

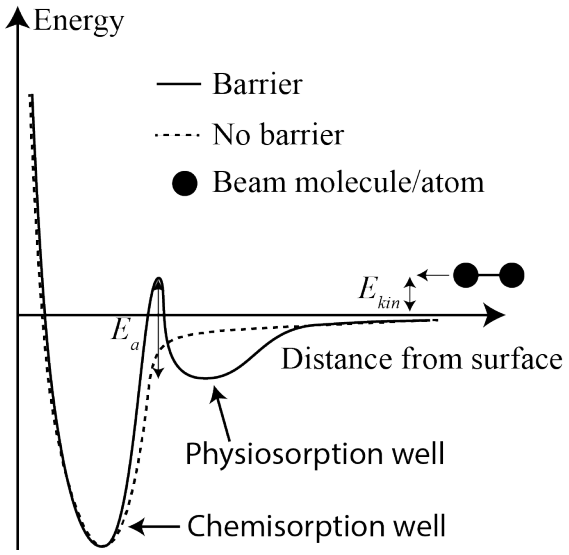

Figure 3.5.: The potential wells of adsorption. If no bond breaking is needed, there is no energy barrier to chemisorption as shown with the dashed line. If bonds have to be broken before chemisorption can proceed the activation energy E_a has to be overcome, Fig. 3.2. The depth of the chemisorped(physiosorped) potential well is on the order of 1-10eV(10-100meV) with a minimum around 1-3Å(3-10Å). The depth of the potential wells are not drawn to scale. The atom/molecule has a kinetic energy E_{kin}, which they loose through interaction with the surface atoms.

3.3.2. Desorption

Desorption is the opposite process of adsorption. If the adatom has enough energy to escape the potential well it is occupying, then the adatom can desorp from the surface. For planar MBE growth the adatom will be lost, since there is nothing to interact with when moving away from the substrate. In order for desorption to take place there is always an energy barrier that needs to be overcome, since adatoms are bound to the substrate. The desorption rate can be written on the Arrhenius form as[23]:

$$\Gamma_{des} = \rho\nu_{\perp} \exp\left(-\frac{E_{des}}{k_B T}\right) \tag{3.2}$$

where E_{des} is the depth of the potential well, and thereby the energy barrier to desorption, $\nu_{\perp}$ is the vibrational frequency of the adatoms normal to the surface, and ρ is the steric factor that accounts for the orientation of molecules and atoms.

This yields an adatom surface time of:

$$\tau_{des} = \frac{1}{\rho \nu_{\perp}} \exp\left(\frac{E_{des}}{k_B T}\right) \tag{3.3}$$

This is the average time an adatom has to incorporate before being desorped and lost to the growth.

3.3.3. Diffusion and Incorporation

Adatoms are bound to the surface, but still not incorporated into the crystal, since they are sitting at energetically unfavorable incorporation positions. Before they desorp, τ_{des}, they can diffuse on the surface or incorporate into the crystal. Diffusion is the movement of adatoms across the crystal surface that is the result of a number of individual hops between neighboring adsorption sites, Fig. 3.6.a.

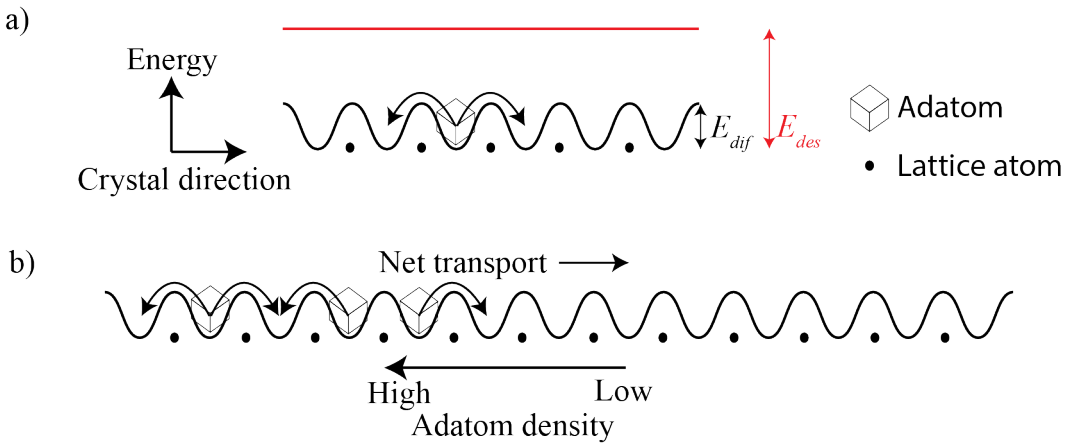

Figure 3.6.: a. Six neighboring potential wells at adsorption sites. A cubic adatom is sitting in one well in the 1-dimensional potential landscape of a single crystal direction. The adatom can hop to neighboring wells by overcoming the energy barrier E_{dif} or desorp by overcoming the desorption barrier E_{des}. Notice it's easier to desorp away from adsorption sites, when the adatom is in a temporary transition state. In reality the energy barriers are changed when an adatom is sitting in an adsorption site, but here the "empty" surface has been sketched. **b**. The random diffusion will cause a net transport of adatoms from high to low density areas.

For an adatom to hop to the next potential well it has to overcome an energy barrier

E_{dif}. The rate by which they do so is given by:

$$\Gamma_{dif} = \rho\nu_{=} \exp\left(-\frac{E_{dif}}{k_B T}\right) \tag{3.4}$$

where $\nu_{=}$ is the vibrational frequency of the adatoms parallel to the surface in the diffusion direction. The energy barrier to diffusion is always smaller than the energy barrier to desorption $E_{dif} < E_{des}$, so an adatom can diffuse quite far before being desorped. If we look at the potential landscape in one crystal direction for a single adatom on a crystal surface it might look like Fig. 3.6.a. The adatom will hop from site to site until it is desorped or finds a deeper potential well. If there, for any reason, is an adatom density gradient on the surface, as in Fig. 3.6.b, the random diffusion will lead to a net transport of adatoms to the low density areas of the surface as described by Fick's law[6]:

$$J_a = -D_a \frac{\partial n}{\partial x} \tag{3.5}$$

where D_a is the diffusivity and $\frac{\partial n}{\partial x}$ is the concentration gradient along the crystals x-direction. The diffusivity is:

$$D_a = a^2 \rho\nu_{=} \exp\left(-\frac{E_{dif}}{k_B T}\right) \tag{3.6}$$

where a is the mean distance between adsorption sites. The interaction between neighboring adatoms is not included in Eqn. 3.5, which will affect the diffusion a bit. However, the net result of an adatom density gradient is diffusion against the gradient even if these interactions are taking into account. Unless there is a localized source of or sink for adatoms the density gradient will disappear quickly.

As an adatom diffuse on the surface, it can meet an empty site in the crystal lattice. If so, it has a probability to incorporate. The incorporation of the adatom will change the potential landscape for the next adatom as seen in Fig. 3.7. Since the adatoms can incorporate, the average time and adatoms spends on the surface is: $\tau_{surf}^{-1} = \tau_{des}^{-1} + \tau_{inc}^{-1}$.

Regarding the crystal surface in one-dimension is a good way of illustrating diffusion,

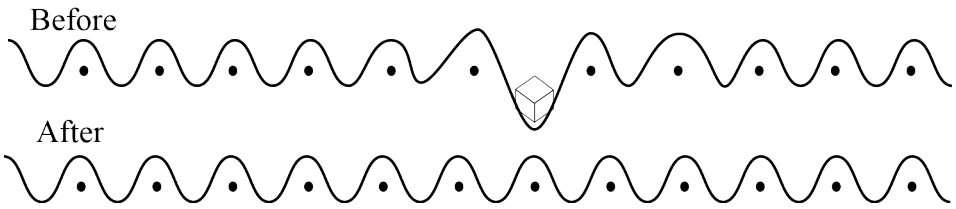

Figure 3.7.: Surface potential landscape before and after incorporation. If there is missing an atom in the top crystal layer the potential landscape is perturbed. When an adatom diffuses into an empty site it incorporates and changes the potential landscape for the next adatom.

desorption and incorporation, but the surface of a crystal is two-dimensional. The surface potential of a section of an idealized crystal is drawn in Fig. 3.8.

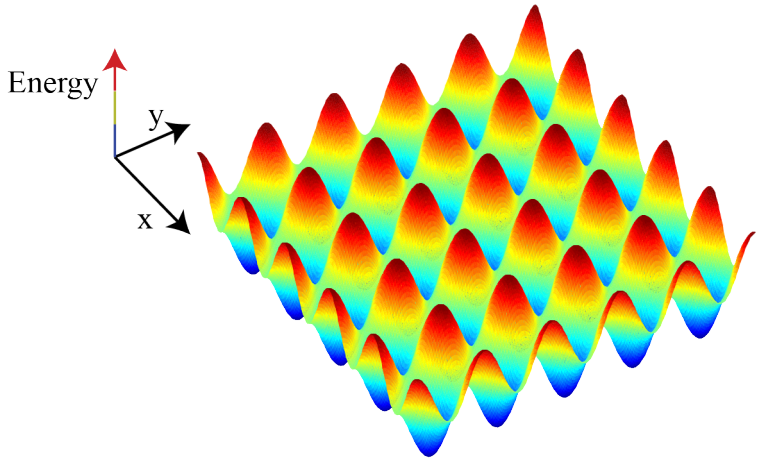

Figure 3.8.: The two-dimensional surface potential energy landscape an adatom will experience. For an adatom vibrating in a potential well certain direction have a smaller energy barrier to diffusion, here it is in the x- and y-direction. When the adatoms vibrates in a potential well it has a probability, as governed by the diffusion energy barrier landscape, to hop to the neighboring potential wells.

Adatoms can diffuse between the potential wells of adsorption sites. The diffusion energy barrier is smallest in certain directions, which are dictated by the underlying crystal. In the figure the lowest energy barriers are between potential wells in the x- and y-directions, and adatoms will therefore diffuse much easier in those directions. Other crystals have different potential surfaces, e.g. there can be different barriers

in the x- and y-direction, or there can be three low energy directions as is the case for hexagonal lattices.

3.3.4. Basic incorporation

Using potential landscapes as seen in Fig. 3.8, or for that matter the even more complicated real crystals will make it hard to understand the basic crystal growth processes. Instead, it is instructive to use Kossel crystals to illustrate the crystal growth processes. If we only consider first neighbor interactions Kossel crystals are basically cubes whose surfaces can bind together to form larger crystal structures. An intermediate state, when building a large crystal out of Kossel crystals, could look like Fig. 3.9.

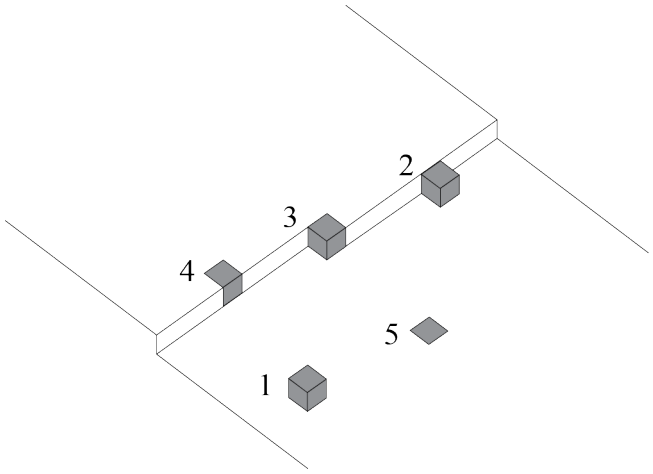

Figure 3.9.: A view of the surface of a Kossel crystal, where a new layer is being formed. The five highlighted Kossel crystals each have a different number of bound surfaces as indicated by the number next to them. 1: An adatom on the surface is the least bound Kossel crystal. 2: An adatom on the step is bound at two surfaces. 3: At the kink site the crystal is being built trough multiple incorporation events. 4: Incorporated atom in step. 5: Incorporated atom in surface. 6: Below the surface with all surfaces bound (not seen).

In the figure are highlighted crystal positions that show Kossel crystals with a different number of bound surfaces as indicated on the figure. To a first approximation the depth of the potential well they occupy is increased in equal steps until all six surfaces are bound. This means that each type of highlighted Kossel crystal would require a different energy both to diffuse and desorp. A higher number of bound surfaces means that a higher energy is needed to move them from their position.

The perhaps most important crystal site is the site with three free and three bound surfaces. This site is called the kink site or half-crystal site. The reason this site is important is that a crystal can be, and is, built using successive incorporation at kink sites, or conversely taken apart by successive dissolutions from kink sites. In addition, the number of free surfaces in the final crystal is unchanged after incorporation at this site, since that position has an equal amount of bound and free surfaces. The unfinished crystal layer thus grows by incorporation at kink sites, which in turn moves the edge of the growing crystal layer forward across the previous layer. The sidewall of the new crystal layer is called a step.

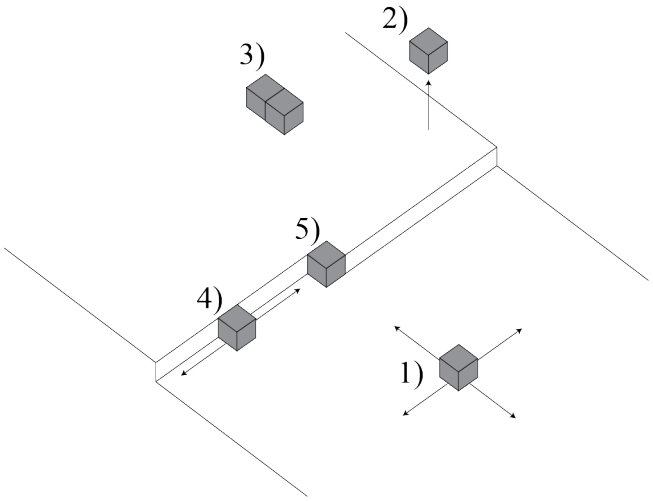

Figure 3.10.: Kossel crystal adatom processes. A Kossel crystal adatom can be involved in five different situations: 1) Adatom diffusion on surface. 2) Adatom desorption from surface. 3) Cluster formation via adatom bonding. Clusters can also form on steps. 4) Adatom step diffusion 5) Adatom incorporation or dissolution at kink site.

The adatom movement routes and incorporation positions are critical to crystal growth. Fig. 3.10 show the movement possibilities of Kossel adatoms which are: 1) Diffuse on the surface of the crystal. The diffusion barrier will always be smallest in certain directions dictated by the potential landscape, so some directions will have a higher diffusion rate. Since the Kossel crystal has a cubic lattice the diffusion directions are as indicated. 2) Desorp from the surface. 3) Meet other adatoms and bind together to form clusters. We will return to clusters later, but their formation is how new crystal layers are started. 4) Diffuse along a step. Adatoms on a step are more tightly bound to the crystal (a deeper potential well) than surface adatoms. They are more likely to diffuse along the step than detaching from the step and

diffuse on the open surface, since there is an additional energy $\Delta\mu$ to be paid on top of the E_{dif}. 5) Incorporate at a kink site which grows the crystal. All five processes are happening simultaneously and in order to grow high quality crystals the crystal grower must choose the right growth parameters. If the flux is too low there will be more desorption than adsorption and the crystal will not grow. Too high a flux and the growth may not happen in an ordered layer-by-layer fashion. Too low a temperature and adatoms will not diffuse, and the growth will become unordered as atoms incorporate where they are adsorbed. Too high a temperature and it becomes impossible to keep desorption below adsorption and the crystal will start to dissolve.

3.4. Thermodynamics

Planar crystal growth is basically as described above, even though we have used the simple Kossel crystal to describe the processes. The described processes have been mostly concerned with individual atoms, and not much with their interaction. Without thermodynamics we can not get into the heart of crystal growth since the unending number of atoms, which are involved, are best described through collective interactions, as constrained by the basic processes, performed by many average atoms in the continuum limit[24]. The continuum limit, or description, says that the thermodynamic properties of the involved materials can be described by continuous functions of position and time. In the continuum limit an atomic state is described by the average values and properties of the atoms in the microstate that is made by selecting a small volume around the atomic state, which means that neighboring microstates will be described by almost identical parameters. If the neighboring microstates are inside different phases the values and properties of the microstates can be used when describing their interaction. This means that in the continuum description we can use macroscopic properties, such as chemical potentials of phases, to describe the interaction at the atomic level.

3.4.1. Chemical potential

All processes in crystal growth are governed by the minimization of the systems free energy, more specifically the minimization of Gibbs free energy[25]:

$$G = U + PV - TS \tag{3.7}$$

where U is the internal energy, P is the pressure, V is the volume, T is the absolute temperature, and S is the entropy. The perhaps most important aspect of a crystal phase is the chemical potential, which has been hinted at above. The chemical potential is the change in Gibbs free energy when one particle is added to or removed from the phase, or said in another way the derivative of Gibbs free energy under constant pressure and temperature with respect to the number of particles in the phase:

$$\mu_\alpha = \frac{\partial G_\alpha}{\partial N_{\alpha\, P,T}} \tag{3.8}$$

The system will seek to minimize its Gibbs free energy, since from Eqn. 3.7 we can see that maximizing the entropy will minimizing the Gibbs free energy. Maximizing the entropy, according to the second law of thermodynamics, will lead to a system in equilibrium.

3.4.2. Equilibrium

Two phases α and β are in equilibrium if $\mu_\alpha = \mu_\beta$. The system's energy doesn't change if one atom transitions between phases in equilibrium, so no net transfer of particles will take place between the two phases $dN_\alpha = dN_\beta = 0$. We have seen state equilibria above. When an adatom hopped from one potential well to the next during diffusion the systems free energy was unaffected. We could state that one potential well was in equilibrium with the neighboring potential well, but those equilibria are not very interesting. In crystal growth the phase equilibrium are the important ones. If $\mu_{adsorbate} = \mu_{solid}$ than as many adatoms will incorporate into as dissolve from the crystal, which means that the crystal will not grow.

3.4.3. Supersaturation

If the pressure or temperature of one phase is changed away from the equilibrium conditions a net transfer of particles is made possible due to supersaturation, which is defined as:

$$\Delta\mu_{\alpha\beta} = \mu_\alpha - \mu_\beta \tag{3.9}$$

If $\Delta\mu_{\alpha\beta} > 0$ there is a thermodynamic driving force for the transfer of particles from α to β, since the systems free energy can be reduced with $\Delta\mu_{\alpha\beta}$ by transferring an atom from α to β. For planar MBE crystal growth to occur via the phases and transitions in Fig. 3.4 there has to be established and sustained a situation where:

$$\mu_{vapor} > \mu_{adsorbate} > \mu_{solid} \tag{3.10}$$

Notice that crystal growth occur under constant out-of-equilibrium conditions, otherwise the atomic conveyor belt will stop and growth cease. The conditions in Eqn. 3.10 is not sufficient for the transitions to occur, since energy barriers as seen in Fig. 3.2 might hinder or prevent the phase transitions. The supersaturation conditions in Eqn. 3.10 can be established by reducing the substrate temperature, or by increasing the pressure(flux) in the vapor(beam). The supersaturation provides the driving force for crystal growth and the size of the supersaturation is very important, since a number of things can happen dependent on the driving force in the system. In addition, it is important to remember, that the thermodynamic equations are constrained by the real crystals on the atomic size scale.

3.4.4. Equilibrium shape

The specific surface free energy γ is the work required to create a new unit of surface. The new surface can be created by growing a new surface by incorporation or by removing the existing surface by dissolution to expose the underlying surface. The system is striving to reduce its free energy, and a large part of that process is to have surfaces with a low surface energy. To a first approximation the surface free energy is the sum of the energies of the broken bonds per unit area. In general low index surfaces {100}, {110}, {111}, ... have the lowest surface energy, and will be the surfaces typically seen in crystal growth.

If the volume of the crystal is kept constant the free energy can only be reduced by changing the shape of the crystal. If we assume the crystal is suspended in e.g. a liquid of the same material the crystal will expose the surfaces that minimizes Gibbs surface free energy [26]:

$$\triangle G_j = \sum_j \gamma_j \xi_j \tag{3.11}$$

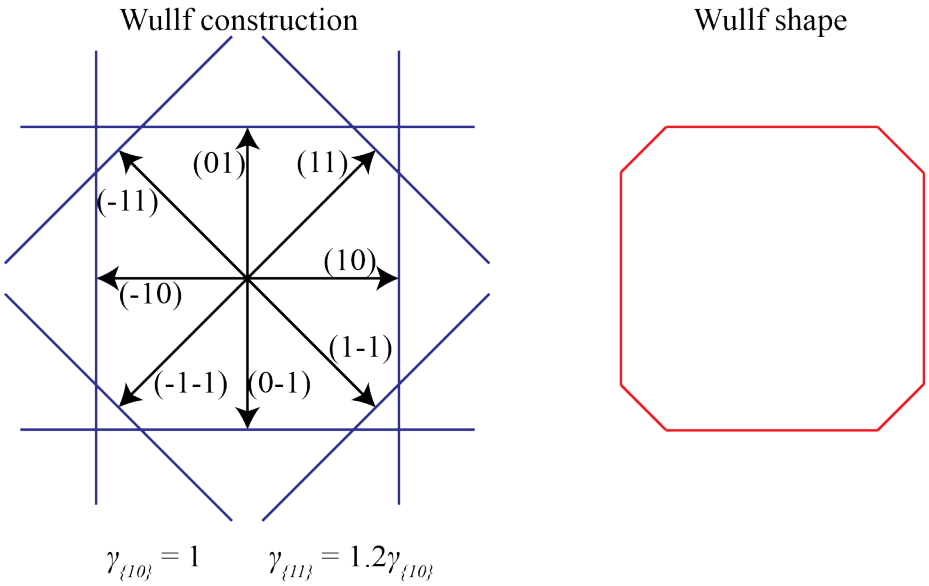

Figure 3.11.: The Wullf construction is made by drawing a vector with the length of the specific surface free energy in the direction of the surface for each surface. In principle all possible surfaces should be used, but only the low energy surfaces are needed, which here consist of the surface groups {10} and {11}. At the end of each vector an unending line perpendicular to the vector is drawn. The Wullf shape or equilibrium shape is the area, volume in 3D, which is enclosed by the inner envelope.

where γ_j is the specific surface free energy per area and ξ_j is the surface area of the j^{th} surface. The minimized Gibbs free energy shape is the equilibrium shape and is called the Wullf shape. If you know the surface energies of all surfaces or at least their relation it is possible to construct the equilibrium shape. The Wullf shape is constructed by from the center of the crystal drawing a vector which is normal to all possible surfaces with the length $v_j = \phi\gamma_j$, where v_j is the length of the vector of the j^{th} surface and ϕ is the proportionality factor, which is the same for all surfaces[27]. The equilibrium shape of a liquid in a vapor is a sphere, since the entire surface has the same surface energy. Different crystal surfaces, however, have different surface energies. This means that a solid crystal forming in a liquid is not spherical but some approximation of a spherical shape. A two dimensional Wulff construction is seen in Fig. 3.11 where only the low energy facet groups {10} and {11} are used to construct the equilibrium shape. It is possible to find the equilibrium shape by using the Wulff construction, but the opposite is also true. If you are given the Wulff shape you can ascertain the relationship between the surface energies, though

not the absolute values.

3.4.5. Wetting

The Wullf construction gives the equilibrium shape of a crystal suspended in a liquid or a gas, which is rarely interesting in planar crystal growth. We are interested in the equilibrium shapes of crystals with some relation to the underlying substrate. The simplest, and often relevant case, is the case of an equilibrium shape attached to a non-deformable surface, Fig. 3.12.

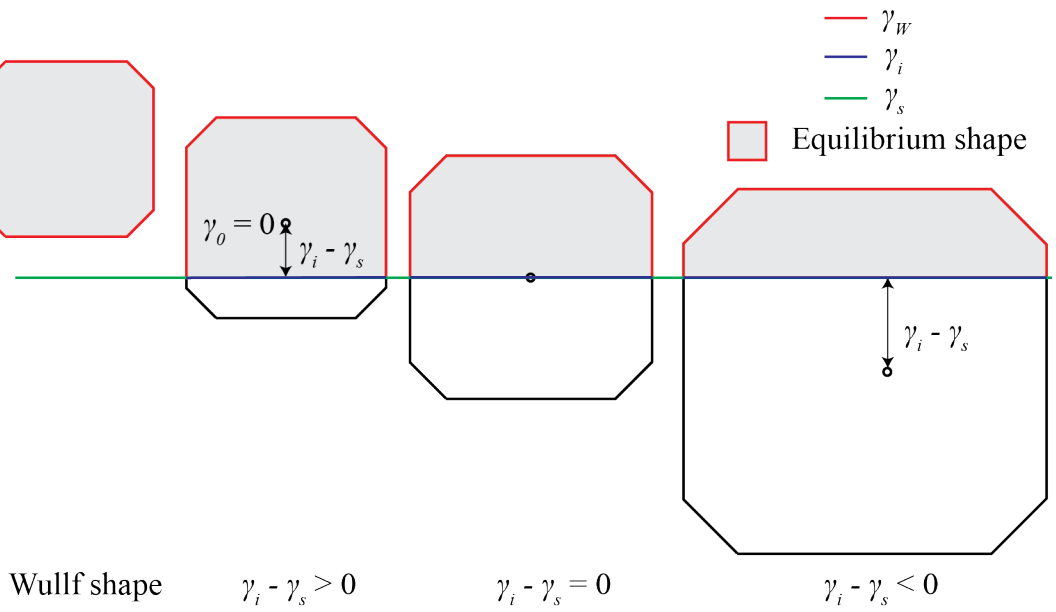

Figure 3.12.: Winterbottom construction for non-deformable substrates. The Wullf shape with surface energy γ_W on the left is attached to a non-deformable substrate with surface energy γ_s as represented by the green line. The difference between the interface energy γ_i and the substrate's surface energy $\gamma_i - \gamma_s$ yields how far below or above the surface the zero point $\gamma_0 = 0$ is situated.

Winterbottom[28] showed that the difference of the interface energy between the equilibrium shape and the substrate γ_i and the surface energy of the substrate γ_s defines where the zero point $\gamma_0 = 0$ lies in relation to the substrate. The reason is, that the system (crystal and substrate) is trying to reduce its surface energy. If the surface energy of the substrate γ_s is large compare to the interface energy γ_i the systems energy is reduced by increasing γ_i at the expense of γ_s. The total crystal volume, gray area, is conserved, which means that the sign and size of the $\frac{\gamma_i}{\gamma_s}$ ratio

decides how far into the substrate the crystal is "submerged". If $\gamma_i - \gamma_s = 0$ the substrate will "cut" through the equilibrium crystals center. If, however, $\gamma_i - \gamma_s > 0$ more than half the equilibrium crystal will be above the substrate, and vice versa for $\gamma_i - \gamma_s < 0$. In the most extreme cases the crystal will float and be the Wullf shape (no wetting) or become a single atomic layer covering the substrate (complete wetting). In order to minimize the free energy the Wulff shape can be rotated to give the lowest free energy.

3.4.6. Nucleation

Gibbs was the first to theorize that for a new phase to form it has to start from small clusters of the new phase. A cluster is a collection of atoms with the same properties as the new bulk phase except that the clusters are very small. In planar crystal growth using MBE, the most interesting phase formation is the formation of a crystal on top of the substrate from the vapor of more likely adsorbate phase. In order to form the clusters there will be a change in the systems Gibbs free energy. Under constant temperature the energy change has two parts:

$$\Delta G = \Delta G_{VolumeFormation} + \Delta G_{SurfaceFormation} \tag{3.12}$$

If the mother phase is supersaturated, the system can reduce its free energy by forming the volume $\Delta G_{VolumeFormation} = -n\left(\mu^{\infty}_{adsorbate} - \mu^{\infty}_{solid}\right)$, where n is the number of atoms transferred between phases. The ∞ superscript signifies that it is the chemical potentials of large phases without size effects that is used. it is the In order to form the volume the system is also forming a new surface. This increases the free energy by: $\Delta G_{SurfaceFormation} = \gamma\xi_{solid}$, where ξ_{solid} is the surface area of the formed solid. This means that when the inequality:

$$n\left(\mu^{\infty}_{adsorbate} - \mu^{\infty}_{solid}\right) > \sum_j \gamma_j \xi_j, \tag{3.13}$$

holds the system can reduce its free energy by transferring n atoms to the solid phase. From the inequality can be seen that a large supersaturation will benefit the phase transfer, but it is equally important that a small γ combined with a small ξ_{solid}, since it makes the transition easier. Though crystal growth is never performed

under equilibrium conditions, the equilibrium shape is the shape that will cause the smallest surface free energy increase. That means that clusters with the equilibrium shape are the clusters that are most likely to nucleate the growth of a new crystal layer. The characteristic of nucleated growth is that an energy barrier has to be overcome in order to form a stable cluster (nucleus), but once the nucleus is formed the layer will quickly grow as the nucleus' kink sites are used to form the crystal layer. On a smaller scale the kink sites also has to be nucleated on the step edges, but if it is possible to nucleate on the substrate surface the step nucleation will not be limiting the crystal growth.

There are two kinds of nucleation. Homogeneous nucleation is when a new phase forms without external interaction. This is e.g. what happen when vapor condenses and forms liquid drops. In crystal growth heterogeneous nucleation is much more common. Heterogeneous nucleation is when the nucleation start at some impurity or surface. Homogenous nucleation is typically assumed to form equilibrium shapes defined by their Wullf shape Fig. 3.11, whereas heterogeneous nucleation forms equilibrium shapes as defined by their Winterbottom construction Fig. 3.12.

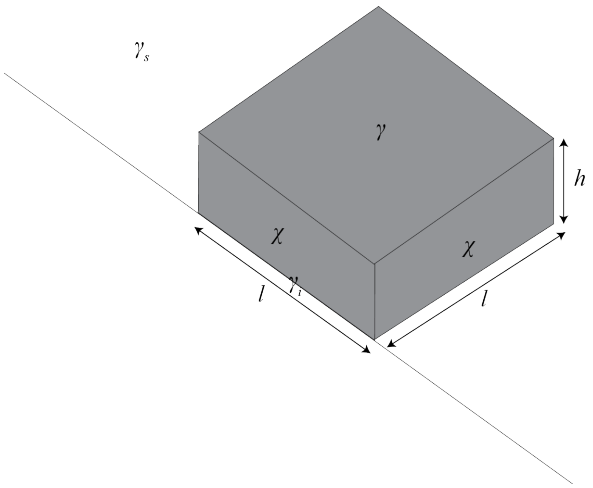

Figure 3.13.: A schematic of a Kossel crystal nucleus of height h and side length l on a foreign substrate. The substrate has a surface energy of γ_s, the nucleus has a surface energy of γ, the interface energy between substrate and nucleus is γ_i and the sidewall energy is χ. If h is a single layer the nucleus is a 2D nucleus. The relationship between $\gamma, \gamma_s, \gamma_i$ determine the equilibrium h/l ratio.

In Fig. 3.13 is drawn a Kossel crystal nucleus with height h, sidewall length l, surface energy γ and sidewall energy χ. It is situated on top of a substrate that has the surface energy γ_s. The crystal interface between the substrate and the nucleus

has the interface energy γ_i. If only first neighbor interactions are considered the equilibrium shape is cubic, and the height will be defined by the wetting $\Delta\gamma = (\gamma + \gamma_i - \gamma_s)$. The wetting is a measure of whether the attractive forces between substrate and nucleus are stronger than the forces between the atoms in the nucleus. If the Kossel nucleus has a height of a single crystal layer the nucleus is a 2D nucleus, while a higher nucleus is considered a 3D nucleus. The work of formation or change in Gibbs free energy for a square 2D nucleus is[23]:

$$\Delta G = -\frac{l^2}{s_c}\Delta\mu + l^2\left(\gamma + \gamma_i - \gamma_s\right) + 4l\chi \tag{3.14}$$

where s_c is the area of an atom in the 2D crystal, $n = l^2/s_c$ is the number of atoms in the nucleus, l is the sidewall length and χ is the specific edge energy. The first term on the left is the volume creation which at positive supersaturation $\mu_{adsorbate} > \mu_{solid}$ reduces the free energy. The second term is the creation of top surface $(l^2\gamma)$, which always increases the free energy, and creation of bottom surface $(\gamma_i - \gamma_s)$ which can be both positive, zero and negative. The third term is the creation of the sidewalls, which also increases the free energy. The change in free energy is a interplay between the free energy lowering volume formation and the free energy increasing surface formation. Adding atoms to the nucleus increases the systems free energy until a critical number of atoms have been added, after which the free energy of the system is reduced by adding atoms to the nucleus. This limit is reached when $\Delta G = 0$ and can for the square 2D nucleus be described in terms of a critical sidewall length::

$$l^* = \frac{2\chi s_c}{\Delta\mu - s_c\left(\gamma + \gamma_i - \gamma_s\right)} \tag{3.15}$$

This means that the formation work for the critical nucleus is:

$$\Delta G^*_{2D} = \frac{4\chi^2 s_c}{\Delta\mu - s_c\left(\gamma + \gamma_i - \gamma_s\right)} \tag{3.16}$$

Substituting $\Delta\mu$ from Eqn. 3.15 into Eqn. 3.16 the formation work of the critical nucleus is $\Delta G^*_{2D} = 2l^*\chi$, and is in fact a specific instance of the general solution for

2D nuclei[29]:

$$\Delta G^*_{2D} = \frac{1}{2}\sum_n \chi_n l_n \tag{3.17}$$

where χ_n is the specific edge energy and l_n is the length of the edge. The work of formation is the energy barrier that the system has to overcome in order to form a stable cluster that can nucleate a new crystal layer. The smallest energy barrier is the one associated with the crystals equilibrium shape, which in the above case was a square 2D nucleus.

An instructive special case is when the 2D nucleus is made of the same material as the substrate. In this case: $\gamma_i = 0$, $\gamma_s = \gamma$ and $\gamma + \gamma_i - \gamma_s = 0$. The energy cost for creating a stable nucleus on the same substrate is then not the cost of creating a new surface, since the nucleation is also removing a free surface below it. Instead it is the creation of the new edge around the cluster which cost energy to complete. This yields the critical length:

$$l^* = \frac{2\chi s_c}{\Delta\mu} \tag{3.18}$$

with work of formation:

$$\Delta G^*_{2D} = \frac{4\chi^2 s_c}{\Delta\mu} \tag{3.19}$$

Recalling that $n^* = \frac{l^*}{s_s}$ and substituting Eqn. 3.18 into Eqn. 3.19 we get:

$$\Delta G^*_{2D} = n^* \triangle\mu \Rightarrow n^* = \frac{4\chi^2 s_c}{\Delta\mu^2} \tag{3.20}$$

Which shows that by increasing the supersaturation the critical number of atoms in the stable nucleus deceases. At sufficiently high supersaturation the critical nucleus becomes a single atom.

The competition between the lowering of free energy due to volume creation and free energy increase due to surface creation is illustrated in Fig. 3.14 for a nucleus consisting of the same material as the substrate. The figure shows the work of formation from Eqn. 3.14 split into the volumes ($-l^2$) dependence and surface (l)

dependence. At the critical length l^* the volume creation overtakes the edge creation, and the systems energy barrier is the critical work of formation. Though the systems total free energy is not reduced at l^* every additional atom added after reaching the critical limit will reduce the free energy.

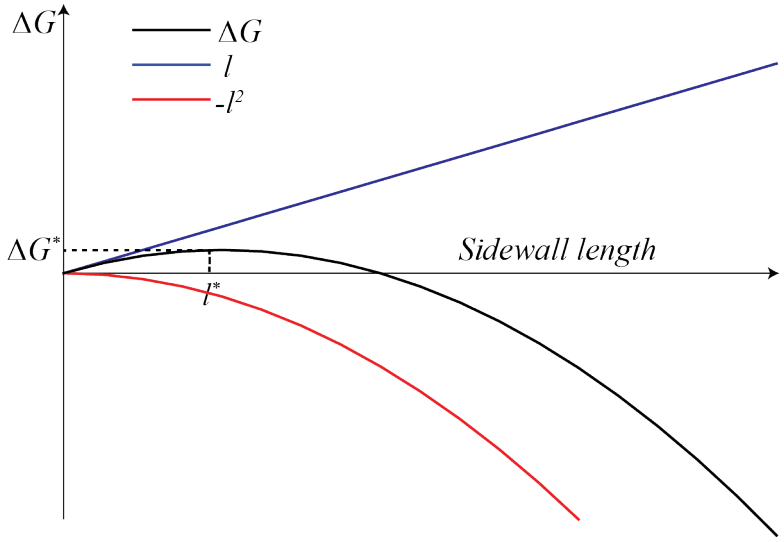

Figure 3.14.: Gibbs free energy change as a function of sidewall length for a cluster forming on a substrate of the same material under constant supersaturation. The critical length can be very long, or shorter than the distance between two atoms in the crystal.

The work of formation for 3D nucleus, where the critical volume is $V^* = l^{*2}h^*$ and the equilibrium shape is $h^*/l^* = (\gamma + \gamma_i - \gamma_s)/2\gamma$, is[23]:

$$\Delta G^*_{3D} = \frac{32\gamma^3 v_c^2}{\Delta\mu^2}\frac{(\gamma + \gamma_i - \gamma_s)}{2\gamma} \tag{3.21}$$

The Gibbs free energy as a function of supersaturation for different wetting conditions can be seen in Fig. 3.15. If $\Delta\gamma < 0$ the attractive forces between substrate and nucleus are strongest and the 2D nucleation will be favored. Nucleation can even occur under undersaturation until $\Delta\mu - s_c(\gamma + \gamma_i - \gamma_s) = 0$ where nucleation becomes thermodynamically forbidden. When $\Delta\gamma = 0$, e.g. when the substrate and nucleus is made of the same material, 3D nucleation is forbidden and 2D nucleation will always take place under supersaturation. When $\triangle\gamma > 0$ and wetting is incomplete 3D nucleation is favored at low supersaturation. 2D nucleation is forbidden until the supersaturation reaches the value: $\Delta\mu_0 = s_c(\gamma + \gamma_i - \gamma_s)$. Beyond the critical supersaturation $\Delta\mu_{cr} = 2s_c(\gamma + \gamma_i - \gamma_s)$ 2D nucleation becomes as likely as

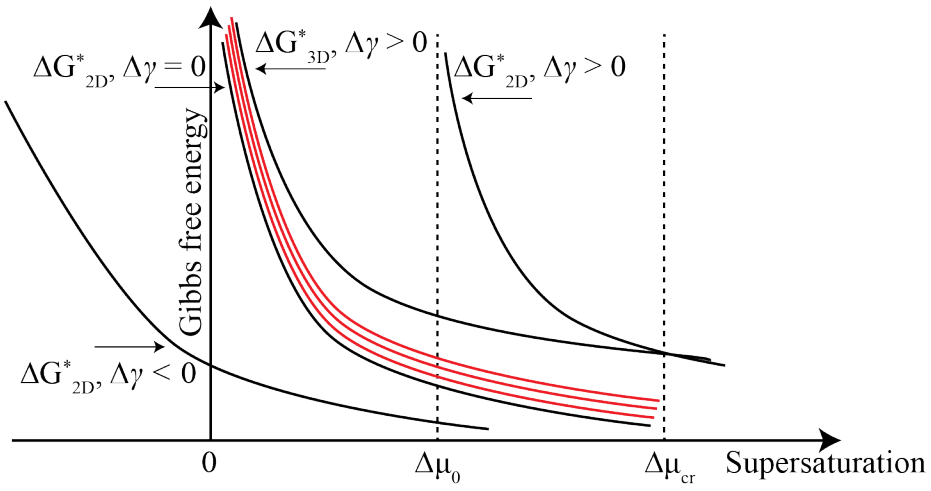

Figure 3.15.: Gibbs free energy change for critical nuclei as a function of supersaturation for Kossel crystals with different wetting conditions. The black curves are for equilibrium crystal shaped nuclei, and the red lines are examples of curves for non-equilibrium shaped 2D nuclei when $\Delta\gamma = 0$.

3D nucleation. Disregarding size effects the equilibrium shape of the 3D nucleation is conserved, for smaller nuclei eventually the height becomes a single atom layer, which is the definition of 2D nucleation. In Fig. 3.15 are also sketched a few red lines, which indicate critical nucleus that are not the equilibrium shape. It is just to illustrate that there will also be formed clusters that are not the equilibrium shape, they are just less likely to form in a stable manner. Especially, at large supersaturations non-equilibrium shaped nuclei will become more common.

If the critical nucleation size is less than one atom no nucleation barrier exist, and the growth is no longer nucleation limited. A growth that is not nucleation limited will be limited by the available growth material. When the available growth material is small, compared to a single layer, the supersaturation will drop after a nucleation event. The pressure, and thereby supersaturation, will drop due to growth species quickly being removed from the source phase due to kink site incorporation. This is a very important process in nanowire growth as we shall see later.

3.4.6.1. Nucleation rate

As seen above the system has to overcome an energy barrier in order to form a stable nucleus. For planar growth we are not very interested in individual nucleation events. Rather, we are interested in the steady state nucleation rate, which is the nucleation

rate when there is always the same number of critical nuclei available for the system to continue its growth. The steady state nucleation rate is[23]:

$$J_s = \omega^* Z c_1 \exp\left(-\frac{\Delta G^*}{k_B T}\right) \tag{3.22}$$

where ω^* is the attachment rate of atoms to the critical nucleus, Z is the the Zeldovich factor[30], c_1 is the steady state concentration of single unit large clusters and ΔG^* is the appropriate critical work of formation. The clusters that are interesting, from a nucleation perspective, are clusters with a Gibbs free energy of formation within $k_B T$ of ΔG^*[31], which the Zeldovich factor includes in the calculation. In this way, the Zeldovich factor accounts for the systems deviation form the equilibrium state, since both clusters that are a little bit smaller or larger than the critical nucleus can nucleate a new layer, as well as clusters with a shape that departs slightly from the equilibrium shape. As an example the 2D nucleation Zeldovich factor is:

$$Z_{2D} = \frac{1}{n^*}\sqrt{\frac{\triangle G^*_{2D}}{4\pi k_B T}} \tag{3.23}$$

The nucleation rate is practically zero below the critical supersaturation after which it rises quickly by many orders of magnitude. That means that no new crystal layer will form unless the supersaturation in the adsorbate phase is sufficient. On the other hand, *if* the supersaturation *is high enough* a stable nucleus *will form* and new crystal layers will follow. Under nucleation limited growth, the J_s will control the growth rate of the crystal.

3.5. Realistic conditions

Planar crystal growth is as described above. The phases and transition follow more or less the idealized conditions. The system's quest to minimize the free energy is what governs the growth, and the supersaturation between the phases is what drives nucleation and incorporation. The crystal grower must establish growth conditions under which the system energetically wants to form the crystal that the grower is trying to grow. Most real crystals are a little bit more complicated than Kossel crystals and some of the most important deviations are worth mentioning.

3.5.1. Surface reconstruction

Real crystal surfaces don't behave as Kossel crystals, where the top atoms have the exact same internal positioning as atoms millions of layers below the surface. Rather the top few atomic layers of the crystal will have a different internal position compared to the bulk atoms. The top atoms, unlike bulk atoms, have outer electrons that are not bound. These dangling bonds have a high energy, so the top atomic layers will move internally in order to somewhat share electrons and reduce the surface free energy. This movement is called surface reconstruction and can be important during crystal growth, since the adatoms are interacting with the reconstructed surface rather than the bulk construction. In addition, the reconstruction will change dependent on temperature and pressure, which again can change the desorption, diffusion, incorporation and nucleation parameters. For example the much investigated (100)GaAs surface has 14 different reconstructions dependent on beam fluxes and temperature[32]. The surface reconstructions are mostly ascertained experimentally using surface probes such as RHEED, which can probe large surfaces reconstruction. Any ex-situ probing of the experimental surface has to be taken with a grain of salt, since the surface has been removed from the growth environment and have experienced different temperatures and pressures. For nanowire growth it is particular tricky to find the reconstruction of the sidewalls during growth, since in-situ measurements of the sidewalls are still quite rare, therefore we have to rely heavily on ex-situ measurement.

3.5.2. Other diffusion mechanisms

Single atom movement across a simple potential well landscape is not the only type of diffusion[33]. Adatoms can also tunnel through the diffusion energy barrier. Adatoms move through exchange with surface atoms, which cause the surface atom to become an adatom. Surface vacancies can also move when neighboring atoms moving into the vacancy position, much like holes moves in the valence band of a semiconductor. Adatoms can also hop further than to the neighboring potential well. Additionally, diffusion involving more than one adatom can occur, so e.g. molecules or clusters can move across the surface. But again the diffusion is governed by Fick's law Eqn. 3.5, and we are not particular interested in the exact diffusion process.

3.5.3. Strained nucleation

When growing crystals we are often interested in combining the qualities of different materials. For solar cells the most important challenge lies in combining materials with complimentary bandgaps. Additionally, there can be financial consideration, since it would be cheapest to grow everything on a silicon substrate. The difference between 2D and 3D nucleation above concerned the wetting as defined by $\triangle\gamma = \gamma + \gamma_i - \gamma_s$. Wetting is an important part of the nucleation, but something else is just as important. To grow a crystals on top of a foreign crystal the two crystals have to fit together. This means that they must have the same or matching crystal structure and the distance between the atoms in the structure must also fit. If the two materials don't fit together the growth becomes amorphous or polycrystalline instead of the desired pure crystalline growth. Some times only the interfaces crystal quality becomes poor, but more likely the faults at the interface will reach far into the growing crystal. This fact has e.g. resulted in poor performance of planar GaAsP solar cells grown on silicon[34]. If you want large areas of crystal covered by other crystals they need to fit, otherwise the misfit will be accommodated by straining one or both crystal and possibly cause dislocations at the interface.

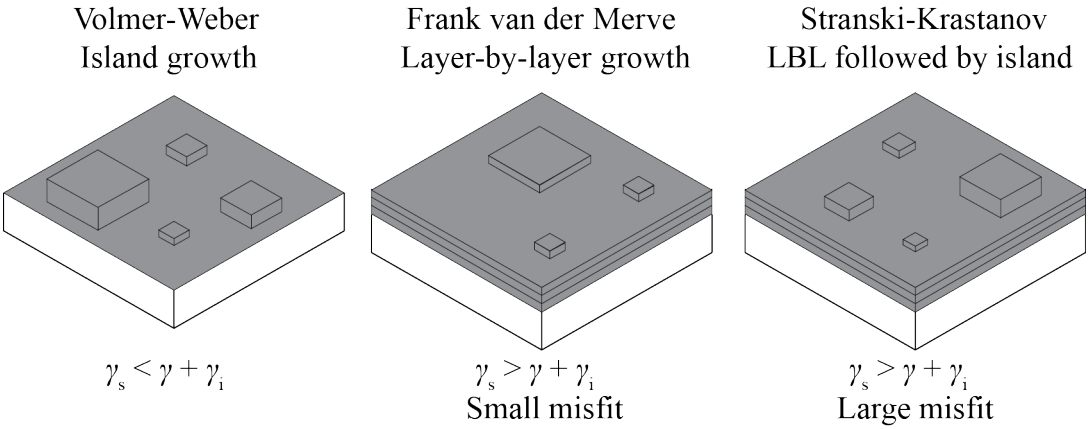

Figure 3.16.: Conditions for epitaxial growth, and the resultant growth types.

Examples of structures that fit well together and are very important in both planar and nanowire semiconductor growth are zinc blende (ZB), wurtzite (WZ), and the diamond structure. Having the same structure is one thing, but having the same lattice parameter is another. In Fig. 2.3 we saw the map of the III-V world highlighting some of the most important solar cell crystals. As can be seen the lattice mismatch can be quite large.

The combination of the wetting and lattice mismatch leads to different growth regimes as identified by Bauer[35], and shown in Fig. 3.16: Volmer-Weber or 3D island growth with incomplete wetting $\gamma_s < \gamma + \gamma_i$. Notice that this is equivalent to the discussion for nucleation. For complete wetting there are two possibilities: Frank-van der Merve or layer by layer growth growth when $\gamma_s > \gamma + \gamma_i$ and the lattice mismatch is zero or small, or Stranski-Krastanov growth or layer-by-layer followed by 3D island growth when $\gamma_s > \gamma + \gamma_i$ and the lattice mismatch is large, since the lattice mismatch can be relaxed for a few layers before islands form.

Planar crystal growth are governed by the above growth modes. Though it is somewhat possible to push the crystal growth away from its preferred growth mode, as we saw with nucleation when 3D became 2D under high supersaturation, Fig. 3.15. There are limits to how far away from the growth rules you can go, but some experimental conditions can help in the direction you desire[36]: High growth temperature favors 3D islands, high deposition rates favors layer-by-layer, crystal orientation affects the growth and densely packed layer planes favor layer-by-layer, and surfactants favors planar growth over island growth.

3.5.4. Multiple atomic growth

Crystal growth often involve more than one growth species. This means that there are two or more species each with their own chemical potential, equilibrium and supersaturation. Because the difference between the phase transformations can be substantial, the growth is mostly performed under a large over-flux of one species. For III-V growth this is done by having a high flux ratio $V/III > 1$, which means that effectively every group V adsorption site is constantly covered, whereas the group III adsorption sites are mostly empty. This means that it is the flux of the group III species that is limiting the growth and the group V flux becomes less important. For growth with more than two growth species the mixing of e.g. group V species requires an experimental investigation of what flux ratios leads to which incorporation ratios. The flux ratio to incorporation ratio will depend on both temperature and absolute fluxes, so it can be challenging to get the exact same result every time. In addition, commercial growers with very large outputs must adjust for changes when e.g. the effusion cells are refilled or the growth chamber has been serviced.

3.6. Growth regimes in planar MBE growth

The above consideration concerning realistic condition doesn't change the basic of crystal growth. The growth is completely decided by the systems thermodynamics and the minimization of free energy. When growing real crystals in MBE the substrate, including crystal direction, and the growth materials decides the possibilities. Within these restrictions the growth conditions can be optimized to grow the desired structures. If, however, the substrate and growth material is poorly chosen, you cannot force the system to grow something it thermodynamically does not want to grow. After choosing materials you will attain good quality planar growth by setting experimental parameters (flux, temperature) that make sure that:

1. The chemical potentials for all growth species must adhere to the relation: $\mu_{vapor} \geq \mu_{adsorbate} \geq \mu_{solid}$.
2. The supersaturation $\triangle\mu = \mu_{adsorbate} - \mu_{solid}$ must be large enough for nucleation to occur, but not so large that undesired nucleation occur frequently.
3. There must be surface diffusion of all growth species. Instantaneous incorporation or desorption will both lead to poor crystal quality.

For nanowire growth it becomes more complex, but it is still a matter of setting up an experimental situation where the growth species can conquer the energy barriers you want conquered, but are unable to conquer the undesired energy barriers.

4. Nanowire Growth

4.1. Introduction

A nanowire is defined as a elongated structure where at least one dimension is below 1μm. Typically nanowires lengths are measure in μms and have a diameter in the range of $50 - 300$nm. They can be made from more or less any material, but most research is conducted on metallic or semiconducting nanowires. Since the focus of this thesis lies on solar cells, semiconducting nanowires that are perfectly crystalline and have bandgaps suitable for single or multi-junction solar cells are the most interesting.

Nanowires can be made both with an epitaxial relation to a substrate or without a substrate. Substrate free growth can produce very large quantities of nanowires. These nanowires are either synthesized in solution[37], in gas-phase[38] or using templates of some form. This thesis, however, is concerned with nanowires grown on a substrate. We are not interested in nanowires that require harvesting and further fabrication, since the expected complications are most likely not commercially viable for solar cells. Therefore the main interest lies in nanowires which stick out of the substrate and preferably vertically from the substrate. Furthermore, the goal is large arrays of wires, so probing of individual nanowires can only be considered a stepping stone on the way to making large arrays consisting of billions of nanowires working in parallel.

Nanowires can in principle be grown in any direction. Energetics of growth, however, seem to favor (111) growth, but other low energy directions such as (100), (110) and (112) have also been grown[39]. There are two basic ways to make crystalline nanowires. A top down approach where a large crystal is treated in a way that produces nanowires, and a bottom up approach where nanowires are assembled from the constituent atoms.

4.2. Top down approach

The most common top down approach is to cover small areas of a planar substrate using either lithography[40], nanoimprint[41] or small particles[42–44]. Afterward a directional etch is used to etch everywhere but the blocked areas, which leaves behind nanowire structures on top of the substrate. Etched silicon wires have been used to experimentally demonstrate anti-reflection performance above the Lambertian limit ($4n^2$)[44]. Etched nanowires have also been part of the active solar structure[45]. If etching of nanowires can be made cost effective, it is possible that this process replaces the current process, where anti-reflection pyramids are etched into the surface of silicon solar cells. The top down approach, however, still doesn't make it possible to combine mismatched materials, which is probably the biggest advantage of utilizing nanowires for photovoltaics.

4.3. Bottom up approach

Whereas the top down approach uses removal of material, the bottom up approach is true nanowire growth. Epitaxial growth of nanowires all share the same basic approach: Take a substrate and either promote growth at nm-scale areas of the substrate, prevent growth on rest of the substrate, or a combination of the two as seen in Fig. 4.1. In a way the nanowire growth is a race between the growth rate of the nanowire and bulk surface. If the bulk grows faster than the nanowires vertical growth speed the nanowire will be buried, or nanowire growth wont be initiated. The vertical growth rate is dependent on the arrival rate of growth material and the energy barrier to nucleation or incorporation of individual atoms. The growth promotion is accomplished by locally increasing the growth species density or decreasing the incorporation energy barriers, and conversely growth prevention is accomplished by locally decreasing the growth species density or increasing the incorporation energy barriers. Since nanowire growth is always performed away from thermodynamic equilibrium, both in terms of phases and shapes, the local differences furthermore have to be sustained over the entire growth time. The bottom up approach is also characterized by the lack of ways to actively shape the structures. Instead, the grower must set up a growth environment where the nanowires growth is the energetically most favorable for the system. This means that the choice of substrate, including material and crystal surface, catalyst, or other growth

promotion/prevention system, and growth material will determine if it is possible to establish growth conditions that enable nanowire growth.

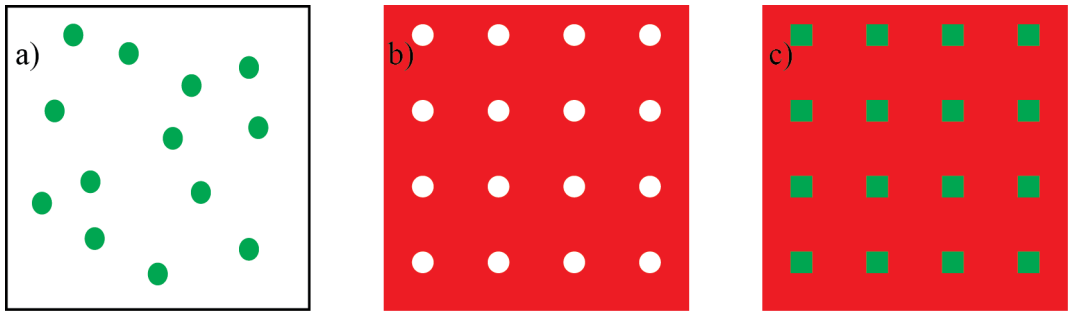

Figure 4.1.: Sections of three growth substrates. Both random and positioned growth is possible. The shape of the conditioned areas of the substrate can vary but are mostly circular. **a.** A random placement of circular areas of high growth probability. **b.** A positioned array of circular areas where most of the substrate has decreased growth probability. **c.** A positioned array of square areas of high growth probability surrounded by a substrate with growth probabilities that have been lowered from a pure substrate.

4.3.1. Selective area epitaxy/growth

Selective area epitaxy (SAE), or selective area growth (SAG), is a crystal growth method that is almost identical to normal planar vapor solid(VS) growth, since the only difference is that the edges of each growth area is much closer than normal planar growth. In SEA most of the substrate is covered by an oxide mask, which prevents or reduces the crystal growth on most of the surface, Fig. 4.1.b. At normal growth temperatures one or more of the growth species cannot adsorb to or will desorp immediately from the oxide surface, thereby making nucleation and growth impossible or very slow. Nanowire growth using SAE is dependent on some crystal facets growing faster than others, since the top facet has to grow much faster than the side facets to obtain nanowires[46]. The key lies in choosing the correct crystal surface direction, which is typically (111)-substrates. When combining the substrate with suitable growth parameters nanowires are produced from each hole in the mask. The process benefits from the fact that only material which are constituent of the nanowires is needed, so in principle very pure nanowires of any crystal can be grown. In addition, high reproducibly as well as the growth of a nanowire from every hole can be achieved. SAE has produced some of the most consisting nanowire arrays,

and is on the forefront of nanowire solar cell research. The process is well suited for making nanowires containing core-shell pn-junctions for solar cells, and the third highest efficiency for a nanowire solar array of 6,63% has been achieved with SAE grown GaAs nanowires[47].

4.3.2. Catalytic nanowire growth

Catalytic growth is the opposite of SEA growth, since it promotes growth at certain sections of the substrate, as seen in Fig. 4.1.a. The technique utilizes small liquid drops or solids of a foreign material called catalysts which is not a constituent of the grown nanowires. The most common catalyst is liquid droplets of metals and primarily gold (Au)[48], which will be focus in this section. The growth process is known as vapor liquid solid (VLS)[49] and proceeds as shown in Fig. 4.2:

1. Catalyst particles are either distributed randomly using in-situ or ex-situ evaporation, colloids or aerosols[50], or placed at designated positions using electron beam lithography[51] or nanoimprint lithography[52].

2. The catalyst is heated inside the chamber until it melts. The catalyst can alloy heavily with the substrate during this stage dependent on the phase equilibrium with the substrate.

3. The growth is initiated, when the growth species are introduced into the chamber. If the right combination of substrate, catalyst and growth species are chosen vertical growth begins as the growth parameters creates a larger growth rate under the catalyst than on the rest of the substrate. This is probably the most important stage of nanowire growth.

4. When the growth is proceeding the adjustment, addition, removal, or exchange of growth species can result in a multitude of different nanowires. The bulk of nanowire growth research has been focused on this area.

The two main growth techniques for catalytic nanowire growth are metal organic chemical vapor deposition (MOCVD) and MBE as described in Sec. 3.2.

In MOCVD the growth species are delivered to the growth substrate as part of molecular complexes called precursors that are carried past the substrate by a carrier gas. Before the growth species can be involved in any growth, the molecules has to be cracked in order to free the growth atoms from the rest of the precursor.

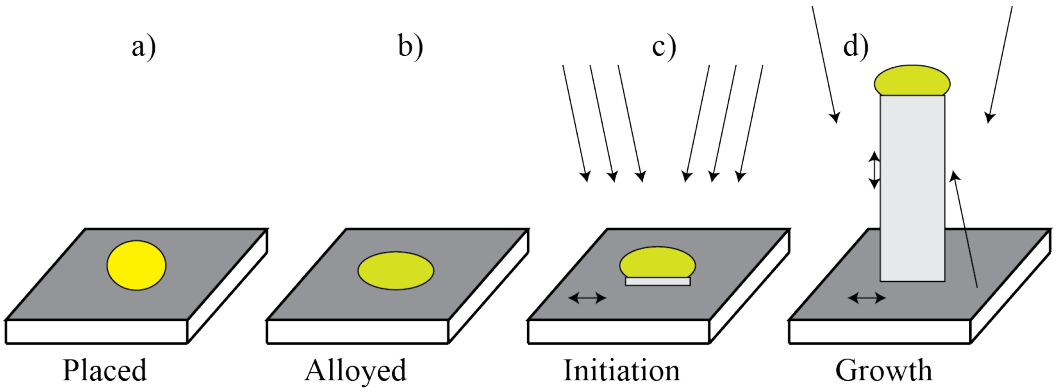

Figure 4.2.: The four stages in VLS nanowire growth. The arrows indicate some of the growth species transport processes as seen in Fig. 4.3 **a.** A catalyst particle is placed on the substrate. **b.** The catalyst melts and possibly alloys with the substrate. **c.** The growth species are introduced to the growth chamber, and the growth is initiated according to the flux, diffusion and chemical potentials in the system. **d.** The growth is continued until the final structure is acchieved.

The cracking has an energy barrier associated with it, see Fig. 3.2, which for some precursors can be catalytically lowered by the Au droplet [53]. This catalytic reaction can promote axial nanowire growth, since a larger percentage of the growth material is delivered very close to the nanowire growth front. In addition, substrate growth can be prevented by covering the surface with the polymer polylysine [54], which moves the growth type from Fig. 4.1.a to c. Once the growth atoms have been liberated from their precursor the physics governing nanowire growth is much the same for MOCVD as MBE growth. Growers and theoretician must, however, be aware that the vapor phase in the two growth systems is different, so the chemical potentials and equilibria can be very different, which means that not all nanowire growth can be easily transferred between the two systems.

In planar growth the growth species movement is a local phenomenon since the growth species land everywhere, and the entire substrate have more or less the exact same growth conditions. In nanowire growth the diffusion of growth species is much more important and complex. In Fig. 4.3 is seen the many phases and transitions in catalyzed nanowire growth. In comparison with planar growth, Fig. 3.4, the system has gone from 3 to 7 phases and from 6 to 16 transitions. Again not all transitions are included, and neither is internal movement within the phases such as diffusion in the adsorbates and liquid. Each arrow, or arrow pair, has a rate as defined by equations of Arrhenius type Eqn. 3.1, and by influencing the rate equations it is

possible to affect the growth. There are three different solid phases, which really are three different locations of the same phase. The promotion of incorporation at the various solid phase positions is what decides the growth. If incorporation at the nanowire top is promoted a long thin nanowire is grown. If incorporation at the sidewalls is promoted the nanowire becomes thicker. If incorporation on the substrate is promoted no nanowire is grown.

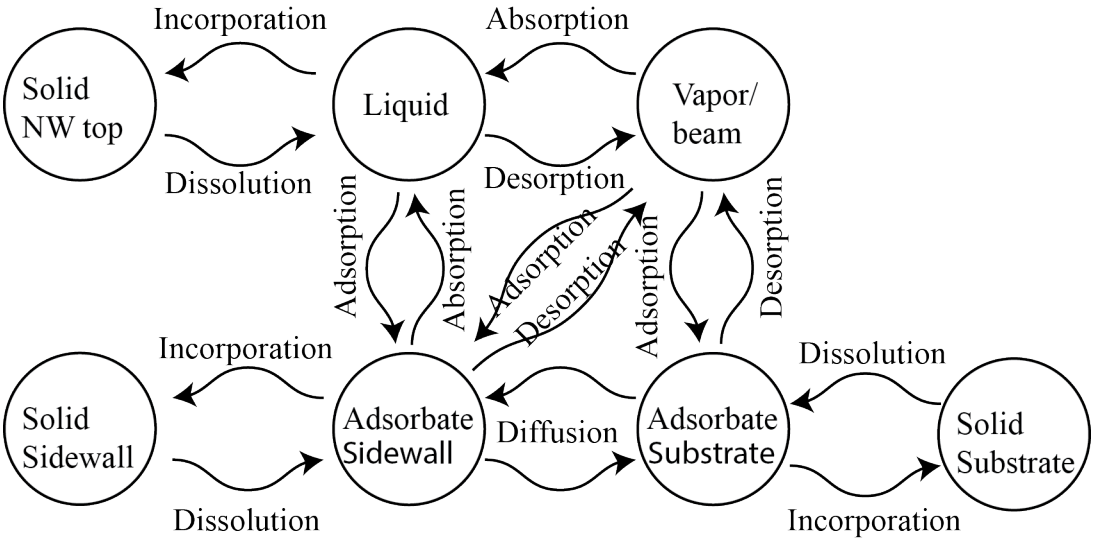

Figure 4.3.: The seven phases and sixteen most important transitions in VLS nanowire growth. Each phase (circle) has a chemical potential, and each transition (arrow) is governed by its own rate equation, Eqn. 3.1.

The phase diagram in Fig. 4.3 is already complicated if you think of it in terms of individual nanowires, but it is further complicated by the fact that the growing nanowires start to affect both their surroundings and neighboring nanowires. If nanowires are grown in close proximity they share substrate collection areas, and growth species may also diffuse between the wires [43]. Nanowires grown in MBE will cast a shadow as the molecular beam hits them at an angle [55]. Unlike planar growth, atoms that desorp from the liquid, sidewall adsorbate and substrate adsorbate has an increased likelihood of being re-caught by the growing nanowires [56,57].

Au catalyzed growth has shown great versatility as a growth method [39,48], and has been used to grow almost every conceivable semiconductor nanowire. Au doesn't wet and therefore readily forms droplets on most surfaces. At the same time almost every material can, to a certain degree, be absorbed in the Au catalyst particle. This makes Au-catalyzed nanowire growth ideally suited to grow nanowires containing

more than one crystal in the axial direction in so-called heterostructures. On the other hand, the Au particles presence on the top of the nanowire, makes it difficult to grow core-shell nanowires, since it is difficult to prevent the axial nanowire growth when the shell is being grown.

4.3.3. Self-assisted nanowire growth

Self-assisted nanowire growth is when the nanowire growth is catalyzed by a liquid droplet which is a constituent of the final nanowire. Self-assisted growth requires that there is a surplus of one or more of the growth species, which forms a liquid droplet, somewhere on the surface of the substrate as seen in Fig. 4.4. These droplets then function, in the same way the droplets in normal catalytic growth function, by being collection centers and increasing the growth rate below them compared to the rest of the substrate. The most investigated growth types has been with group III materials such as In[58] or the more common Ga[59] including [I,II,III]. The droplets can collect at pinholes in native[60], grown or deposited oxide[61] covering the whole substrate. The holes either exist already or their formation is promoted by Ga-catalyzed dissolution of the oxide[61]. Above a certain oxide thickness the catalyst wont be able to reach the substrate and catalyze growth with relation to the substrate. It is also possible that the catalyst can collect in holes that have been etched in the oxide at positions defined by lithography[62,63] or other processes. It is also possible for the droplets to gather on substrates that the catalytic material wets poorly($\gamma_s < \gamma + \gamma_i$), so that droplets form on the surface in the same way Au droplets form in Au-catalyzed growth[64,65].

The self-assisted growth has a number of advantages over foreign catalyzed growth. Incorporation of Au from the catalyst particle has been observed in nanowires[66,67], but whether the incorporation degrades performance[68] or not[69] is still being investigated. From a commercial solar cell standpoint a few missing % in efficiency can be the difference between success and failure, so if possible it is preferable to keep contaminants away from the growth chamber. The second advantage is that the catalyst particle can be removed at the end of growth, by simply shutting off the catalytic growth species while maintaining the other fluxes, since the growth will continue until the catalyst is consumed [I]. After which, the nanowire is perfectly prepared to function as the core in a core-shell nanowire growth. Self-catalyzed growth is still neither as reproducible nor as flexible as SAE and Au-catalyzed growth, but

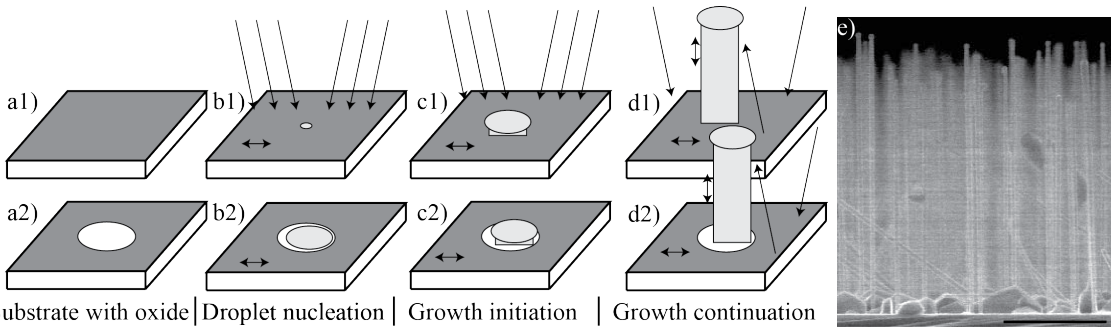

Figure 4.4.: The four stages of self-assisted nanowire growth. Above growth with native oxide, and below growth from defined holes in the oxide. The arrows indicate some of the growth species transport processes as seen in Fig. 4.3 **a1.** A surface covered by a thin oxide layer. **a2.** Holes have been defined and etched into the oxide mask to expose the substrate. **b1.** Droplets form and through pinholes reach the surface. **b2.** Droplets collect in the etched holes. **c.** Nanowire growth is initiated when the other growth species are introduced to the chamber. **d.** Nanowire growth is continued. **e.** Sideview SEM image of self-assisted GaAsP nanowires grown on Si. Scale bar is 1μm

with time could close the gap and at least become as reproducible.

4.3.4. Strain accommodation

No matter which nanowire growth technique is used, one of the major advantages, especially for solar cell technology, is the ability to grow lattice mismatched crystals on top of each other. In Sec. 3.5.3 we saw that in planar growth two crystals can only be grown on top of each other if they fit very well together and wet each other well, so layer-by-layer formation is favored over island formation. If the lattices didn't match the strain at the interface of the crystals could cause dislocations.

When growing nanowires the strain between crystals with different lattice constants can be relaxed due to the small interface. There exist a radius limit below which the strain can be completely relaxed and no dislocations appear at the interface between substrate and nanowire[70–73]. Smaller lattice mismatches will increase this critical radius, and the exact growth method may also move the limit somewhat[46,74]. If the radius is larger than the limit for dislocation free growth, most of the strain is relaxed at the interface through the formation of crystal dislocations and the remaining strain is relaxed within 50nm[75]. Since nanowires are typically several µm in length, most of the nanowires crystal quality is conserved and dislocation

free. It is important where the dislocations are situated, since the crystal quality in some areas of actual devices are more important than others. The SCR in the pn-junction is the section that is most sensitive to crystal defects, since recombination here is likely to reduce the V_{oc} and thereby the solar cells efficiency. Away from junction minority carriers are so few, that especially SRH recombination becomes less likely. In high efficiency planar multi-junction solar cells it is impossible to avoid dislocations completely due to imperfect lattice matching. Great care is taken to keep the pn-junction sections of the crystal free of dislocations. However, some crystal imperfections are accepted in the buffer regions at the interface between two crystals.

4.3.5. Nucleation and single layer formation

Nucleation is even more important for nanowire growth than for planar growth. Due to the small area and limited amount of growth species available at the droplet-nanowire interface, every layer of growth will be nucleated by a single nucleation event. After the stable nucleus is created the rest of the crystal layer form trough successive incorporations at kink sites, which means that the layer will adapt the crystal structure that the nucleus have.[76,77]. The critical nucleus is the nucleus with the lowest free energy cost. Nucleation at the interface between liquid, solid and vapor, called the triple-phase line (TL), is energetically favored over nucleation in the interior of the droplet.[78]. This is key in explaining why (111) nanowires sometimes grow with a WZ structure rather than the bulks ZB structure. If the TL is in contact with the edge of the nanowire top, as seen in Fig. 4.5.a, WZ nucleation is favored, since the sidewall energy of WZ is lower than ZB[78,79]. If the TL is not in contact with the nanowire edge ZB formation is favored[80], which is important because the circular TL will not always lie on the hexagonal nanowire edge, as seen in Fig. 4.5.b. When the growth proceeds with a side facet that is not perpendicular to the top facet, as seen in Fig. 4.5.c, the droplets position and angle in relation to the top facet might alter the shape of the low energy nucleus, and the result can be growth of structural superlattices[79,81]. There is also the possibility that the surface of the nanowire is not flat during growth, as forces at the TL changes the shape of the nanowire in the proximity of the TL, as seen in Fig. 4.5.d . The result is the formation of a truncation consisting of small facets at the edges of the nanowire, which can be very important to nanowire growth[24,82–85], and possibly

help explain how wires kink and change growth direction. With the complex system at the catalyst-nanowire interface, the important thing to keep in mind is that the nucleus with the smallest formation energy will form, and the new crystal layer then forms through kink site incorporation.

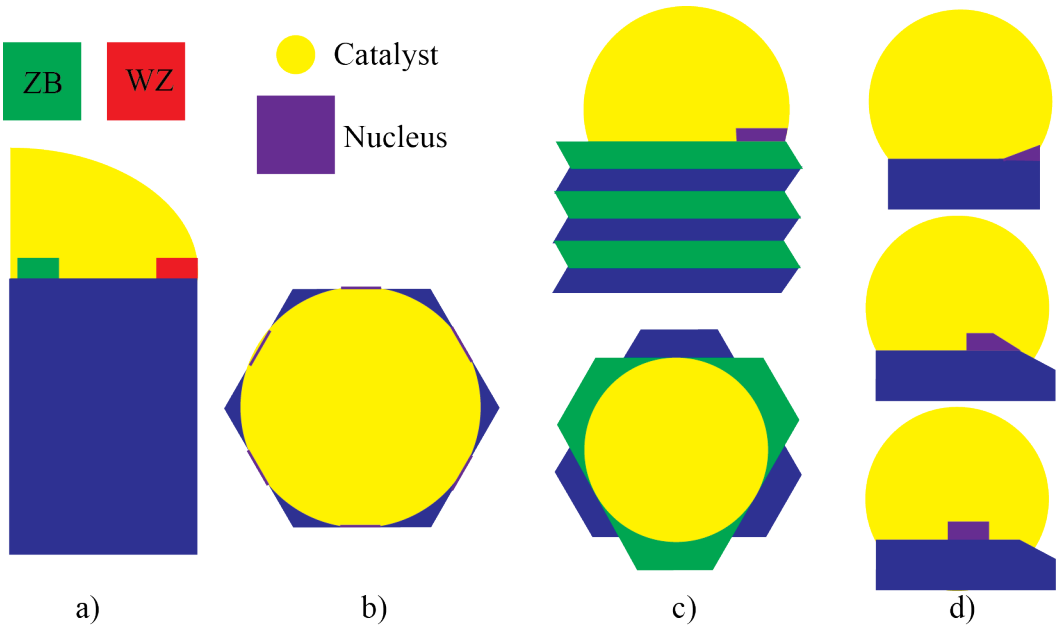

Figure 4.5.: Nanowire nucleation. **a.** Nucleation at the nanowire edge promotes the WZ structure. **b.** The exact position of the liquid droplet in relation to the facets and shapes of the growing nanowire affect nucleation. **c.** Superstructure formed as the TL nucleus is affected by the angle of the droplet at the TL. **d.** The top facet is not necessarily flat, but can be deformed by the forces at the TL.

Once the critical nucleus has formed, the rest of the layers growth is continued by incorporation at kink sites. Since almost no supersaturation is required for kink site incorporation this process is fast compared to nucleation. This means that a lot of growth atoms are removed from the droplet and this leads to a decease of the supersaturation below the critical limit[24]. This means that the nucleation no longer is continuous but clock-like, since the supersaturation has to build up until nucleation can occur again. Outside the droplet the kink site incorporation occurs via the sidewall or top adsorbate phases. This incorporation continues until low energy facets which are in equilibrium with the adsorbate are formed.

Since the interface area between nanowire and substrate is so small the growth of each crystal layer has a high likelihood of being initiated by a single nucleation event. This avoids the anti-phase problem with polar on non-polar growth when

combining Si and III-V crystals[86], through the problems of electrical neutrality across the boundary and cross doping remains. In addition, the individual nanowires can be rotated in relation to each other in order to accommodate the underlying substrates crystal[64]. Planar growth with more than one nucleation event have large accommodation problems when the advancing step edge from different nucleation meet, since there is not enough energy in the systems to rearrange all the atoms in one of the nucleation sections. If the system was much smaller it would require less energy to make this rearrangement, and a similar transition has been observed experimentally, where the buried part of a WZ nanowire changed to ZB[87].

Since catalytic nanowire growth is nucleation limited, prediction of growth is practically reduced to finding the nucleus with the smallest formation energy ΔG^*. This is done by looking at all the places and ways a cluster can form, and then calculating the formation energy for all the possibilities. The formation energy has the two parts from Eqn. 3.12 namely volume creation and surface creation. The volume energy will be negative and have the form $n\Delta\mu$, and the surface energy will be positive and have the form $\left(\sum_j \gamma_j \xi_{j,}\right) + \gamma_i \xi_i - \gamma_s \xi_s$ because new surfaces have to be created while the previous surface disappears and the interface energy has to be accounted for. It is reasonable simple to set up the formation energies equations, but the real challenge is finding the relevant energies and supersaturations. In addition, the systems as described in Fig. 4.3 is highly dynamic, so in-situ observations of the real growth is critical in establishing which surface facets are in play. In addition, modeling must really be dynamical, as the system is constantly evolving in an attempt to minimize the free energy[24].

4.3.6. Axial heterostructures

The axial heterostructures can be put into three categories:

1. Material: nanowires made out of different materials
2. Structural: WZ/ZB or twinned structure changes, lattice superstructures and kinked wires.
3. Electrical: Changes in the doping profile in the axial direction.

The three heterostructures types can also be combined. The structural heterostructures are governed by the minimization of free energy during growth. The material heterostructures are accomplished by adding, removing or adjusting the flux of

growth material. Examples of material hetero structures are seen in Fig. 4.6. When changing growth material it is desirable to be able to change as abruptly as possible, since non-abrupt junctions can usually be obtained by a gradual change of growth material. The liquid catalyst acts a reservoir for the growth species, where the size of the droplet and the solubility of the various growth species determine how much growth material is inside the catalyst at any point during growth. Phase diagrams are helpful in finding the equilibria for the different species, but the phase diagrams might not tell the full story, since the equilibrium in the liquid has to be balanced by the equilibrium with the other phases in the system. However, some success in making more abrupt interfaces has been achieved by adding materials that reduce the solubility of certain growth species in catalytic particle[88]. The reservoir effect means it can be hard to reach the desired material heterostructures when only one junction is abrupt since one growth material leaves the catalyst quickly whereas the other(s) linger Fig. 4.6.d. There can be other complexities such as different incorporation across the top facet for different species[89].

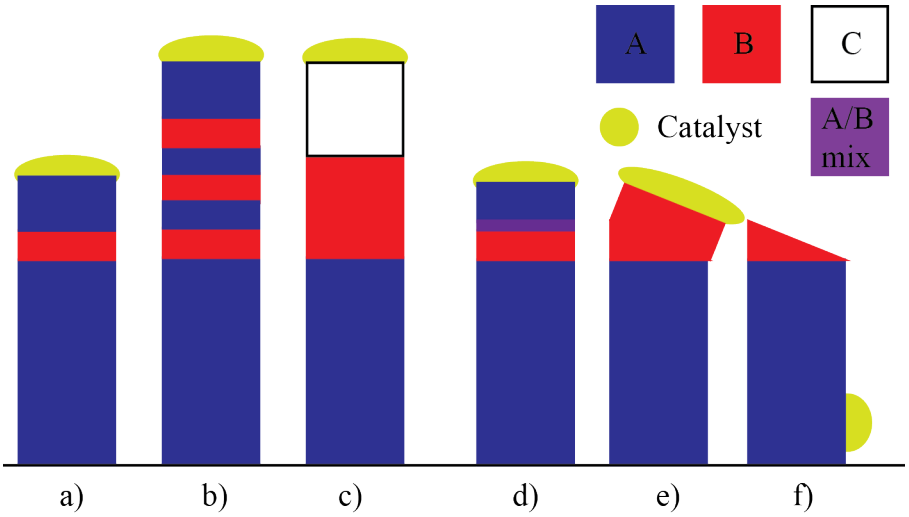

Figure 4.6.: a. A nanowire made out of material A with a single inclusion of material B with abrupt interfaces. **b.** Several inclusions of material B with abrupt interfaces. **c.** Change from material A to B to C with abrupt interfaces. **d.** Abrupt interface from A to B, but a non-abrupt interface from B to A. **e.** Island formation when going from A to B causes kinked growth. **f.** High catalyst interface energy to material B causes the catalyst to completely move of top facet.

In many ways the axial material change heterostructures behaves much the same as nanowire on bulk substrate, since the small interface area allows the relaxation of

lattice mismatch. The result is that if island formation is favored the nanowire will often kink when switching from B->A as seen in Fig. 4.6.e. If the catalyst interface energy with material A is much smaller than with B the catalyst might move of the top completely, as seen in Fig. 4.6.f.

When growing axially there is a possibility of simultaneous growth on the sidewalls. It is important to prevent radial growth when making material changes in the axial direction. Dependent on the axial growth it may be possible to select growth parameters that decreases the supersaturation between adsorbate and the sidewall, which can reduce or avoid nucleation and consequently radial growth. If those growth conditions are impossible you may be able to employ surfactants that prevent growth or even in-situ etching[90]. The opposite is also true. You also have to avoid sidewall dissolution of sections that have already been grown. This has been observed for indium antimony (InSb) nanowires grown on top of InAs nanowires[91]. The original InAs nanowires sidewall started to dissolve when the As flux was turned off, since there suddenly were an undersaturation between sidewall and adsorbate.

Doping can be added to the growth species in order to change the electronic structure of the nanowires, e.g. a pn-junction can be made. In principle it should be possible to make abrupt axial doping junctions, since there is so little material in the droplets and on the surface. Clean axial doping heterostructures has, however, been harder to grow than hoped for. Doping incorporation on the sidewall[92,93] is a major challenge, and it is possibly that top facet truncation will lead to different doping inclusion across the top facet[94]. These two problems both yield a radial doping structure on top of the axial doping structure. It is difficult to measure the electronic properties of nanowires, and thereby their doping, because surface effects can override the bulk properties when e.g. measuring the conductance of the nanowires. In addition, the doping inclusion is so small that only highly specialized characterization tools such as atom probe tomography can be used to measure the doping values[95,96]. The research topic is still quite new, and more studies can be expected in the future, which perhaps can lead to better understanding of how dopants are incorporated and lead to better control, and hopefully high quality pn-junctions. For multi-junction solar cell in axial heterostructures, sharp doping interfaces are also needed to make axial tunnel junctions.

4.3.7. Core-shell heterostructures

After nanowire growth it can be beneficial to surround it with a shell of a different materials or with a different doping profile. Most good core-shell heterostructures are based on nanowires without a catalytic particle on top. This means that the growth is basically a planar growth, except that the "substrate" is now a nanowire with multiple crystal facets. Since there is no longer a catalyst, core-shell growth avoids the reservoir effect and atomically abrupt junction are easier to accomplish both for material and doping junctions as seen in Fig. 4.7a-d. The interface area in core-shell heterostructures is much larger than for axial heterostructures. This makes lattice matching between core and shell more important than for axial heterostructures, since dislocations at the interface will disrupt the whole nanowire crystal, and less strain can be accommodated. The lattice mismatch that can be accommodated falls between that of the axial heterostructures and planar bulk heterostructures[97,98]. Since the strain relaxation is area dependent thinner wires can accommodate a larger lattice mismatch than thicker ones, and below a certain radius no dislocations will be seen[99]. If growing in the Stranski-Krastanov regime Fig. 3.16.c more crystal layers can be grown before islands starts to form. This is beneficial if only very thin shells are needed, which e.g. is the case for surface passivisation.

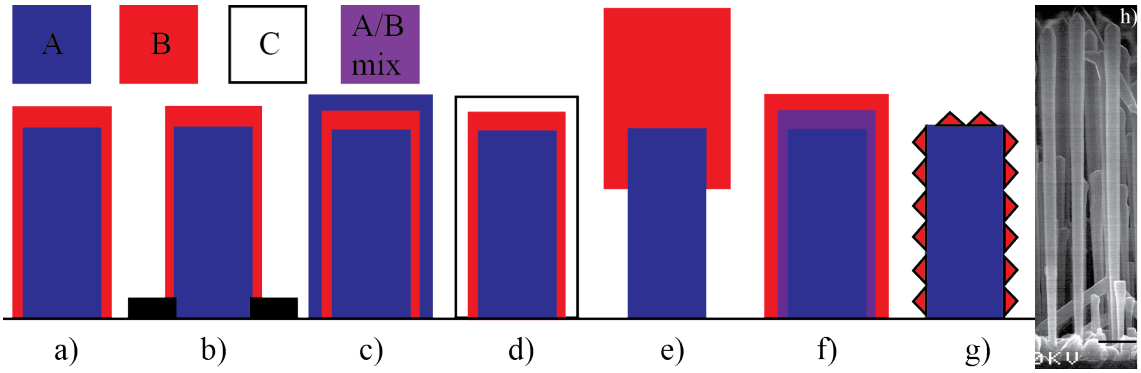

Figure 4.7.: Core-shell heterostructures. **a.** Abrupt change from A->B. **b.** A change from A->B, where the bottom of material A is buried in an oxide mask. **c.** Abrupt changes A->B->A. Several changes can produce superstructures **d.** Abrupt changes A->B->C **e.** Core-shell growth can be anisotropic, if the growth species flux is directional, nanowires grow close to each other, or different growth speeds on different facets. **f.** Unabrupt change. **g.** Island growth instead of layer-by-layer. Can be utilized to grow quantum dots. **h.** Core-shell GaAsP nanowires with p-i-n doping structure and InGaP shell. Scale bar is 1μm

5. Nanowire Solar Cells

5.1. Introduction

This chapter will focus on III-V nanowire solar cells, which has been recently reviewed[100], and slightly older reviews are also available[101,102]. The section will, however, neither discuss hybrid solar cells where e.g. a polymer is the p(n) part of the solar pn-junction[103–106], solar cells where the nanowire is only part of the pn-junction[107–110], nor solar cells where a Schottky diode is used to separate the carriers[111].

5.2. Our publications

5.2.1. GaAs single nanowire solar cell, ref[II]

GaAs is one of the best semiconductor materials for single junction solar cells, due to a 1.4eV bandgap it has a SQ-limit of 33,5%, and other good material qualities should enable it to approach this limit[112]. Prior to our article, self-catalyzed nanowire growth of GaAs using Ga droplets had been shown[60–62], and several individually contacted nanowires had been made into single nanowire solar cells, but they were always lying flat on a substrate[113–116]. The research was, therefore, an investigation into how well a single vertical nanowire solar cell would perform. Specifically, to investigate the prediction that nanowires can absorb light from an area, which is greater than their top surface[117–120].

GaAs nanowires with a core-shell p-i-n junction were grown from predefined 100nm diameter wide oxide holes on p-doped silicon(111). The successfully grown single vertical nanowires were made into solar cells. They were enclosed in SU-8 resist and contacted individually with a transparent top contact made out of indium tin

oxide (ITO), II.Fig.1.a-c. The highest, apparent efficiency was 40% when using the top area of the nanowire to calculate the efficiency despite a poor fill factor(0.52) and low open circuit voltage(0.43V), II.Fig.1.d. The 40% efficiency is somewhat misleading, as the result can't be scaled-up to production of a real solar cell, since the area between the nanowires would then have to be included in the efficiency calculation. What can be transferred to real solar cells is that the nanowire absorbed light from a much larger area than its top surface, which yielded an average built-in concentration of 8 and a top concentration of 12 at the bandgap edge, II.Fig.3.a. Our Swiss colleagues used a finite-difference time-domain (FDTD) method [121,122] to simulate the absorption cross section, or concentration, for a SU-8 enclosed, standing, GaAs nanowire with different diameters, II.Fig.2.b, which correlated well with the measured absorption spectrum II.Fig.3.a. The enhancement at certain wavelength and diameters are due to Mie resonances, which have also been observed for single nanowire solar cells lying on a substrate [123,124].

5.2.2. GaAsP single nanowire solar cell, ref[I,III]

[I] and [III] can be considered together, since they both are concerned with Ga-catalyzed GaAsP nanowires grown on native oxide covered silicon(111) substrates.

It is going to be very difficult for single junction solar cells based on nanowires to succeed commercially, especially with Alta Devices 28% 1-sun record efficiency planar solar cell [125] as competitor in the market gap Sec. 1.3. It is more likely that high efficiency multi-junction nanowire solar cells grown on a silicon substrate will break trough. The simplest multi junction cell is a dual junction cell, and design-wise it is possible to include a solar pn-junction in the silicon growth substrate. The perfect bandgap combination for a dual junction cell, when constrained to a silicon bottom cell, is a 1.7eV bandgap top cell. A solar cell consisting of a 1.7eV bandgap nanowire top cell and a silicon bottom cell has been predicted to yield a 33,8% 1-sun and 42,3% 500-sun efficiency [126]. There are several III-V semiconductors with a 1.7eV bandgap, but to reduce the number of dislocations in the interface, a small lattice mismatch with silicon is preferable. Therefore, the best option is probably the direct bandgap $GaAs_{0.8}P_{0.2}$. We further chose to grow nanowires with a core-shell pn-junction, which decouples absorption (along axis) and carrier separation (radial) [127]. This choice meant that we needed both the correct composition of the core nanowire and lattice matching between core and shell, as described in Sec. 4.3.7.

The radial pn-junction also allows the growth of a surface passivating window layer, which we expected would be key in producing high efficiency nanowire solar cells.

Ref[III] highlights the iterative process needed to include phosphorous (P) into the Ga-catalyzed growth developed for GaAs nanowires[57]. The V/III flux ratio affected the shape of the grown nanowires, and straight sides where obtained with V/III = 50. Increasing the absolute flux increased the nanowire density, but also increased the surface growth between the nanowires, so there was a tradeoff between high density of nanowires and reducing unwanted surface growth. The most important finding, however, was the difference between incorporation of P in catalyzed nanowire growth compared to planar MBE growth as shown in III.Fig.5. The percentage of P incorporation was generally higher in nanowires than for planar growth at identical flux percentage. More interestingly, the percentage of P in the nanowire was found to be a concave function of the percentage of P in the flux, while for planar MBE growth it was a convex function. So when the percentage in the flux was increased the incorporation of P slowed down in nanowire growth, where it sped up in planar growth. This result stems from the very different incorporation pathways for the growth species in planar MBE growth compared to nanowire growth, as shown in III.Fig.6. The result highlights that fundamental observations of this kind is vital, if complete control over ternary compound nanowire growth is the be achieved.

Ref[I] is primarily concerned with fabricating and improving single nanowire solar cells (SNWSC). Several characterization techniques were utilized to investigate the core nanowire composition. Scanning electron microscopy (SEM), small angle X-ray diffraction (XRD) and room temperature photo-luminescence (PL) were used to investigate the properties of large ensembles of wires, while individual nanowires were investigated using transmission electron microscopy (TEM), including diffraction, and energy-dispersive X-ray spectroscopy (EDX). The many characterization techniques confirmed that we were able to produce almost perfectly crystalline zinc-blende $GaAs_{0.8}P_{0.2}$ nanowires, which had almost the same composition along the axial direction. In addition, we showed that the composition could be varied from X=0.15 to X=0.70 in a single wire, and we speculate that the complete 1.42–2.26 eV GaAsP bandgap spectrum is available when using Ga-catalyzed growth.

The $GaAs_{0.8}P_{0.2}$ nanowire growth recipe was then used to grow the core of core-shell nanowires. Following the core nanowire growth the Ga droplet was consumed

by letting the group-V flux remain after the Ga shutter was closed. Afterward, a shell was grown around the core by VS growth on the sidewalls and top facets. The AS/P flux ratio during the shell growth was iteratively changed, as a result of an investigation of the composition between growths using primarily XRD and PL. We were able to produce the first lattice matched core-shell $GaAs_{0.8}P_{0.2}$ nanowires, since previously grown GaAsP core-shell nanowires were not lattice matched[128,129]. Having found good parameters for lattice matched core-shell growth of good crystal quality, we included doping with beryllium to the core and silicon to part of the shell growth to produce a radial p-i-n junction in the nanowires. A number of the grown p-i-n junction nanowires were removed from the substrate, placed on an insulating wafer, and selectively contacted at each end to produce SNWSCs. 28 SNWSC were investigated under 1.5 AMG illumination, and the top efficiency was 6.8%, and the average efficiency was 2.9%. The 6.8% efficiency was better than previously reported for SNWSCs, but especially the open circuit voltage (0.76V) seemed poor compared to the SQ limit for a 1.7eV bandgap solar cell (1.4V). SNWSCs are only a stepping stone on the way to nanowire solar cell arrays, so we didn't want to begin a time-consuming optimization process on the p-i-n doping structure. Instead, we chose to attempt to passivate the surface, since no proper surface passivisation had been done for nanowire solar cells[130]. Surface passivisation should have a huge impact on the V_{oc}, and even an unoptimized surface passivisation was expected to work reasonable well[126,131]. Surface passivisation using a window layer was applied by growing an additional shell around the nanowire consisting of a highly doped, wide bandgap semiconductor. Again we wanted lattice matching, so we chose InGaP. We can't be sure, if we succeed in lattice matching, since we did not have access to characterization tools that could properly investigate the thin InGaP layer. The small shoulder in the XRD of sample R30, I.Fig.2.b., could indicate that we did not achieve perfect lattice matching, but the crystal quality didn't suffer, so we suspect, we were close. 43 surface passivated SNWSCs were investigated, and this time the top efficiency was 10.2%, and the average efficiency was 5.0%. We saw improvement in all important solar cell parameters, and especially the improvement of the V_{oc} by ~0.15V was encouraging. The 10.2% efficiency is still the record for SNWSCs lying on a substrate.

It is hard to compare SNWSC's efficiency with a "real" solar cell, whether they are standing up as in [II] or lying down as in [I]. If we positioned the nanowires from [II] in an array, the solar cell would probably have an efficiency ~4%, which

would put it in the efficiency neighborhood of several published nanowire solar cell arrays[47,132–134], but far behind the very good recent InP-based arrays[135,136], which again are very far from the single-junction record of 28,8%[1,125,137]. Speculating on the efficiency of an array made from the best 10.2% efficient GaAsP SNWSC's is even harder. It has been theorized that erecting a lying SNWSC, and putting it into an array would yield an solar cell array with double the efficiency[122], primarily owing to a lack of absorption in a nanowire that is lying down. Since the current is not the biggest problem for our best SNWSC, it is more likely that a solar cell array would have an efficiency around ~15%. This would require a perfect array consisting of perfect nanowires, and would still be far from the single junction record. The dual junction record of 31.1%[138] seems closer at hand, since a ~10-15% silicon solar cell below a perfect array of GaAsP nanowire solar cells would quickly approach 30% efficiency.

5.3. Single nanowire solar cells

Single nanowire solar cells (SNWSC) are solar cells where the solar cell consist of a single nanowire. It is easier to make SNWSC, since they only require individual nanowires, than nanowire solar cell arrays (NWSCA), which require a higher degree of control over the growth process. SNWSC can be used as a steppingstone on the way to a NWSCA, and fundamental aspects of nanowire solar cells can be probed with SNWSC. Some insights into nanowire solar cell behavior can possibly only be obtained by fabricating and characterizing SNWSCs.

5.3.1. Doping structure

First thing to consider is the design of the pn-junction. There are two ways of designing the doping structure, and both have advantages and disadvantages. One way is to have an axial pn-junction, as seen in Fig. 5.1.a. The other is to have a radial pn-junction, or core-shell, Fig. 5.1.b. When more than one pn-junction is needed, one or more of the junctions can be in the nanowire or the substrate, but the largest bandgap should be grown last, unless a reverse growth is performed Fig. 5.1.c. It is also possible to only have part of the pn-junction in the nanowires, e.g. only have the n-doped section in the nanowire while the substrate contains the p-doped section Fig. 5.1.d.

5.3.1.1. Axial pn-junction

Nanowire solar cells with an axial pn-junction, in a similar way to planar solar cells, have the same light absorption direction(down) as the carrier extraction direction(up/down). The main benefits for axial pn-junctions are:

1. The small pn-junction area takes full advantage of the built-in concentration, since the light that would be absorbed across the entire plane is now absorbed in the nanowire cross section. This requires that all the photons are absorbed in the SCR section of the nanowire, where the generated carrier can be separated.

2. The axial design should enable the design of multi junction cells within a single nanowire. Growing another semiconductor nanowire as an extension of the already grown nanowire is equivalently to growing from the substrate. The small interface between the different semiconductor materials should relax the strain, due to lattice mismatch, as discussed in Sec. 4.3.6, and the incorporation of several materials with complimentary bandgaps in the axial direction of a single nanowire.

The primary problems with the axial design are:

1. It can be difficult to grow junctions with the desired doping control, since axial growth using a catalyst can cause a reservoir effect for both main materials and dopants. SEA growth avoids this problem.

2. When growing the axial doping structure, detrimental growth on the sidewalls and unwanted doping of the sidewalls can be hard to avoid. In-situ or post growth etching may relieve this problem.[135,136]

3. Wrapping a heavily p- or n-doped, wide bandgap material around an axial pn-junction nanowire will introduce one or more additional pn-junctions along the nanowire sidewall. If surface passivisation proves necessary for nanowire solar cells, then this will be a serious obstacle for an axial junction design.

Only a few articles of SNWSC based on axial design have been published[115,139], which could be a coincidence, or because the research groups favoring this design type have leapfrogged directly into nanowire solar cell arrays.

5.3.1.2. Radial pn-junction

Nanowire solar cells with radial pn-junctions have, unlike the axial designs, the benefit of separating the photon absorption path (down) from the carrier extraction path (in/out)[127]. Other advantages of core-shell pn-junctions are:

1. The core is grown axially and only has one doping type, so problems with sidewall incorporation of doping is removed.
2. The growth of the shells proceeds via VS growth, so the radial pn-junction can be designed with very good control of the doping profile, since there is very little reservoir effect.
3. The complete wrapping of the doping structure around the length of the nanowire means that it is easy to incorporate surface passivisation, since there is no danger of disrupting the solar structure [I][47].

The radial pn-junction design is not without problems, and the most important are:

1. It is difficult to grow more than one pn-junction inside the nanowire, since the core-shell VS growth reduces the lattice mismatch flexibility. The material combinations are reduced towards the planar growth material combinations.
2. The area of the pn-junction, which runs the entire length of the nanowire, is much larger than for axial pn-junctions, so the built-in concentration will be less than for axial designs.

There have been some articles describing SNWSC with a core-shell pn-junction design[114,116,140] including our own [I,II].

5.4. Nanowire solar cell arrays

NWSCAs are real solar cells. These are the types of nanowire based solar cells that at some point, hopefully, will be used to supply power to real world applications. Simultaneously, their efficiency can be directly compared to planar solar cells. Until recently the efficiency has been lower than 5%[132,133,141], but this year several groups have reported >5% efficiency[47,134,136] and even as high as 13.8%[135]. In all cases, besides good control over doping, some type of surface passivisation has been employed, either by using InP[135,136], which is known for a low surface recombination velocity[142], or by applying a surface-passivating window layer[47,134].

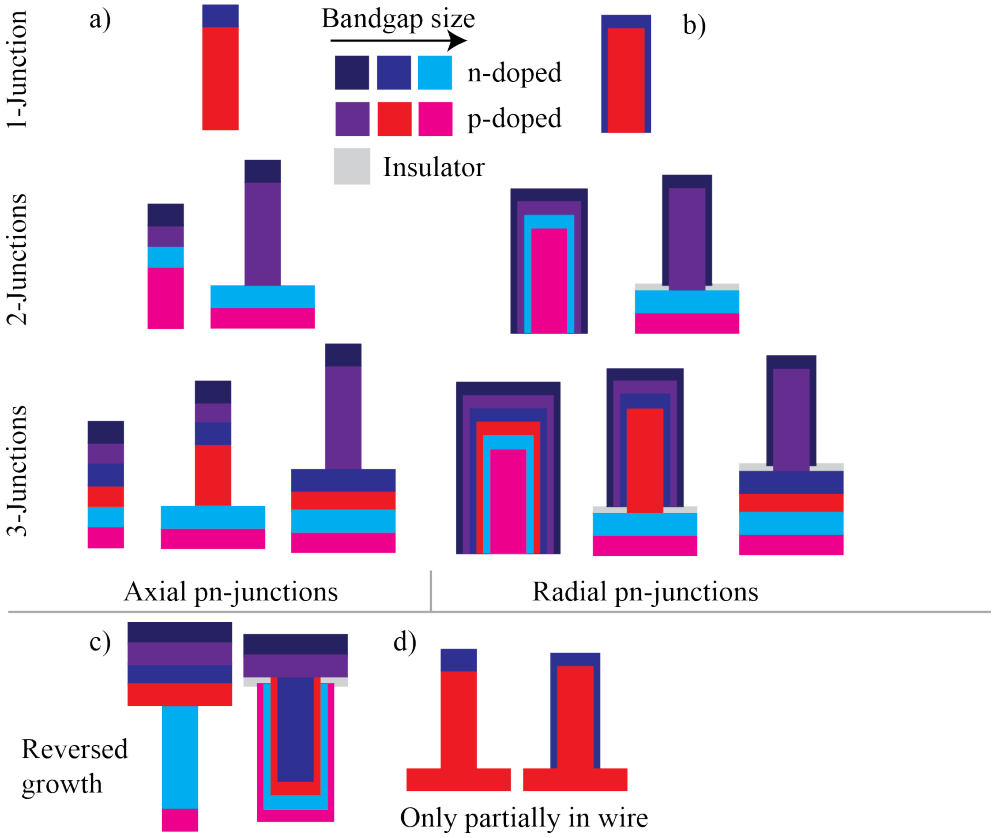

Figure 5.1.: Doping design of single nanowire solar cells. **a.** Axially designed pn-junction(s). **b.** Radially designed pn-junction(s). For radial multijunction cells it's important to insulate the various junctions from each other. **c.** The growth can be reversed so that the smallest bandgap is grown last, but then the solar cell has to be reversed when installed. **d.** Only part of the pn-junction has to be in the nanowire.

5.4.1. Contacting schemes

Contacting the nanowire solar cell array is an added complexity in comparison to planar solar cells. Since it is uncertain if the nanowires will be electrically connected at their base, the scheme probably will involve a top contact to connect the nanowires and conduct the generated current away. The transparency and conductance of the top contact is mostly dependent on the chosen material, and at the moment the only materials that have the right combination of transparency and conductance are transparent conducting oxides (TCO). The most used TCO is indium tin oxide (ITO), since it has the best combination of transparency and conductance. Its wide use has, however, caused indium prices to rise significantly, and a lot of development

is going into other TCOs, primarily aluminum zinc oxide and gallium zinc oxide. It is possible that more exotic materials such as few layer graphene, polarons, electrides or conducting polymers could be used in the future. Once the contact material is chosen there are several ways to design the contacting scheme. In Fig. 5.2 is shown three suggested contacting schemes. The most important aspect is to contact only the top/outer most working section of every nanowires, e.g. the n-doped shell in a GaAs core-shell nanowire [II]. If the top contact is connected to any other part of the solar cells, the R_{sh} will decrease and could completely bypass the solar diode. The simplest and most used technique is to fill the entire space between the nanowires with a transparent insulator, Fig. 5.2.a. The filler provides insulation between top contact and substrate, and it also supports the top contact and increases the solar cell's stability [II][47,132–134,136]. The major drawback of this technique is that the plane surfaces yields an abrupt change in index of refraction, which significantly reduces the nanowire solar cells inherent light trapping ability. In addition, the technique will most likely require that the insulator matches the thermal expansion of the substrate horizontally and the nanowires vertically. It has been suggested that nanoparticles can be mixed with the insulator to increase the light refraction into the nanowires[143], which can increase the distance between nanowires while still absorbing all the light. A contacting technique that retain the light trapping ability of the nanowire array is seen in Fig. 5.2.b. The insulator is applied in a thin layer to cover the nanowires and substrate, at the top of the nanowire the insulator is removed, and the topcontact is then applied. The most likely problem with this technique is the small contact interface between the nanowires and the top contact, since the contact resistance is contact area dependent, this can cause a high series resistance. However, the highest efficiency to date has been achieved using this technique[135]. A third possibility is shown in Fig. 5.2.c. This scheme is only possible for core-shell nanowire solar cell arrays, since the entire shell in principle should be available for contact. The techniques reduces the problem with small contact area between nanowires and top contact. In addition, the oxide pattern used to grow the nanowires can be reused as the insulator, which would remove a costly processing step.

In excess of material choice and contacting scheme a few other considerations are necessary. The contact resistance between ITO and nanowire will be important if nanowire solar cells are going to be successful, particular for high concentration photo voltaics. Increasing the contact area is one approach, but even with a set

contact area there may be improvements to find. Mariani et. al.[47] attempted to improve this aspect by inserting a thin titanium layer between ITO and the nanowires, and the conduction was improved without sacrificing too much transmittance. Experiments along these lines will be needed in order to reduce the series resistance to manageable values. To reduce the sheet resistance of the top contact, an additional metal finger pattern may be needed on top of the top contact. In the Fig. 5.2.b,c contact schemes there may be room for a finger pattern to lie between the nanowires. If so, it is possible that the fingers wont block any light, since the entire photonic field has been guided into the nanowires at the substrate surface. This would be a major advantage for nanowire solar cells, and could also lead to nanowires being used to guide the light into planar solar cell.

The bottom contact should give fewer problems, and the contacting schemes used in normal planar devices can be adapted.

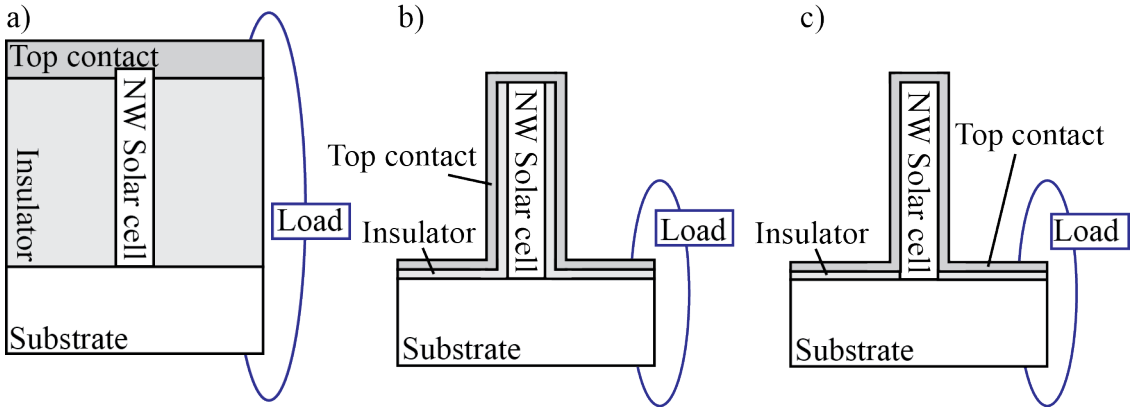

Figure 5.2.: Contacting schemes for nanowire solar cell arrays. The top contact must contact all nanowires, and be electrically insulated from the substrate to avoid shorts. External connection to the load mus also be established. Metal contact grid not shown. **a.** A transparent insulator completely fills the gap between the nanowires. The top contact rests on the insulator. **b.** The insulator only covers the nanowires, and a gap in the insulator allows the topcontact to connect to the nanowires. **c.** The insulator only covers the substrate. The top contact is in contact with the entire nanowire surface.

5.5. Conclusions

Our research has not yet reached the level demonstrating nanowire solar cells that can compete with planar solar cells, since a working solar cell array has not yet

been produced. We have, however, shown fundamental photonic aspects of a single nanowire [II], and demonstrated that the semiconductor with the ideal complimentary bandgap (1.7eV) to silicons, for use in a dual junction nanowire-planar solar cell, can be grown. In addition, we have shown that the GaAsP nanowires work well as solar cells, and been among the first to demonstrate surface passivisation using a window layer on nanowire solar cells.

It is an interesting time for nanowire growth research. The experimental side of the research is getting more and more sophisticated. The reliability and reproducibility is so good, for some methods and materials, that ~100% of predefined catalysts or oxide holes will produce a nanowire with the desired dimension and doping structure. At the same time the theoretical work is catching up to the experimental. In the future, the theoretical predictions, to a higher degree, can be used to predict good growth parameters. Nanowire growth will become more two-sided, as opposed to the current one-sided affair with the experiments leading the way. To improve the theoretical predictions, however, it will be vitally important to have more basic observations of system behavior during the growth, but current in-situ observation systems are rare and only work at certain growth conditions.

In the solar cell area of nanowire growth the research is closing in on commercial application. We only need to improve the current devices by around a factor two, which was the improvement produced in the previous year. In fact, we only need to combine the already demonstrated techniques into a single bundle, and improve the doping structure slightly to begin competing seriously with planar devices.

5.6. Outlook for nanowire solar cells

Nanowire solar cell development can, more or less, be put into three phases: Can we grow it? Can we mature it? Can we make it profitable?

5.6.1. Phase 1. Can we grow it?

This is the phase where most nanowire research, and also most of our research, has been conducted. In this phase researchers are asking and trying to answer questions like: Can we grow a single vertical GaAs nanowire, make a pn-junction, contact it, and what will we see? Can we grow $GaAs_{0.8}P_{0.2}$ nanowires on silicon, can we

lattice match the p-doped core and n-doped shell, and how well will the SNWSC perform? A bit more thought has gone into the selection of $GaAs_{0.8}P_{0.2}$, since it has the perfect complimentary bandgap to silicon for a double junction, so it might be in phase 2. The real maturity for $GaAs_{0.8}P_{0.2}$ nanowire solar cells, however, is when the nanowires are standing in ordered arrays, and the profitability is when the growth is performed on working silicon solar cells.

5.6.2. Phase 2. Can we mature it?

The part of our research that was definitely in phase 2, was the surface passivisation in [I]. For nanowire solar cells some sort of surface passivisation is necessary, whether built-in due to material properties[135,136], or a window layer [I][47,134]. Non-passivated nanowire solar cells will incur losses stemming from large recombination rates due to the small physical separation between the many surface traps and the pn-junction and to the conduction pathways. For confirmation of this one need look no further than the efficiency increases that surface passivisation has demonstrated. In [I] our best SNWSC improved by 50% and the average improvement was 72%. The Huffaker groups 2.54%[132]-> 6.63%[47] is an improvement of 161%, and the Fukui groups 3.37%[133]-> 6.35%[134] is an improvement of 88%. The Huffaker and Fukui groups improved on other fronts between their respective articles, but the primary difference was the added surface passivisation.

The correct selection of materials is also important. In phase 1, it is good enough to turn any nanowire into a solar cell, but for commercial application the grown nanowires must have bandgaps suited for single junction solar cells, such as Si, InP or GaAs, or compliment each other in dual junctions, such as Si-GaAsP or InP(1.34ev)-InGaP(1.9eV)[16], or even for triple junction solar cells. In addition, selecting materials with other inherent material properties such as InPs low surface recombination will be needed.

Nanowire growth has matured to the point that most nanowires that can be grown randomly, also can be grown in arrays at designated positions. More experiments and theory is needed to find the optimal placing of the nanowires in the array[143]. Current arrays are perfectly ordered, but the optimal array is probably unordered both in terms of position and height[144,145].

For MJ solar cells the development of tunnel junctions is also necessary, since resis-

tance in the tunnel junctions between the pn-junctions will be added to the solar cells series resistance and decrease the FF. Tunnel junctions can be inserted in both substrate[146,147] between substrate and nanowire[148,149] and inside the nanowire[139]. Tunnel junctions should be easier to design than the solar pn-junction, but continued development is still needed.

In the discussion of nanowire solar cells one of the most interesting papers has been "Photonic design principles for ultrahigh-efficiency photovoltaics" by Albert Polman & Harry A. Atwater[150]. They highlight the different causes for losses in solar cells, and particular the losses included in the calculation of the SQ-limit. Perhaps some of the losses can be avoided by having nanostructures as part of the solar cell. Particular they looked at possible improvement in open circuit voltage given by:

$$qV_{oc} = E_g \left(1 - \frac{T}{T_{sun}}\right) - k_B T \left[\ln\left(\frac{\Omega_{emit}}{\Omega_{sun}}\right) + \ln\left(\frac{4n_{solar}^2}{I}\right) - \ln\left(QE\right)\right] \qquad (5.1)$$

where T is the solar cell temperate, T_{sun} is the temperature of the sun, Ω_{emit} is the emission angle, which for planar cells are 4π, Ω_{sun} is the angle of the incoming sunlight, which stems from the size of the sun in the sky and unconcentrated is 6×10^{-5}steradians, n_{solar} is the index of refraction of the solar cell material, I is the light concentration factor and QE is the quantum efficiency. The first parentheses is unavoidable thermodynamic loses and reduces the V_{oc} by ~7%[15]. The three loss processes in square brackets, which accounts for a 0.4-0.5V loss in V_{oc}, can be reduced by employing techniques that:

1. Decrease Ω_{emit}, e.g. by making emission directional. By designing the nanowire according to the emitted wavelength, the nanowire will emit light in a narrow angle from the tip[151].
2. Increase Ω_{sun}, which is done in concentration systems, since the concentrated sun disc fill up a larger area of the sky.
3. Increase I, which we have shown to be true for nanowire solar cells.
4. Increase QE, which the 1-sun single junction record solar cells from Alta Devices do[125].

The remaining unavoidable losses in solar cells stem from thermalization losses due to absorption of high energy photons and non-absorption of photons below the bandgap. These loses are what multi-junction cells, up/down-conversion solar cells,

intermediate band solar cells, quantum well solar cell, and hot carrier solar cells are targeting. Exactly how nanowire solar cells exploit the built-in advantages, or are specifically designed in relation to Eqn. 5.1, will be important for their future success. The biggest problem, at the moment, is the quantum efficiency, and more specifically that the recombination rate is very high. We succeeded in reducing the surface recombination by passivating the surface. We haven't gotten to optimization of the doping profile, but especially considering the poor V_{oc} nanowire solar cells suffer from, the doping profile needs improvements in order to mature the technology.

5.6.3. Phase 3. Can we make it profitable?

The most likely profitability calculation for nanowire solar is efficiency/price, Sec. 1.3.

Nanowire solar cells have an advantage over planar solar cells due to how light is adsorbed and emitted from the nanostructures, but there are expected losses due to problems with electrically contacting the wires individually, as well as increased surface recombination from forcing the pn-junction into a small form factor. Therefore, it is uncertain whether single junction nanowire solar cells can compete with single junction planar devices.

It will, at a minimum, be a while before the advantages of nanowire solar cells outweigh the disadvantages for single junction cells. Therefore, nanowires have to beat planar by making MJ solar cells that utilize the fact that nanowires can be grown on lattice mismatched substrates. Our research is proceeding along this line by pursuing the GaAsP-Si dual junction, and we expect a 1-sun ~35% efficiency solar cell to be profitable. Axial heterostructures allow for several junctions in each nanowire, and it will be interesting to see how long we have to wait before someone grows one of the "perfect" triple-junction solar cell bandgap combinations (1.87eV/1.34eV/0.93eV) or (1.75eV/1.18eV/0.70eV)[15,152].

The denominator in the profitability calculation is price, and at the moment nanowire solar cells are incredible expensive to produce. The most likely growth techniques for nanowire solar cells are MOCVD and MBE, which are both expensive to use, but the material use is very small compared to planar growth, since the wires can be positioned far from each other.

A very important aspect is the price of the substrate. III-V substrates are very expensive, and the only semiconductor substrate that has a place in the market-

place is probably silicon. Otherwise very thin substrate has to be used, either by growing on a thin substrate or by epitaxial lifting off the top of the substrate and reusing the remaining substrate again [153,154]. A different approach is to grow on very different substrates such as aluminum or graphene [64,155] or forgoing the substrate completely [38].

The nanowire growth community should also move the success of nanowire growth from (111)substrates to (100)substrates to improve integration with current techniques. It may not be needed for solar cells, but for nanowire growth in general it might be necessary for commercial success.

There exist a few nanowire solar cell companies, but they are all spin-out companies from universities and still dependent on government support and/or venture capital. The commercial solar cell companies haven't yet embraced nanowire solar cell technology, but hopefully that will change soon, or even better, one of the existing nanowire-based solar cell companies can break through and start real production of nanowire based solar cells.

Bibliography

[1] NREL, Research Cell Efficiency Records. http://www.nrel.gov/ncpv/.

[2] NASA, Sun: Facts & Figures. http://solarsystem.nasa.gov/planets/profile.cfm?Object=Sun&Display=Facts&System=Metric.

[3] Hecht, E. *Optics 4th edition*; 2001.

[4] NREL, Solar Spectral Irradiance: Air Mass 1.5. http://rredc.nrel.gov/solar/spectra/am1.5/.

[5] Cotal, H.; Fetzer, C.; Boisvert, J.; Kinsey, G.; King, R.; Hebert, P.; Yoon, H.; Karam, N. *Energy Environmental Science* **2009**, *2*, 174.

[6] Fick, A. *Annalen der Physik* **1855**, *170*, 59.

[7] Drude, P. *Annalen der Physik* **1900**, *306*, 566–613.

[8] Drude, P. *Annalen der Physik* **1900**, *308*, 369–402.

[9] Shockley, W.; Read, W. *Physical Review* **1952**, *87*, 835–842.

[10] Auger, P. *C.R.A.S* **1923**, *177*, 169–171.

[11] Nelson, J. *The Physics of Solar Cells*; 2003.

[12] Green, M. A. *Solid State Electronics* **1981**, *24*, 788–789.

[13] Shockley, W.; Queisser, H. J. *Journal of Applied Physics* **1961**, *32*, 510.

[14] Byrnes, S. Shockley-Queisser limit. http://sjbyrnes.com/?page_id=15.

[15] Henry, C. H. *Journal of Applied Physics* **1980**, *51*, 4494.

[16] Meillaud, F.; Shah, A.; Droz, C.; Vallatsauvain, E.; Miazza, C. *Solar Energy Materials and Solar Cells* **2006**, *90*, 2952–2959.

[17] Yablonovitch, E.; Cody, G. *IEEE Transactions on Electron Devices* **1982**, *29*, 300–305.

[18] Bowden, S.; Honsberg, C. B. PVCDROM. `http://pveducation.org/pvcdrom`.

[19] LaPierre, R. R. *Journal of Applied Physics* **2011**, *109*, 034311.

[20] Breitenstein, O. B. O.; Altermatt, P. A. P.; Ramspeck, K. R. K.; Green, M. A. G. M. A.; Zhao, J. Z. J.; Schenk, A. S. A. *2006 IEEE 4th World Conference on Photovoltaic Energy Conference* **2006**, *1*, 879–884.

[21] Breitenstein, O.; Bauer, J.; Altermatt, P. P.; Ramspeck, K. *Solid State Phenomena* **2009**, *156-158*, 1–10.

[22] Arrhenius, S. *Zeitschrift für Physikalische Chemie* **1889**, *4*, 226.

[23] Markov, I. V. *Crystal growth for beginners : fundamentals of nucleation, crystal growth, and epitaxy*; 2003.

[24] Krogstrup, P.; Jørgensen, H. I.; Johnson, E.; Madsen, M. H.; Sørensen, C. B.; Morral, A. F. I.; Aagesen, M.; Nygård, J.; Glas, F. *Journal of Physics D: Applied Physics* **2013**, *46*, 313001.

[25] Kittel, C.; Kroemer, H. *Thermal Physics*; 1980.

[26] Gibbs, J. W.; Bumstead, H. A.; Van Name, R. G.; Longley, W. R. *The collected works of J. Willard Gibbs*; 1928.

[27] Wulff, G. *Zeitschrift für Krystallographie und Mineralogie* **1901**, *34*, 449–530.

[28] Winterbottom, W. *Acta Metallurgica* **1967**, *15*, 303–310.

[29] Brandes, H. *Zeitschrift für Physikalische Chemie* **1927**, *126*, 198.

[30] Zeldovich, Y. B. *Acta Physicochim. USSR* **1943**, *18*, 1.

[31] Kashchiev, D. *Surf Sci* **1969**, *18*, 389–397.

[32] Daweritz, L. *Surf Sci* **1990**, *236*, 15–22.

[33] Oura, K., Lifshits, V.G., Saranin, A.A., Zotov, A.V., Katayama, M. *Surface Science - An Introduction*; 2003.

[34] Geisz, J. F.; Olson, J. M.; Romero, M. J.; Jiang, C. S.; Norman, A. G. *2006 IEEE 4th World Conference on Photovoltaic Energy Conference* **2006**, *1*, 772–775.

[35] Bauer, E. *Zeitschrift für Kristallographie* **1958**, *110*, 372–394.

[36] Markov, I.; Stoyanov, S. *Contemporary Physics* **1987**, *28*, 267–320.

[37] Holmes, J. D. *Science* **2000**, *287*, 1471–1473.

[38] Heurlin, M.; Magnusson, M. H.; Lindgren, D.; Ek, M.; Wallenberg, L. R.; Deppert, K.; Samuelson, L. *Nature* **2012**, *492*, 90–4.

[39] Fortuna, S.; Li, X. *Semiconductor Science and Technology* **2010**, *25*, 024005.

[40] Choi, Y.-k.; Zhu, J.; Grunes, J.; Bokor, J.; Somorjai, G. A. *J. Phys. Chem. B* **2003**, *107*, 3340–3343.

[41] Morton, K. J.; Nieberg, G.; Bai, S.; Chou, S. Y. *Nanotechnology* **2008**, *19*, 345301.

[42] Hsu, C.-M.; Connor, S. T.; Tang, M. X.; Cui, Y. *Applied Physics Letters* **2008**, *93*, 133109.

[43] Zhu, J.; Yu, Z.; Burkhard, G. F.; Hsu, C.-M.; Connor, S. T.; Xu, Y.; Wang, Q.; McGehee, M.; Fan, S.; Cui, Y. *Nano Letters* **2009**, *9*, 279–82.

[44] Garnett, E. C.; Yang, P. *Nano Letters* **2010**, *10*, 1082–7.

[45] Garnett, E. C.; Yang, P. *Journal of the American Chemical Society* **2008**, *130*, 9224–5.

[46] Tomioka, K.; Ikejiri, K.; Tanaka, T.; Motohisa, J.; Hara, S.; Hiruma, K.; Fukui, T. *Journal of Materials Research* **2011**, *26*, 2127–2141.

[47] Mariani, G.; Scofield, A. C.; Hung, C.-H.; Huffaker, D. L. *Nature communications* **2013**, *4*, 1497.

[48] Dick, K. *Progress in Crystal Growth and Characterization of Materials* **2008**, *54*, 138–173.

[49] Wagner, R. S.; Ellis, W. C. *Applied Physics Letters* **1964**, *4*, 89–90.

[50] Messing, M. E.; Hillerich, K.; Johansson, J.; Deppert, K.; Dick, K. A. *Gold Bulletin* **2009**, *42*, 172–181.

[51] Mårtensson, T.; Borgström, M.; Seifert, W.; Ohlsson, B. J.; Samuelson, L. *Nanotechnology* **2003**, *14*, 1255–1258.

[52] Mårtensson, T.; Carlberg, P.; Borgström, M.; Montelius, L.; Seifert, W.; Samuelson, L. *Nano Letters* **2004**, *4*, 699–702.

[53] Salehzadeh, O.; Watkins, S. *Journal of Crystal Growth* **2011**, *325*, 5–9.

[54] Mikkelsen, a.; Eriksson, J.; Lundgren, E.; Andersen, J. N.; Weissenreider, J.; Seifert, W. *Nanotechnology* **2005**, *16*, 2354–2359.

[55] Sibirev, N. V.; Tchernycheva, M.; Timofeeva, M. A.; Harmand, J.-C.; Cirlin, G. E.; Dubrovskii, V. G. *Journal of Applied Physics* **2012**, *111*, 104317.

[56] Borgström, M. T.; Immink, G.; Ketelaars, B.; Algra, R.; Bakkers, E. P. A. M. *Nature Nanotechnology* **2007**, *2*, 541–544.

[57] Krogstrup, P.; Popovitz-Biro, R.; Johnson, E.; Madsen, M. H.; Nygård, J.; Shtrikman, H. *Nano Letters* **2010**, *10*, 4475–4482.

[58] Mattila, M.; Hakkarainen, T.; Lipsanen, H.; Jiang, H.; Kauppinen, E. I. *Applied Physics Letters* **2006**, *89*.

[59] Colombo, C.; Spirkoska, D.; Frimmer, M.; Abstreiter, G.; Fontcuberta I Morral, A. *Physical Review B* **2008**, *77*, 2–6.

[60] Plissard, S.; Dick, K. A.; Larrieu, G.; Godey, S.; Addad, A.; Wallart, X.; Caroff, P. *Nanotechnology* **2010**, *21*, 8.

[61] Fontcuberta I Morral, A.; Colombo, C.; Abstreiter, G.; Arbiol, J.; Morante, J. R. *Applied Physics Letters* **2008**, *92*, 063112.

[62] Plissard, S.; Larrieu, G.; Wallart, X.; Caroff, P. *Nanotechnology* **2011**, *22*, 275602.

[63] Bauer, B.; Rudolph, A.; Soda, M.; Fontcuberta I Morral, A.; Zweck, J.; Schuh, D.; Reiger, E. *Nanotechnology* **2010**, *21*, 9.

[64] Munshi, A. M.; Dheeraj, D. L.; Fauske, V. T.; Kim, D.-C.; Van Helvoort, A. T. J.; Fimland, B.-O.; Weman, H. *Nano Letters* **2012**, *12*, 4570–6.

[65] Somaschini, C.; Bietti, S.; Trampert, A.; Jahn, U.; Hauswald, C.; Riechert, H.; Sanguinetti, S.; Geelhaar, L. *Nano Letters* **2013**,

[66] Allen, J. E.; Hemesath, E. R.; Perea, D. E.; Lensch-Falk, J. L.; Li, Z. Y.; Yin, F.; Gass, M. H.; Wang, P.; Bleloch, A. L.; Palmer, R. E.; Lauhon, L. J. *Nature Nanotechnology* **2008**, *3*, 168–173.

[67] Bar-Sadan, M.; Barthel, J.; Shtrikman, H.; Houben, L. *Nano Letters* **2012**, *12*, 2352–6.

[68] Breuer, S.; Pfueller, C.; Flissikowski, T.; Brandt, O.; Grahn, H. T.; Geelhaar, L.; Riechert, H. *Nano Letters* **2011**, *11*, 1276–1279.

[69] Ahtapodov, L.; Todorovic, J.; Olk, P.; Mjåland, T.; Slåttnes, P.; Dheeraj, D. L.; Van Helvoort, A. T. J.; Fimland, B.-O.; Weman, H. *Nano Letters* **2012**, *12*, 6090–6095.

[70] Glas, F. *Physical Review B* **2006**, *74*, 2–5.

[71] Zhang, X.; Dubrovskii, V. G.; Sibirev, N. V.; Ren, X. *Crystal Growth & Design* **2011**, *11*, 5441–5448.

[72] Chuang, L. C.; Moewe, M.; Chase, C.; Kobayashi, N. P.; Chang-Hasnain, C.; Crankshaw, S. *Applied Physics Letters* **2007**, *90*, 043115.

[73] Cirlin, G. E.; Dubrovskii, V. G.; Soshnikov, I. P.; Sibirev, N. V.; Samsonenko, Y. B.; Bouravleuv, A. D.; Harmand, J.-C.; Glas, F. *Physica Status Solidi RRL* **2009**, *3*, 112–114.

[74] Biermanns, A.; Breuer, S.; Trampert, A.; Davydok, A.; Geelhaar, L.; Pietsch, U. *Nanotechnology* **2012**, *23*, 305703.

[75] Davydok, A.; Breuer, S.; Biermanns, A.; Geelhaar, L.; Pietsch, U. *Nanoscale Research Letters* **2012**, *7*, 109.

[76] Wen, C. Y.; Tersoff, J.; Reuter, M.; Stach, E.; Ross, F. *Physical Review Letters* **2010**, *105*, 1–4.

[77] Hofmann, S.; Sharma, R.; Wirth, C. T.; Cervantes-Sodi, F.; Ducati, C.; Kasama, T.; Dunin-Borkowski, R. E.; Drucker, J.; Bennett, P.; Robertson, J. *Nature Materials* **2008**, *7*, 372–375.

[78] Glas, F.; Harmand, J.-C.; Patriarche, G. *Physical Review Letters* **2007**, *99*, 4.

[79] Johansson, J.; Karlsson, L. S.; Svensson, C. P. T.; Mårtensson, T.; Wacaser, B. A.; Deppert, K.; Samuelson, L.; Seifert, W. *Nature Materials* **2006**, *5*, 574–80.

[80] Krogstrup, P.; Curiotto, S.; Johnson, E.; Aagesen, M.; Nygård, J.; Chatain, D. *Physical Review Letters* **2011**, *106*, 125505.

[81] Caroff, P.; Dick, K. A.; Johansson, J.; Messing, M. E.; Deppert, K.; Samuelson, L. *Nature Nanotechnology* **2009**, *4*, 50–55.

[82] Oh, S. H.; Chisholm, M. F.; Kauffmann, Y.; Kaplan, W. D.; Luo, W.; Rühle, M.; Scheu, C. *Science* **2010**, *330*, 489–493.

[83] Gamalski, A. D.; Ducati, C.; Hofmann, S. *The Journal of Physical Chemistry C* **2011**, *115*, 4413–4417.

[84] Wen, C.-Y.; Tersoff, J.; Hillerich, K.; Reuter, M. C.; Park, J. H.; Kodambaka, S.; Stach, E. A.; Ross, F. M. *Physical Review Letters* **2011**, *107*, 025503.

[85] Wang, H.; Zepeda-Ruiz, L. A.; Gilmer, G. H.; Upmanyu, M. *Nature communications* **2013**, *4*, 1956.

[86] Kroemer, H. *Journal of Crystal Growth* **1987**, *81*, 193–204.

[87] Patriarche, G.; Glas, F.; Tchernycheva, M.; Sartel, C.; Largeau, L.; Harmand, J.-C.; Cirlin, G. E. *Nano Letters* **2008**, *8*, 1638–1643.

[88] Perea, D. E.; Li, N.; Dickerson, R. M.; Misra, A.; Picraux, S. T. *Nano Letters* **2011**, *11*, 3117–3122.

[89] Chen, C.; Shehata, S.; Fradin, C.; LaPierre, R.; Couteau, C.; Weihs, G. *Nano Letters* **2007**, *7*, 20.

[90] Borgström, M. T.; Wallentin, J.; Trägårdh, J.; Ramvall, P.; Ek, M.; Wallenberg, L. R.; Samuelson, L.; Deppert, K. *Nano Research* **2010**, *3*, 264–270.

[91] Caroff, P.; Wagner, J. B.; Dick, K. A.; Nilsson, H. A.; Jeppsson, M.; Deppert, K.; Samuelson, L.; Wallenberg, L. R.; Wernersson, L.-E. *Small* **2008**, *4*, 878–82.

[92] Wallentin, J.; Borgström, M. T. *Journal of Materials Research* **2011**, *26*, 2142–2156.

[93] Casadei, A.; Krogstrup, P.; Heiss, M.; Rohr, J. A.; Colombo, C.; Ruelle, T.; Upadhyay, S.; Sørensen, C. B.; Nygård, J.; Morral, A. F. I. *Applied Physics Letters* **2013**, *102*.

[94] Connell, J. G.; Yoon, K.; Perea, D. E.; Schwalbach, E. J.; Voorhees, P. W.; Lauhon, L. J. *Nano Letters* **2012**,

[95] Perea, D. E.; Allen, J. E.; May, S. J.; Wessels, B. W.; Seidman, D. N.; Lauhon, L. J. *Nano Letters* **2006**, *6*, 181–185.

[96] Perea, D. E.; Hemesath, E. R.; Schwalbach, E. J.; Lensch-Falk, J. L.; Voorhees, P. W.; Lauhon, L. J. *Nature Nanotechnology* **2009**, *4*, 315–319.

[97] Kavanagh, K. L.; Saveliev, I.; Blumin, M.; Swadener, G.; Ruda, H. E. *Journal of Applied Physics* **2012**, *111*.

[98] Kavanagh, K. L. *Semiconductor Science and Technology* **2010**, *25*, 7.

[99] Raychaudhuri, S.; Yu, E. T. *Journal of Vacuum Science and Technology B* **2006**, *24*, 2053.

[100] LaPierre, R. R.; Chia, a. C. E.; Gibson, S. J.; Haapamaki, C. M.; Boulanger, J.; Yee, R.; Kuyanov, P.; Zhang, J.; Tajik, N.; Jewell, N.; Rahman, K. M. a. *Physica Status Solidi - RRL* **2013**, DOI: 10.1002/pssr.201307109.

[101] Tian, B.; Kempa, T. J.; Lieber, C. M. *Chemical Society Reviews* **2009**, *38*, 16–24.

[102] Garnett, E. C.; Brongersma, M. L.; Cui, Y.; McGehee, M. D. *Annual Review of Materials Research* **2011**, *41*, 269–295.

[103] Novotny, C. J.; Yu, E. T.; Yu, P. K. L. *Nano Letters* **2008**, *8*, 775–779.

[104] Bi, H.; Lapierre, R. R. *Nanotechnology* **2009**, *20*, 465205.

[105] Mariani, G.; Laghumavarapu, R. B.; Tremolet De Villers, B.; Shapiro, J.; Senanayake, P.; Lin, A.; Schwartz, B. J.; Huffaker, D. L. *Applied Physics Letters* **2010**, *97*, 013107.

[106] Chao, J.-J.; Shiu, S.-C.; Lin, C.-F. *Solar Energy Materials and Solar Cells* **2012**, *105*, 40–45.

[107] Tang, Y. B.; Chen, Z. H.; Song, H. S.; Lee, C. S.; Cong, H. T.; Cheng, H. M.; Zhang, W. J.; Bello, I.; Lee, S. T. *Nano Letters* **2008**, *8*, 4191–4195.

[108] Cirlin, G.; Bouravleuv, A.; Soshnikov, I.; Samsonenko, Y. B.; Dubrovskii, V.; Arakcheeva, E.; Tanklevskaya, E.; Werner, P. *Nanoscale Research Letters* **2009**, *5*, 360–363.

[109] Wei, W.; Bao, X.-Y.; Soci, C.; Ding, Y.; Wang, Z.-L.; Wang, D. *Nano Letters* **2009**, *9*, 2926–2934.

[110] Shin, J. C.; Kim, K. H.; Yu, K. J.; Hu, H.; Yin, L.; Ning, C.-Z.; Rogers, J. A.; Zuo, J.-M.; Li, X. *Nano Letters* **2011**, *11*, 4831–8.

[111] Han, N.; Wang, F.; Yip, S.; Hou, J. J.; Xiu, F.; Shi, X.; Hui, A. T.; Hung, T.; Ho, J. C. *Applied Physics Letters* **2012**, *101*, 013105.

[112] Miller, O. D.; Yablonovitch, E.; Kurtz, S. R. *IEEE Journal of Photovoltaics* **2012**, *2*, 303–311.

[113] Tian, B.; Zheng, X.; Kempa, T. J.; Fang, Y.; Yu, N.; Yu, G.; Huang, J.; Lieber, C. M. *Nature* **2007**, *449*, 885–889.

[114] Colombo, C.; Heiss, M.; Gratzel, M.; Fontcuberta I Morral, A. *Applied Physics Letters* **2009**, *94*, 173108.

[115] Heurlin, M.; Wickert, P.; Fält, S.; Borgström, M. T.; Deppert, K.; Samuelson, L.; Magnusson, M. H. *Nano Letters* **2011**, *11*, 2028–2031.

[116] Gutsche, C.; Lysov, A.; Braam, D.; Regolin, I.; Keller, G.; Li, Z.-A.; Geller, M.; Spasova, M.; Prost, W.; Tegude, F.-J. *Advanced Functional Materials* **2012**, *22*, 929–936.

[117] Li, J.; Yu, H.; Wong, S. M.; Li, X.; Zhang, G.; Lo, P. G.-Q.; Kwong, D.-L. *Applied Physics Letters* **2009**, *95*, 243113.

[118] Lin, C.; Povinelli, M. L. *Optics Letters* **2010**, *35*, 3378–3380.

[119] Wen, L.; Zhao, Z.; Li, X.; Shen, Y.; Guo, H.; Wang, Y. *Applied Physics Letters* **2011**, *99*, 143116.

[120] Hu, Y.; LaPierre, R. R.; Li, M.; Chen, K.; He, J.-J. *Journal of Applied Physics* **2012**, *112*, 104311.

[121] Oskooi, A. F.; Roundy, D.; Ibanescu, M.; Bermel, P.; Joannopoulos, J. D.; Johnson, S. G. *Computer Physics Communications* **2010**, *181*, 687–702.

[122] Heiss, M.; Fontcuberta I Morral, A. *Applied Physics Letters* **2011**, *99*, 263102.

[123] Cao, L.; White, J. S.; Park, J.-S.; Schuller, J. A.; Clemens, B. M.; Brongersma, M. L. *Nature Materials* **2009**, *8*, 643–647.

[124] Colombo, C.; Krogstrup, P.; Nygård, J.; Brongersma, M. L.; Morral, A. F. I. *New Journal of Physics* **2011**, *13*, 123026.

[125] Kayes, B. M.; Nie, H.; Twist, R.; Spruytte, S.; Reinhardt, F.; Kizilyalli, I.; Higashi, G. *Photovoltaic Specialists Conference (PVSC), 2011 37th IEEE* **2011**, 000004.

[126] LaPierre, R. R. *Journal of Applied Physics* **2011**, *110*, 014310.

[127] Kayes, B. M.; Atwater, H. A.; Lewis, N. S. *Journal of Applied Physics* **2005**, *97*, 114302.

[128] Mohseni, P. K.; Rodrigues, A. D.; Galzerani, J. C.; Pusep, Y. A.; LaPierre, R. R. *Journal of Applied Physics* **2009**, *106*, 124306.

[129] Tchernycheva, M.; Rigutti, L.; Jacopin, G.; De Luna Bugallo, A.; Lavenus, P.; Julien, F. H.; Timofeeva, M.; Bouravleuv, A. D.; Cirlin, G. E.; Dhaka, V.; Lipsanen, H.; Largeau, L. *Nanotechnology* **2012**, *23*, 265402.

[130] Tajik, N.; Peng, Z.; Kuyanov, P.; LaPierre, R. R. *Nanotechnology* **2011**, *22*, 225402.

[131] Yu, S.; Roemer, F.; Witzigmann, B. *Solar Energy* **2012**, *8438*, 84380O–84380O–8.

[132] Mariani, G.; Wong, P.-S.; Katzenmeyer, A. M.; Léonard, F.; Shapiro, J.; Huffaker, D. L. *Nano Letters* **2011**, *11*, 2490–2494.

[133] Goto, H.; Nosaki, K.; Tomioka, K.; Hara, S.; Hiruma, K.; Motohisa, J.; Fukui, T. *Applied Physics Express* **2009**, *2*, 035004.

[134] Yoshimura, M.; Nakai, E.; Tomioka, K.; Fukui, T. *Applied Physics Express* **2013**, *6*, 052301.

[135] Wallentin, J.; Anttu, N.; Asoli, D.; Huffman, M.; åberg, I.; Magnusson, M. H.; Siefer, G.; Fuss-Kailuweit, P.; Dimroth, F.; Witzigmann, B.; Xu, H. Q.; Samuelson, L.; Deppert, K.; Borgström, M. T. *Science* **2013**,

[136] Cui, Y.; Wang, J.; Plissard, S. R.; Cavalli, A.; Vu, T. T. T.; van Veldhoven, R. P. J.; Gao, L.; Trainor, M.; Verheijen, M. a.; Haverkort, J. E. M.; Bakkers, E. P. a. M. *Nano Letters* **2013**,

[137] Green, M. A.; Emery, K.; Hishikawa, Y.; Warta, W.; Dunlop, E. D. *Progress in Photovoltaics: Research and Applications* **2013**, *21*, 1–11.

[138] NREL, 31.1% Efficiency for III-V Solar Cell. 2013; `http://www.nrel.gov/news/press/2013/2226.html`.

[139] Kempa, T. J.; Tian, B.; Kim, D. R.; Hu, J.; Zheng, X.; Lieber, C. M. *Nano Letters* **2008**, *8*, 3456–3460.

[140] Dong, Y.; Tian, B.; Kempa, T. J.; Lieber, C. M. *Nano Letters* **2009**, *9*, 2183–2187.

[141] Nguyen, H. P. T.; Chang, Y.-L.; Shih, I.; Mi, Z. *IEEE Journal of Selected Topics in Quantum Electronics* **2011**, *17*, 1062–1069.

[142] Joyce, H. J.; Wong-Leung, J.; Yong, C.-K.; Docherty, C. J.; Paiman, S.; Gao, Q.; Tan, H. H.; Jagadish, C.; Lloyd-Hughes, J.; Herz, L. M.; Johnston, M. B. *Nano Letters* **2012**, *12*, 5325–30.

[143] Kelzenberg, M. D.; Boettcher, S. W.; Petykiewicz, J. a.; Turner-Evans, D. B.; Putnam, M. C.; Warren, E. L.; Spurgeon, J. M.; Briggs, R. M.; Lewis, N. S.; Atwater, H. a. *Nature materials* **2010**, *9*, 239–44.

[144] Pickett, E.; Gu, A. G. A.; Huo, Y. H. Y.; Garnett, E.; Hu, S. H. S.; Sarmiento, T.; Thombare, S.; Liang, D. L. D.; Li, S. L. S.; Cui, Y. C. Y.; McGehee, M.; McIntyre, P.; Harris, J. *Photovoltaic Specialists Conference PVSC 2010 35th IEEE* **2010**, 1848–1853.

[145] Bao, H.; Ruan, X. *Optics Letters* **2010**, *35*, 3378–80.

[146] Hobart, K. D.; Thompson, P. E.; Rommel, S. L.; Dillon, T. E.; Berger, P. R.; Simons, D. S.; Chi, P. H. *Journal of Vacuum Science & Technology B: Microelectronics and Nanometer Structures* **2001**, *19*, 290.

[147] Oehme, M.; Hahnel, D.; Werner, J.; Kaschel, M.; Kirfel, O.; Kasper, E.; Schulze, J. *Applied Physics Letters* **2009**, *95*, 242109.

[148] Bjrk, M. T.; Schmid, H.; Bessire, C. D.; Moselund, K. E.; Ghoneim, H.; Karg, S.; Lortscher, E.; Riel, H. *Applied Physics Letters* **2010**, *97*, 163501–1635013.

[149] Yang, T.; Hertenberger, S.; Morkotter, S.; Abstreiter, G.; Koblmuller, G. *Applied Physics Letters* **2012**, *101*, 233102.

[150] Polman, A.; Atwater, H. A. *Nature Materials* **2012**, *11*, 174–7.

[151] Claudon, J.; Bleuse, J.; Malik, N. S.; Bazin, M.; Jaffrennou, P.; Gregersen, N.; Sauvan, C.; Lalanne, P.; Gérard, J.-M. *Nature Photonics* **2010**, *4*, 174–177.

[152] Friedman, D. J. *Current Opinion in Solid State and Materials Science* **2010**, *14*, 131–138.

[153] Yablonovitch, E.; Gmitter, T.; Harbison, J. P.; Bhat, R. *Applied Physics Letters* **1987**, *51*, 2222.

[154] Bauhuis, G. J.; Mulder, P.; Haverkamp, E. J.; Huijben, J. C. C. M.; Schermer, J. J. *Solar Energy Materials and Solar Cells* **2009**, *93*, 1488–1491.

[155] Adachi, M. M.; Anantram, M. P.; Karim, K. S. *Scientific reports* **2013**, *3*, 1546.

A. Published articles

I: Surface-passivated GaAsP single-nanowire solar cells exceeding 10% efficiency grown on silicon

Jeppe V. Holm*, Henrik I. Jørgensen*, Peter Krogstrup, Jesper Nygård, Huiyun Liu & Martin Aagesen*

Reprinted with permission from Nature Publishing Group. First published as: *Nature Communications,* **4**, Article number: 1498 (2013)

nature COMMUNICATIONS

ARTICLE

Received 29 Nov 2012 | Accepted 17 Jan 2013 | Published 19 Feb 2013

DOI: 10.1038/ncomms2510

Surface-passivated GaAsP single-nanowire solar cells exceeding 10% efficiency grown on silicon

Jeppe V. Holm[1,*], Henrik I. Jørgensen[1,*], Peter Krogstrup[2], Jesper Nygård[2,3], Huiyun Liu[4] & Martin Aagesen[1,*]

Continued development of high-efficiency multi-junction solar cells requires growth of lattice-mismatched materials. Today, the need for lattice matching both restricts the bandgap combinations available for multi-junctions solar cells and prohibits monolithic integration of high-efficiency III-V materials with low-cost silicon solar cells. The use of III-V nanowires is the only known method for circumventing this lattice-matching constraint, and therefore it is necessary to develop growth of nanowires with bandgaps >1.4 eV. Here we present the first gold-free gallium arsenide phosphide nanowires grown on silicon by means of direct epitaxial growth. We demonstrate that their bandgap can be controlled during growth and fabricate core-shell nanowire solar cells. We further demonstrate that surface passivation is of crucial importance to reach high efficiencies, and present a record efficiency of 10.2% for a core-shell single-nanowire solar cell.

[1] SunFlake A/S, Universitetsparken 5, Copenhagen DK-2100, Denmark. [2] Nano-Science Center, Niels Bohr Institute, University of Copenhagen, Universitetsparken 5, Copenhagen, DK-2100, Denmark. [3] Center for Quantum Devices, Niels Bohr Institute, University of Copenhagen, Universitetsparken 5, Copenhagen DK-2100, Denmark. [4] Department of Electronic and Electrical Engineering, University College London, London WC1E 7JE, UK. * These authors contributed equally to this work. Correspondence and requests for materials should be addressed to M.A. (email: martin.aagesen@sunflake.dk).

Improving the cost/efficiency ratio of III-V-based multi-junction cells can be done through efficiency enhancements, by adding additional junctions to the cell stack[1] or through the lowering of cost by replacing the expensive germanium substrate with silicon. Integrating III-V semiconductors and silicon requires overcoming their differences in lattice parameters and thermal expansion coefficient, as well as their polar/non-polar interfaces[2,3]. When constrained to a silicon-bottom cell, the optimum dual-junction solar cell, the simplest multi-junction solar cell, has a theoretical 1-sun peak efficiency between 33 and 43% (refs 4,5) when combined with a 1.7 eV bandgap top cell; this can be achieved with a III-V semiconductor consisting of $GaAs_{0.8}P_{0.2}$.

The small contact interface between the nanowire and the silicon substrate ensures that strain from lattice mismatch is relaxed within the first few monolayers[6]. Using the method of gallium (Ga)-assisted growth, gold-free perfect single crystal, gallium arsenide (GaAs) nanowires have been grown directly on silicon[7]. Higher bandgap gallium phosphide (GaP)[8] and gallium arsenide phosphide (GaAsP)[9,10] nanowires have also been grown, but only using gold as growth catalyst. Gold is incompatible with silicon[11], and has been shown to incorporate into the III-V crystal[12] and degrade the optoelectronic properties of the nanowires[13]. In addition, a sparse array of nanowires can absorb almost all incoming light[14], meaning that only minute amounts of the expensive III-V material is needed for making a nanowire top cell. Devices consisting of a contacted ensemble of free-standing nanowires have been exposed to temperature changes of up to 200 K, demonstrating that their strain-relieving ability is able to overcome the difference in thermal expansion[15]. To fully utilize their advantage with regards to non-lattice-matched growth, the nanowires themselves must also be able to function well as solar cells.

Results

Ga-assisted $GaAs_{0.8}P_{0.2}$ nanowire growth. High-quality GaAsP nanowires were grown without the use of a buffer layer on epi-ready Si(111) substrates having a native oxide surface layer. Solid-source molecular beam epitaxy (MBE) was used for the growths. The Ga-assisted vapour–liquid–solid growth method demonstrated with GaAs nanowires[7,16] was adapted to allow for the difference in nucleation energy caused by the addition of P to the growth environment. Direct substitution of an As beam flux with a similar P beam equivalent pressure, resulted in a high nucleation rate that caused the Ga droplet to disappear. By lowering the V/III flux ratio, the nucleation rate was decreased and the Ga droplet maintained throughout the nanowire growth (Fig. 1a,b). The growth parameters: V/III flux ratio, P/As flux ratio and temperature, yielding the highest crystal quality, were determined by inspecting the wires using transmission electron microscopy (Fig. 1b and Supplementary Figs S1–S3). The different diffusion lengths and incorporation rates of P and As, in combination with the changing growth landscape, mean that the P/As flux ratio needs to be adjusted throughout the growth (Fig. 1c). We were able to grow nanowires with constant P content as well as graded nanowires with P content varied from $x = 0.15$ to $x = 0.70$ ($GaAs_{1-x}P_x$) along the wire axis (Supplementary Fig. S4). With a systematic focus on the growth parameters, Ga-assisted $GaAs_{0.8}P_{0.2}$ nanowires with a 1.7 eV bandgap consisting of a close to perfect zinc-blende crystal were successfully produced. The bandgap of nanowire ensembles was determined using room temperature photoluminescence (PL) and further verified on individual nanowires by energy-dispersive X-ray spectroscopy (Supplementary Figs S4 and S5).

Core-shell nanowire solar-cell fabrication. Solar-cell structures were made by fabricating p–i–n core-shell GaAsP nanowires. The core-shell p–i–n-junction growth method allows for the design of optimal doping densities and layer thicknesses. Further, the radial p–i–n junction ensures a sufficient optical absorption length while minimizing the carrier-extraction distance. First, a p-type core nanowire was grown by introducing beryllium during the axial vapour–liquid–solid growth. A Ga-free step was added to let the group V material consume the Ga droplets and halt further axial growth. Then, two GaAsP shells were grown around the As-grown nanowires, using vapour–solid (VS) epitaxial growth, the first one intrinsic and the second one n-type by doping with silicon. Before the radial shell growth, the substrate temperature was lowered to avoid beryllium diffusion and to enhance n-type

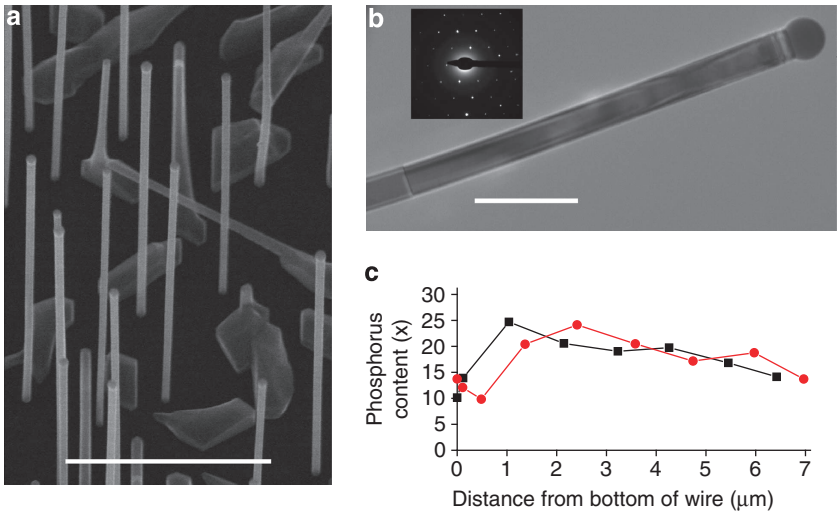

Figure 1 | Ga-assisted $GaAs_{1-x}P_x$ nanowires grown directly on silicon. (**a**) Scanning electron microscope image of GaAsP nanowires, each having a Ga droplet on top. The nanowires are seen from above at an angle of 25°. Scale bar, 1 μm. (**b**) Transmission electron microscope image showing the upper part of a GaAsP nanowire with only a few twinnings visible just below the Ga droplet and further down the nanowire. Scale bar, 200 nm. Inset: diffraction image showing the nanowires zinc-blende crystal structure, expanded in Supplementary Fig. S3. (**c**) Energy-dispersive X-ray spectroscopy characterization of P content (*x*-value) in two nanowires from the same growth. The variation in P during the first 1 μm of the growth is due to a deliberate flux change, whereas the downward slope is under a constant flux.

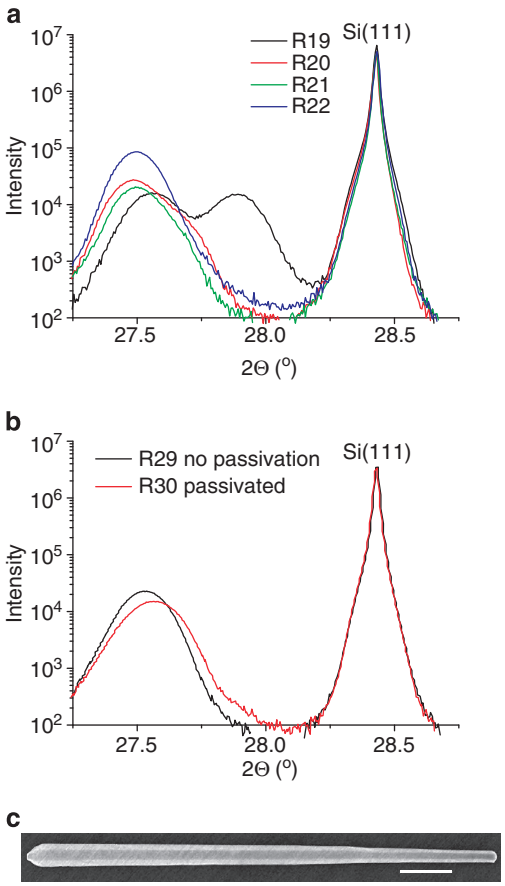

Figure 2 | Lattice matching of the $GaAs_{1-x}P_x$ shell using X-ray diffraction. (**a**) A GaAsP core-shell growth series consisting of four growths with identical core growth parameters. The series was aligned using the sharp Si(111) peak from the substrate. The peaks to the left are from the nanowire crystal, and any shift or broadening of the peaks towards the right represents a shift in lattice size towards a higher P content. (**b**) Two GaAsP core-shell growths with the only difference being the addition of an InGaP passivation layer to R30. The unpassivated and passivated SNWSCs were fabricated using nanowires from these two growths. (**c**) Scanning electron microscope image of a core-shell GaAsP nanowire from the same growth as the best device. Scale bar, 1 μm.

doping of the silicon. As and P have different incorporation rates during planer (VS) film growth, and these rates further depend on beam fluxes and growth temperature. To grow a lattice-matched shell around the core nanowire, a series of core-shell growths were carried out to optimize the growth parameters. The growths were characterized using X-ray diffraction, which shows mismatched lattice sizes as multiple peaks in the data plot. For the ideal core-shell nanowire growth, only two peaks should be visible, one from the silicon crystal lattice in the substrate and one from the GaAsP core-shell nanowire. The first growth (R19) in the series had a too high P content in the shell (Fig. 2a). The final growth (R22) in the series showed only one III-V peak, indicating a lattice-matched core and shell. The $GaAs_{0.8}P_{0.2}$ (111) peak should yield a $2\Theta \approx 27.5°$, which correlates well with the R22 growth.

Single-nanowire solar cell (SNWSC) characterization. To produce SNWSCs, the nanowires were removed from the growth substrate, placed on an oxide covered silicon substrate and contacted at both ends (see Fig. 3c and Methods for details on the fabrication scheme). The SNWSCs were characterized individually by measuring current-voltage curves in the dark and under AM1.5G illumination. The best unpassivated SNWSC had an efficiency of 6.8%, short circuit current $I_{SC} = 13.2\,mA\,cm^{-2}$, open circuit voltage $V_{OC} = 0.76\,V$ and fill factor (FF) = 0.68 (Fig. 3a). This efficiency is higher than what has previously been reported[17–19], but still considerably lower than the theoretical Shockley–Queisser limit, which for a 1.7 eV bandgap is 29%, $I_{SC} \sim 23\,mA\,cm^{-2}$, $V_{OC} \sim 1.4\,V$ and FF ~ 0.9 (ref. 20). For a device geometry similar to ours, it is predicted that roughly half of the projected sunlight is absorbed[21], which accounts well for the discrepancy between measured and Shockley–Queisser I_{SC}. The measured V_{OC} is also about half of the Shockley–Queisser limit, but this cannot be accounted for by the low absorption in this solar-cell geometry. A low V_{OC} is often attributed to non-optimal doping of the n- and p-region or inadequate surface passivation.

Surface passivation. Because nanowire solar cells have a high surface to volume ratio compared with planar solar cells, it is critical to passivate the surface of the wires, that is, stopping charge carriers from reaching the surface and recombining at surface states. Simulations on InP core-shell nanowires predicted a 32% improvement in efficiency when reducing the surface recombination[22]. By growing an additional shell of ~10 nm highly n-doped InGaP, we have for the first time applied surface passivation to III-V nanowire solar cells (Fig. 2b,c). The clear faceting in Fig. 2c is a signature of a highly crystalline core-shell growth. Using the passivated nanowires, SNWSCs similar to the unpassivated ones were fabricated. Because the rate of surface recombination typically increases rapidly with bias, introducing a surface-passivation layer should give a large increase in V_{OC} and only a small increase in I_{SC}, which is precisely what we observe (Fig. 3b). Another typical sign of a high recombination rate is a low FF and a high ideality factor. The passivation layer increased the fill-factor from 0.68 to 0.77 and decreased the ideality factor from 2.2 to 2.0, indicating that we indeed have lowered the rate of surface recombination (Table 1). With the introduction of a passivation layer, we have been able to significantly increase the peak efficiency to >10% and the average efficiency by 72% (Fig. 3d,e). Characterization as a function of laser wavelength further confirms a 1.7-eV bandgap, because the external quantum efficiency is zero below the bandgap of the nanowire and increases sharply around 1.7 eV (Fig. 3f).

Discussion

Our realization of GaAsP semiconductor structures directly on silicon, and the excellent performance of the SNWSCs, demonstrates essential steps towards a robust high-efficiency and low-cost dual-junction solar cell. Furthermore, this record SNWSC efficiency has been achieved despite the less than optimal bandgap of GaAsP as a single-junction cell. We still need to optimize the individual nanowires to reach efficiencies close to the Shockley–Queisser limit. We have here demonstrated the first attempt on optimizing the open circuit voltage and FF by means of surface passivation, but have yet to focus on doping concentrations and layer thicknesses in the p–i–n junction. There are additional challenges towards a dual-junction nanowire/planar solar cell. For homogeneous growth and light management, the nanowires should be grown in a positioned array[23] and contacted[24]. The nanowire array must furthermore be produced without any parasitic bulk growth between the nanowires, which will function as Shockley Read Hall recombination centres. The array must be grown on a (111) silicon solar cell, and a tunnel junction must be implemented between the two junctions. The GaAsP/Si dual-junction solar cell is only one example of how nanowires can be used to produce more cost-efficient multi-junction solar cells in the future. The inherent ability of

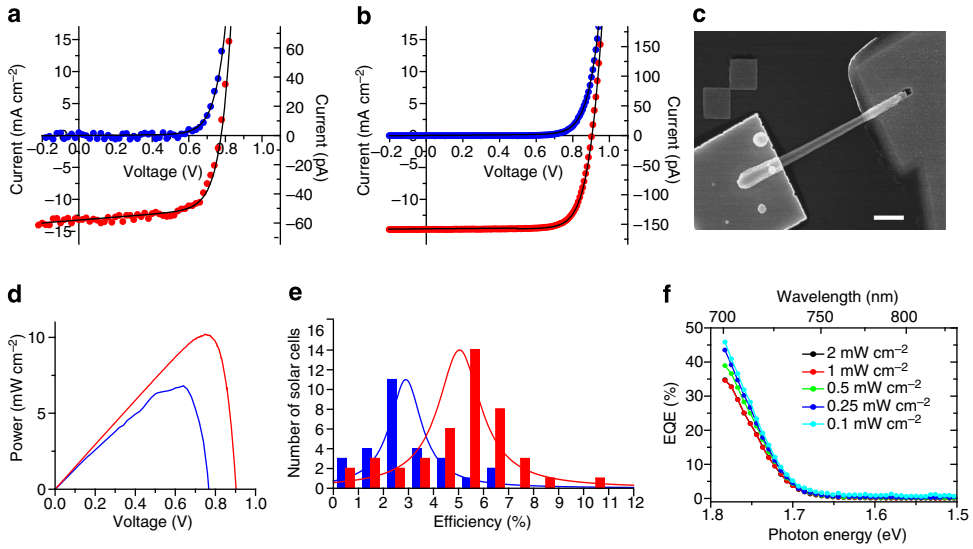

Figure 3 | Characterization of SNWSCs with and without passivation. (**a**,**b**) I-V characteristics under dark (blue dots) and AM1.5G illuminated conditions (red dots) of (**a**) the unpassivated and (**b**) passivated SNWSCs with the highest efficiency. The black line is a fit to the data. Passivation increased the efficiency by 50%. (**c**) A scanning electron microscope image of the best passivated device. Scale bar, 1 μm. (**d**) P–V comparison between the best passivated ($P_{max} = 10.2\,mW\,cm^{-2}$) (red) and unpassivated ($P_{max} = 6.8\,mW\,cm^{-2}$) (blue) SNWSC. (**e**) Histogram of the 1-sun efficiency of 28 unpassivated (blue) and 43 passivated (red) SNWSCs. The Lorentzian fit shows that the passivation has increased the average efficiency by 72% (5.0% for the passivated versus 2.9% for the unpassivated). (**f**) External quantum efficiency (EQE) versus photon energy of the SNWSC in **b**,**c**.

Table 1 | Key performance parameters of the three best passivated and unpassivated SNWSCs

	Passivated			Unpassivated		
	1	2	3	1	2	3
Efficiency (%)	10.2	8.2	7.6	6.8	6.4	5.0
I_{SC} (mA cm^{-2})	14.7	14.2	11.9	13.2	13.8	14.3
V_{OC} (V)	0.9	0.8	0.88	0.76	0.74	0.64
FF	0.77	0.72	0.72	0.68	0.62	0.55
Ideality factor	2.0	2.2	2.2	2.2	2.6	2.7

nanowires to relieve strain while conserving crystal quality means that lattice matching between two or more of the solar-cell junctions can be relaxed, thereby allowing for new and better bandgap combinations to be used. Our growth method should enable growth of nanowires in the full 1.42–2.26 eV GaAsP bandgap range, which could facilitate their use as both the top junction in a III-V on Si dual-junction solar cell and a fourth junction in a four-junction solar cell.

In conclusion, we have demonstrated high-quality gold-free GaAsP nanowires, grown directly on silicon, with an optimum bandgap for use in a dual-junction silicon-based solar cell. The nanowires have intrinsic properties that overcome the requirements for lattice matching, as well as the difference in thermal expansion coefficient and polar/non-polar interface, which until now have hampered III-V on silicon growth. A surface-passivated GaAsP SNWSC has achieved a 1-sun record efficiency of 10.2%, which effectively doubles the previous SNWSC record[17–19].

Methods

Crystal growth. The GaAsP core-shell nanowires were fabricated using solid-source III-V MBE. Substrates of 380-μm thick B-doped Si(111) with a thin layer of native oxide were used in the experiments. To enhance the reproducibility between growths, the substrates were first heated to 1100 °C in the MBE system to remove the existing layer of surface oxide, and afterwards kept for 24 h in the clean room before being re-loaded into the MBE system. Using the method of Ga-assisted growth, the core nanowires were grown by means of a Ga droplet that formed on the silicon surface during the first few seconds of the growth procedure. The core-nanowire growths were carried out at a substrate temperature ranging between 620 and 650 °C measured using a pyrometer. For the core growth series, the Ga flux was varied between the growths but kept within the range of 4×10^{-8}–9×10^{-8} torr. The group V flux was also varied between growths but was within the range of 2.8×10^{-6}–7.0×10^{-6} torr. Core-nanowire growth times were up to 1 h. Following core-nanowire growth, the Ga shutter was closed to interrupt axial growth. During the 10–20 min growth interrupt, the Ga droplets were consumed by the group V fluxes, and the temperature was lowered to 460–470 °C where shell growth was carried out. For p-type doping of the core, a Be doping density corresponding to $8 \times 10^{17}\,cm^{-3}$ for planar growth of GaAs at $1\,ML\,s^{-1}$ was used, and for the n-type shell growth, a silicon doping density corresponding to 0.8×10^{18}–$1.3 \times 10^{18}\,cm^{-3}$ for planar growth at $1\,ML\,s^{-1}$ was used.

Device fabrication. The wires were removed from the growth substrate by sonication in isopropanol and drip dried onto strongly p-doped Si(100) substrates covered with 500 nm thermal SiO_2 and pre-fabricated alignment marks. The contact to the p-doped core was defining using e-beam lithography followed by a 45–60 s etch at 30 °C in H_3PO_4:H_2O_2:H_2O (1:1:15) to expose the core and subsequent thermal evaporation of 5 nm Au/30 nm Zn/150 nm Au. The p-contact was annealed for 2 min at 420 °C in a N_2 atmosphere. Contact to the n-doped wire surface was defined using e-beam lithography followed by a 20 s B-HF etch to remove oxide and a quick load into the evaporation chamber. Several n-contacts have been tested. The results in this article have been achieved with unannealed 40 nm Ge/60 nm Au/27 nm Ni/200 nm Au, annealed 100 nm Ge/100 nm Au for 2 min at 300 °C in a N_2 atmosphere and annealed 6 nm In/240 nm Au-Ge eutectic for 2 min at 300 °C in a N_2 atmosphere. Contact pads were defined using ultraviolet lithography and consist of e-beam evaporated 10 nm Ti/150 nm Au.

Optical characterization. Solar illumination was done with a standard solar simulator (LOT—Oriel 150 W Xe lamp) with a 1′ beam diameter and an AM1.5G filter. The 1-sun intensity was verified using a mono-crystalline silicon solar cell calibrated at Radboud University Nijmegen against a National Renewable Energy Laboratory (NREL) secondary cell standard.

For the quantum efficiency measurements, a continuous wave titanium sapphire laser, tuneable from 700 to 1000 nm, was used.

References

1. King, R. R. *et al.* Solar cell generations over 40% efficiency. *Prog. Photovoltaics Res. Appl.* **20,** 801–815 (2012).
2. Fang, S. F. *et al.* Gallium arsenide and other compound semiconductors on silicon. *J. Appl. Phys.* **68,** R31 (1990).
3. Moutanabbir, O. & Gösele, U. Heterogeneous integration of compound semiconductors. *Ann. Rev. Mater. Res.* **40,** 469–500 (2010).

4. Meillaud, F., Shah, A., Droz, C., Vallat-Sauvain, E. & Miazza, C. Efficiency limits for single-junction and tandem solar cells. *Solar Energ. Mater. Solar Cells* **90,** 2952–2959 (2006).
5. LaPierre, R. R. Theoretical conversion efficiency of a two-junction III-V nanowire on Si solar cell. *J. Appl. Phys.* **110,** 014310 (2011).
6. Davydok, A., Breuer, S., Biermanns, A., Geelhaar, L. & Pietsch, U. Lattice parameter accommodation between GaAs (111) nanowires and Si (111) substrate after growth via Au-assisted molecular beam epitaxy. *Nanoscale Res. Lett.* **7,** 109 (2012).
7. Krogstrup, P. *et al.* Structural phase control in self-catalyzed growth of gaas nanowires on silicon (111). *Nano. Lett.* **10,** 4475–4482 (2010).
8. Mårtensson, T. *et al.* Epitaxial III − V nanowires on silicon. *Nano. Lett.* **4,** 1987–1990 (2004).
9. Mohseni, P. K., Rodrigues, A. D., Galzerani, J. C., Pusep, Y. A. & LaPierre, R. R. Structural and optical analysis of GaAsP/GaP core-shell nanowires. *J. Appl. Phys.* **106,** 124306 (2009).
10. Tchernycheva, M. *et al.* Photovoltaic properties of GaAsP core–shell nanowires on Si(001) substrate. *Nanotechnology* **23,** 265402 (2012).
11. Dubois, S., Palais, O., Pasquinelli, M., Martinuzzi, S. & Jaussaud, C. Influence of substitutional metallic impurities on the performances of p-type crystalline silicon solar cells: The case of gold. *J. Appl. Phys.* **100,** 123502 (2006).
12. Bar-Sadan, M., Barthel, J., Shtrikman, H. & Houben, L. Direct Imaging of single Au atoms within GaAs nanowires. *Nano. Lett.* **12,** 2352–2356 (2012).
13. Breuer, S. *et al.* Suitability of Au-and self-assisted GaAs nanowires for optoelectronic applications. *Nano. Lett.* **11,** 1276–1279 (2011).
14. Kelzenberg, M. D. *et al.* Enhanced absorption and carrier collection in Si wire arrays for photovoltaic applications. *Nat. Mater.* **9,** 239–244 (2010).
15. Wei, W. *et al.* Direct heteroepitaxy of vertical InAs nanowires on si substrates for broad band photovoltaics and photodetection. *Nano. Lett.* **9,** 2926–2934 (2009).
16. Fontcuberta i Morral, A., Colombo, C., Abstreiter, G., Arbiol, J. & Morante, J. R. Nucleation mechanism of gallium-assisted molecular beam epitaxy growth of gallium arsenide nanowires. *Appl. Phys. Lett.* **92,** 063112 (2008).
17. Colombo, C., Heiβ, M., Gratzel, M. & Fontcuberta i Morral, A. Gallium arsenide p-i-n radial structures for photovoltaic applications.. *Appl. Phys. Lett.* **94,** 173108 (2009).
18. Gutsche, C. *et al.* n-GaAs/InGaP/p-GaAs core-multishell nanowire diodes for efficient light-to-current conversion. *Adv. Funct. Mater.* **22,** 929–936 (2011).
19. Kempa, T. J. *et al.* Coaxial multishell nanowires with high-quality electronic interfaces and tunable optical cavities for ultrathin photovoltaics. *Proc. Natl Acad. Sci. USA* **109,** 1407–1412 (2012).
20. Shockley, W. & Queisser, H. J. Detailed balance limit of efficiency of p-n junction solar cells. *J. Appl. Phys.* **32,** 510–519 (1961).
21. Heiss, M. & Fontcuberta i Morral, A. Fundamental limits in the external quantum efficiency of single nanowire solar cells. *Appl. Phys. Lett.* **99,** 263102 (2011).
22. Yu, S., Roemer, F. & Witzigmann, B. Analysis of surface recombination in nanowire array solar cells. *Proc. SPIE 8438, Photonics for Solar Energy Systems IV*. (eds Wehrspohn, R. & Gombert, A.) 84380O (International Society of Optics and Photonics, 2012).
23. Plissard, S., Larrieu, G., Wallart, X. & Caroff, P. High yield of self-catalyzed GaAs nanowire arrays grown on silicon via gallium droplet positioning. *Nanotechnology* **22,** 275602 (2011).
24. Goto, H. *et al.* growth of core–shell InP nanowires for photovoltaic application by selective-area metal organic vapor phase epitaxy. *Appl, Phys, Express,* **2,** 035004 (2009).

Acknowledgements

This work has been supported by the Danish National Advanced Technology Foundation through project 022-2009-1, by the EU through FP7-SME programme support to project PolyGlass, a University of Copenhagen Centre of Excellence and by the UNIK Synthetic Biology project. We thank Dr Ray LaPierre (McMaster University) for fruitful discussions, Dr Erik Johnson (University of Copenhagen) for assistance with transmission electron microscopy characterization and Kevin Lee (University College London) for assisting with MBE growths.

Author contributions

H.L. and M.A. performed material growth. H.I.J., J.V.H., H.L., M.A. and P.K. assisted with growth development and characterization. H.I.J., J.V.H. and M.A. collaborated on device design, fabrication, measurement and assessment. J.N. supervised P.K. and participated in discussions throughout the work. All the authors contributed to preparation of the manuscript.

Additional information

Supplementary Information accompanies this paper on http://www.nature.com/naturecommunications

Competing financial interests: The authors declare no competing financial interests.

Reprints and permission information is available online at http://npg.nature.com/reprintsandpermissions/

How to cite this article: Holm, J.V. *et al.* Surface-passivated GaAsP single-nanowire solar cells exceeding 10% efficiency grown on silicon. *Nat. Commun.* 4:1498 doi: 10.1038/ncomms2510 (2013).

Supplementary information for:

Surface passivated GaAsP single-nanowire solar cells exceeding 10% efficiency grown on silicon

Jeppe V. Holm[1†], Henrik I. Jørgensen[1†], Peter Krogstrup[2], Jesper Nygård[2,4], Huiyun Liu[3] and Martin Aagesen[1†*]

[1]SunFlake A/S, Universitetsparken 5, DK-2100 Copenhagen, Denmark,
[2]Nano-Science Center, Niels Bohr Institute, University of Copenhagen, Universitetsparken 5, DK-2100 Copenhagen, Denmark,
[3]Department of Electronic and Electrical Engineering, University College London, London WC1E 7JE, UK,
[4]Center for Quantum Devices, Niels Bohr Institute, University of Copenhagen, Universitetsparken 5, DK-2100 Copenhagen, Denmark.

†These authors contributed equally to this work

*e-mail: martin.aagesen@sunflake.dk

The supplement includes more details on:

1. Nanowire core growth
2. Ideality factor, series and shunt resistance

Supplementary Figures

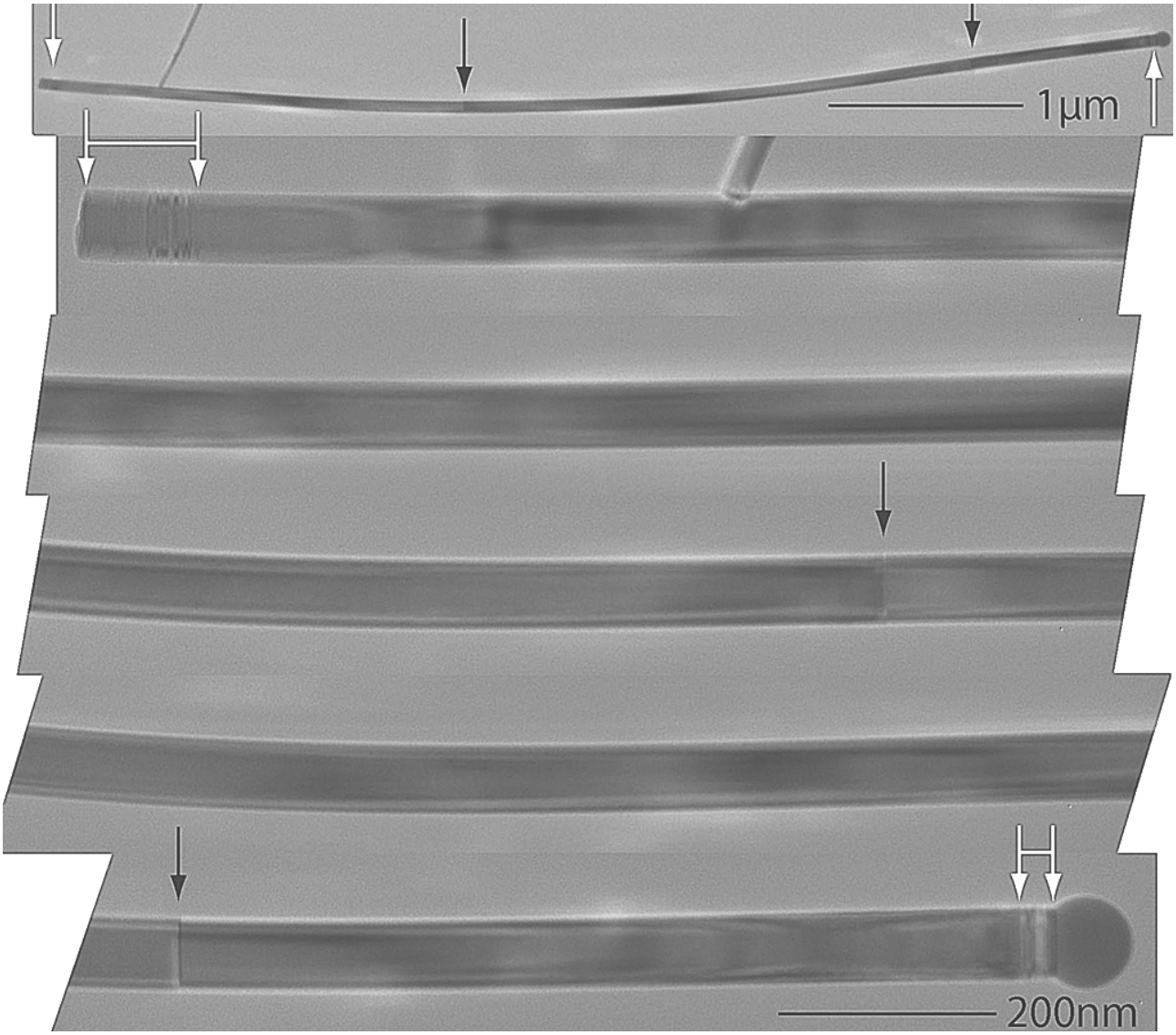

Supplementary Figure S1. TEM image showing the full nanowire from Figure 1b and higher resolution images of sections of the same wire. The crystal structure is almost phase perfect except from a few single twins along the nanowire which are indicated by black arrows. At the bottom and top part of the nanowire larger sections with multiple twins are present, as indicated by white arrows. The almost perfect middle section shows that it is possible, by adjusting the growth parameters, to essentially eliminate twinning in the GaAsP nanowires.

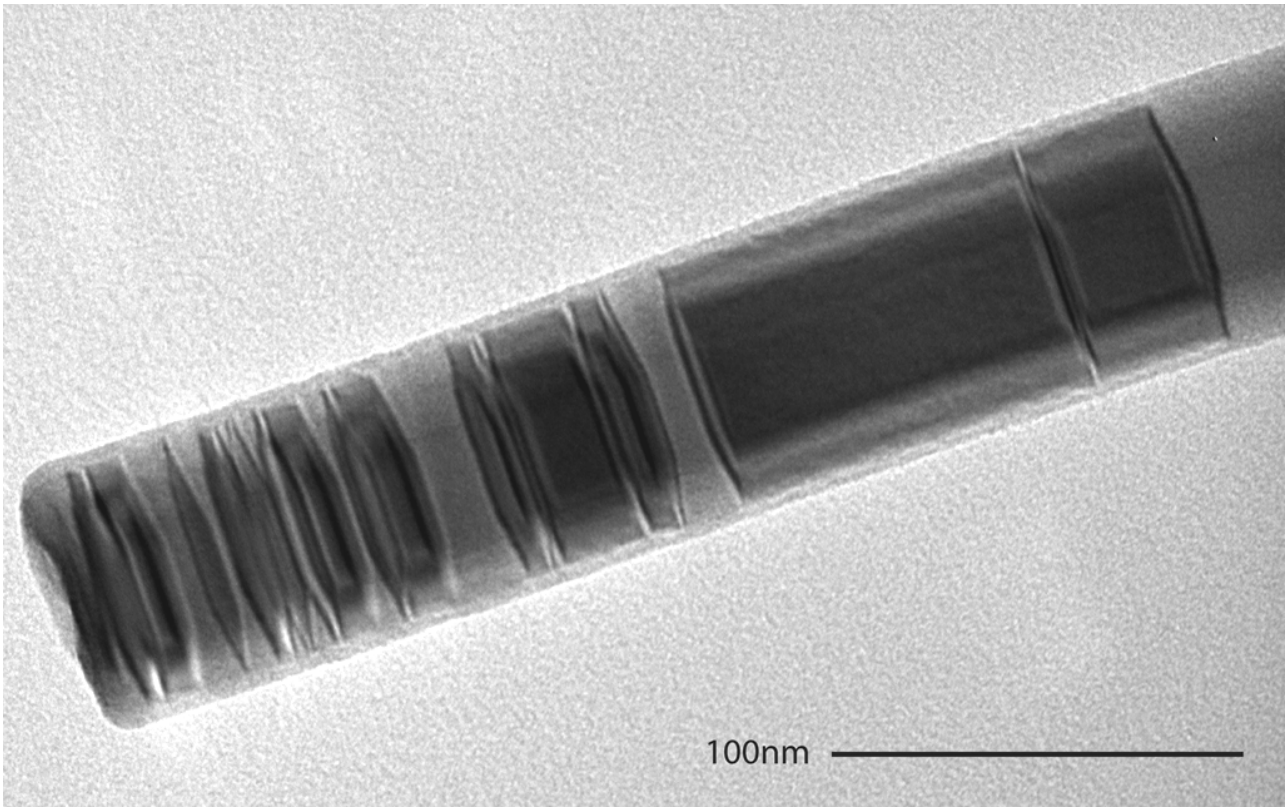

Supplementary Figure S2. A TEM image of a bottom nanowire section. During the first part of the nanowire growth, large sections of single twins or würtzite crystal segments form. Since the nanowire is tilted slightly the hexagonal shape of the nanowire can be seen in the twin segments. The twinnings are not caused by strain from the difference in lattice constants between the GaAsP and the Si, but are due to the different growth conditions during this part of the nanowire growth. By adjusting the growth parameters correctly it should hence be possible to eliminate the twinning entirely.

Supplementary Figure S3. Diffraction image from core only GaAsP. The diffraction spots are a signature of the face centred cubic crystal structure when viewed in the [011] zone axis. Since there are two atoms in the brillouin zone (Ga and As/P) it is a zinc-blende signature. The image is obtained when looking at the middle section of a nanowire. At the top and bottom of the nanowires, some of the spots may have additional mirror spots as a signature of one or more twins. At areas with multiple twins close to each other streaks between the main spots begin to develop. No other type of diffraction pattern has been found, indicating that the wires have 6 equivalent [011] side facets.

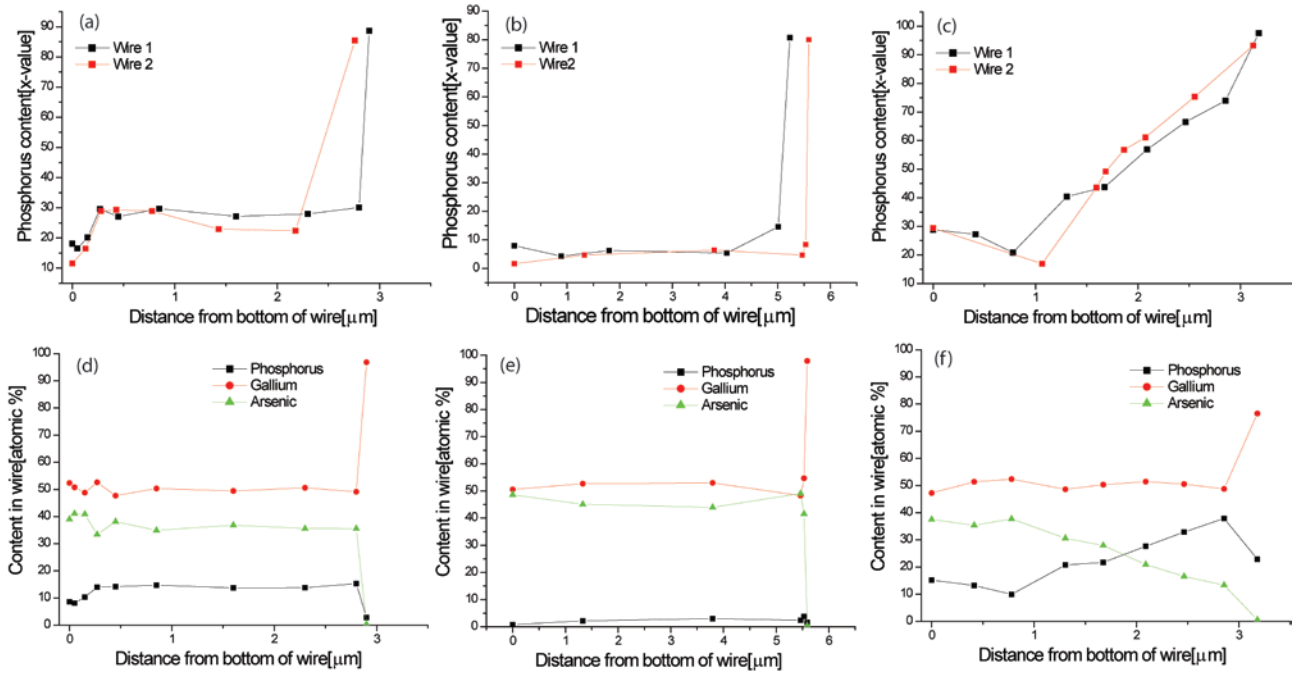

Supplementary Figure S4. EDX of core only $GaAs_{1-x}P_x$ nanowires. a, b and c, Phosphorus content [*x*] of two nanowires from three different nanowire growths. The sudden change in P content at the highest point is measured at the very top of the nanowire. It should be noted that the content of group V in the liquid is generally very low (see Supplementary Figure S4d,e,f), which implies a high uncertainty in the Group V mole fractions. **a,** A growth where the P content was within the intended range *x* ~0.25. **b,** A growth where the P content was lower than required *x* ~0.5-0.10. **c,** A growth where the P content was deliberately changed from low (0.15) to high (0.70) during the growth. **d, e and f,** The atomic content of one of the wires from respectively the a, b and c panels. The top data point shows that the catalyst particle is mostly gallium. Since these are raw data the gallium content is not displayed as exactly 50%.

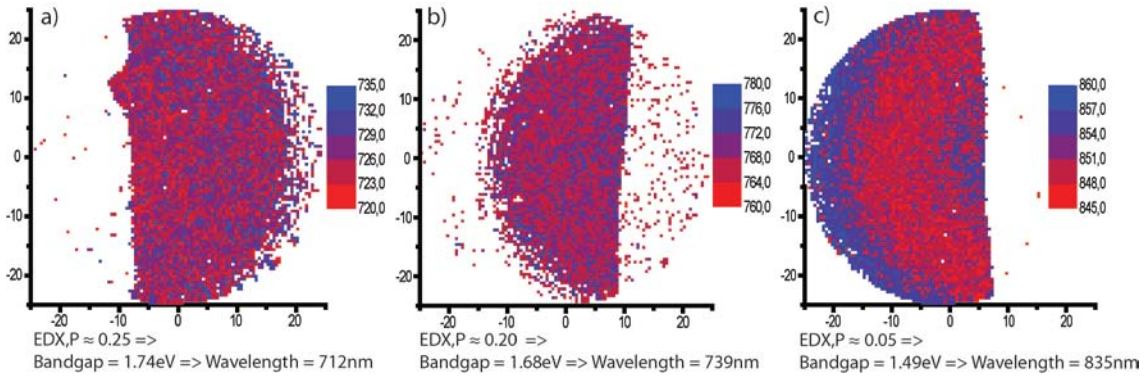

Supplementary Figure S5. The emitted wavelength from room temperature photo luminescence measurements of core only $GaAs_{1-x}P_x$ nanowires standing on half 3" growth substrates. a, same growth as Supplementary Figure S4a. **b,** same growth as Figure 1c in the main paper **c,** same growth as Supplementary Figure S4b. Every pixel represents a 0.5 x 0.5 mm square of substrate and thousands of nanowires. The axes indicate scan distance [mm]. Note that the wavelength scale is different in each panel. Below each plot is written the approximate phosphor content which was extracted from the EDX measurements, and the calculated bandgap and equivalent wavelength[25]. Comparing the measured wavelengths to the EDX derived ones, we observe that the EDX and PL qualitatively agree, but that wavelengths calculated from the EDX are slightly below the wavelength of the emitted light. A small variation in bandgap is observed across the substrate in Supplementary Figure S5c. This is the result of a small temperature gradient across the substrate during nanowire growth and growth initiation. The temperature gradient results in a variation in nanowire density and because the P and As diffusion lengths are different this leads to the observed variation in bandgap. Using positioned growth and improved substrate temperature calibration this bandgap variation should be removed.

Supplementary Discussion

Nanowire core growth

For vapor-liquid-solid (VLS) growth of Ga-assisted nanowires the morphology of the liquid-solid growth region plays an important role on the relative crystal structure formation probabilities[26]. Thus, having a correct V/III ratio is crucial for obtaining perfect zinc-blende nanowire crystals. Since the effective V/III ratio at the growth region changes throughout the nanowire growth[7] it is important to counteract this by being able to adjust the external group V and III fluxes accordingly. The Ga-assisted axial nanowire core growth can be divided into 3 growth stages, 1) The initial growth stage: formation of a stable liquid-solid growth mode takes typically a few hundred nm of growth; 2) quasi steady-state growth of the main part of the nanowire; and 3) the final growth stage where the droplet is consumed by nucleation from the supersaturated Ga droplet either a) during cooling after nanowire growth or b) when growing without a Ga flux. By adjusting the As and P fluxes during part 2 we have been able to obtain essentially a perfect single crystal zinc-blende structure. Twinnings at the lower section of the nanowire, away from the main photon absorption areas, and at the top of the nanowire have not yet been attempted removed. The crystal quality, material composition and bandgap of the nanowires grown, were probed using transmission electron microscopy (TEM), room temperature photo-luminescence (PL) and energy dispersive x-ray spectroscopy (EDX). Selected data from different core nanowire growths are shown in Supplementary Figures S1, S2, S3, S4 and S5.

Ideality factor, series and shunt resistance

We extract the ideality factor, series resistance and shunt resistance by fitting the current-voltage curves to a simple model schematically shown below. It consists of a diode with ideality factor η, photo current I_{ph} and a series and shunt resistor (R_{Se}, and R_{Sh}). The source-drain current (I_{Sd}) versus source-drain voltage (V_{Sd}) can be found via a parameterization of the diode voltage (V_d) using the following three equations:

$$I_d(V_d) = I_0\left(\exp\left(\frac{eV_d}{\eta k_B T}\right) - 1\right) - I_{ph}$$

$$I_{sd}(V_d) = \frac{V_d}{R_{Sh}} + I_d(V_d)$$

$$V_{sd}(V_d) = R_{Se}\left(\frac{V_d}{R_{Sh}} + I_d(V_d)\right) + V_d$$

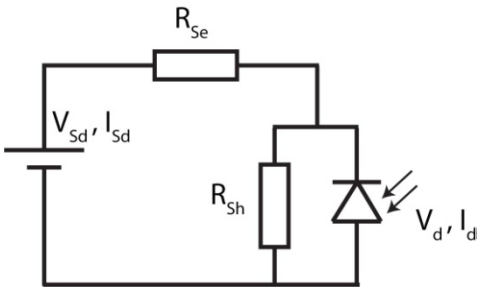

Figure 3a, b shows fits (solid lines) to the measured IV curves in the dark (blue circles), and illuminated by global AM1.5 light (red circles). We hereby extract for the passivated (unpassivated) device an ideality factor of about 2.0 (2.2), and series resistances of 70MΩ (10MΩ). The shunt resistance depends on the light intensity; under dark conditions it is >100GΩ for both devices.

Supplementary References

25. Vurgaftman, I., Meyer, J. R. & Ram-Mohan, L. R. Band parameters for III–V compound semiconductors and their alloys. *Journal of Applied Physics* **89**, 5815–5875 (2001).

26. Krogstrup, P. *et al.* Impact of the Liquid Phase Shape on the Structure of III-V Nanowires. *Phys. Rev. Lett.* **106**, 125505 (2011).

II: Single-nanowire solar cells beyond the Shockley–Queisser limit

Peter Krogstrup*, Henrik Ingerslev Jørgensen*, Martin Heiss*, Olivier Demichel, **Jeppe V. Holm**, Martin Aagesen, Jesper Nygard & Anna Fontcuberta i Morral

Reprinted with permission from Nature Publishing Group. First published as: *Nature Photonics*, **7**, 306-310 (2013)

ARTICLES
PUBLISHED ONLINE: 24 MARCH 2013 | DOI: 10.1038/NPHOTON.2013.32
nature photonics

Single-nanowire solar cells beyond the Shockley–Queisser limit

Peter Krogstrup[1†*], Henrik Ingerslev Jørgensen[2†], Martin Heiss[3†], Olivier Demichel[3], Jeppe V. Holm[2], Martin Aagesen[2], Jesper Nygard[1] and Anna Fontcuberta i Morral[3*]

Light management is of great importance in photovoltaic cells, as it determines the fraction of incident light entering the device. An optimal p–n junction combined with optimal light absorption can lead to a solar cell efficiency above the Shockley–Queisser limit. Here, we show how this is possible by studying photocurrent generation for a single core–shell p–i–n junction GaAs nanowire solar cell grown on a silicon substrate. At 1 sun illumination, a short-circuit current of 180 mA cm^{-2} is obtained, which is more than one order of magnitude higher than that predicted from the Lambert–Beer law. The enhanced light absorption is shown to be due to a light-concentrating property of the standing nanowire, as shown by photocurrent maps of the device. The results imply new limits for the maximum efficiency obtainable with III–V based nanowire solar cells under 1 sun illumination.

Nanowire-based solar cells hold great promise for third-generation photovoltaics and for powering nanoscale devices[1,2]. With the advent of third-generation photovoltaics, solar cells will become cheaper and more efficient than current devices. In particular, a cost reduction may be achieved by reducing material use through the fabrication of nanowire arrays and radial p–n junctions[3–5]. The geometry of nanowire crystals is expected to favour elastic strain relaxation, providing great freedom in the design of new compositional multijunction solar cells[6] grown on mismatched materials[7,8]. The efficiencies of nanostructured solar cells have increased over time and have now reached up to 13.8%, due to improvements in materials and new device concepts[9–14].

Light absorption in standing nanowires is a complex phenomenon, with a strong dependence on nanowire dimensions and the absorption coefficient of the raw materials[15–18]. In low-absorbing microwire arrays, such as those composed of silicon, light absorption is understood via ray optics or by calculation of the integrated local density of optical states of the nanowire film[19,20]. Interestingly, when these arrays stand on a Lambertian back-reflector, an asymptotic increase in light trapping for low filling factors (FFs) is predicted[19]. This is advantageous for improvement of the efficiency-to-cost ratio of solar cells and has led to the demonstration of microwire arrays exhibiting higher absorption than in the equivalent thickness of textured film[19,21,22]. The case for nanowires is quite different. Nanowire diameters are smaller than or comparable to the radiation wavelength. In this case, optical interference and guiding effects play a dominant role in relation to reflectivity and absorption spectra. For low-absorbing materials (for example, indirect bandgap materials such as silicon), waveguiding effects plays a key role[23,24], whereas highly absorbing semiconductors (such as direct-bandgap GaAs) exhibit resonances that increase the total absorption several times. Nanowires lying on a substrate also exhibit such resonances, often described by Mie theory[25,26], although the total absorption rate is significantly lower[27,28]. Even though the optical absorption of nanowires arranged in an array has been shown to be far more complex than in thin films, nanowire vertical arrays currently seem to be the most reasonable device proposal. One elegant device consists of a single standing nanowire solar cell, contacted on top by a transparent electrode and at the bottom through the substrate. Although the characterization of single nanowires lying on a substrate is quite common, to date there have been no studies on single standing nanowires.

In this Article, we present experimental measurements on single GaAs nanowire solar cells, as grown on a silicon substrate, where the p-section is contacted through a highly doped substrate and the n-section through a transparent top contact (Fig. 1a–c)[26]. We find that light absorption in single standing nanowires is more than one order of magnitude more efficient than is predicted from the Lambert–Beer law. We show measurements on two devices. The first device (Fig. 1) exhibits a short-circuit current density of 180 mA cm^{-2} when normalized to the projected area. This leads to an apparent solar conversion efficiency of 40%. The second device shows a short-circuit current of 173 mA cm^{-2} and an apparent efficiency of 28%. The reason for these very high efficiencies is the mismatch between the absorption cross-section and the physical bounds of the nanowires, hinting at a very large absorption cross-section. This work represents a critical step towards the next generation of nanowire-based solar cells.

The current–voltage characteristics of the devices were measured in the dark and under AM 1.5G illumination. The experimental data for device 1 are shown in Fig. 1d. In the dark, the device exhibits typical diode behaviour, with an ideality factor of 2.6. Under illumination, the diode curve is shifted downwards as a consequence of photogeneration and separation of electron–hole pairs, giving a short-circuit current of 256 pA. The diameter of the nanowire is 425 nm, corresponding to an apparent photogenerated current density of 180 mA cm^{-2}. The open-circuit voltage V_{OC} and FF are 0.43 V and 0.52, respectively, both of which should be improved by optimizing the resistivity, the thickness of the doped layers and surface passivation[29]. The generated power at the maximum power point is 57 pW, corresponding to 40 mW cm^{-2}. Dividing the generated power density by the incident power density, the

[1]Center for Quantum Devices, Nano-Science Center, Niels Bohr Institute, University of Copenhagen, Universitetsparken 5, DK-2100 Copenhagen, Denmark, [2]SunFlake A/S, Nano-Science Center, Universitetsparken 5, DK-2100 Copenhagen, Denmark, [3]Laboratoire des Matériaux Semiconducteurs, Ecole Polytechnique Fédérale de Lausanne, 1015 Lausanne, Switzerland; †These authors contributed equally to this work. *e-mail: anna.fontcuberta-morral@epfl.ch; krogstrup@fys.ku.dk

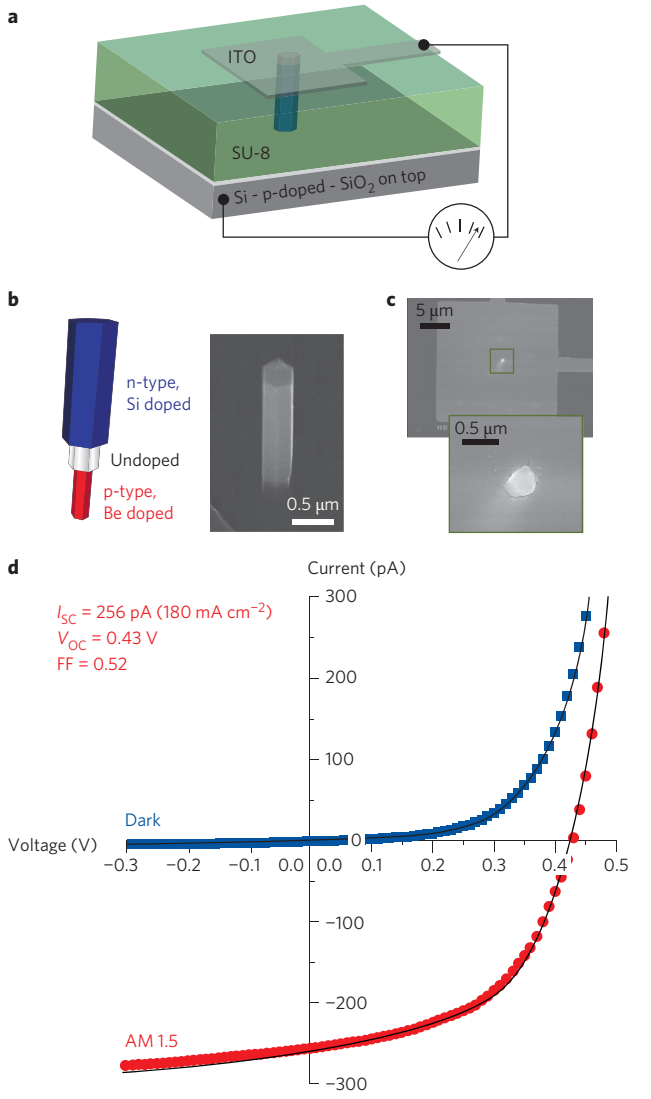

Figure 1 | Electrical characterization of a single nanowire solar cell (device 1). **a**, Schematic of the vertical single-nanowire radial p–i–n device connected to a p-type doped silicon wafer by epitaxial growth. **b**, Left: doping structure of the nanowire. The p-type doped core is in contact with the doped silicon substrate and the n-type doped shell is in contact with the ITO. Right: Scanning electron microscope (SEM) image of a nanowire solar cell before adding the top contact, with a 30° angle from the vertical. **c**, SEM images of the device seen from the top electrode. The nanowire is ~2.5 μm high and has a diameter of ~425 nm. **d**, Current–voltage characteristics of the device in the dark and under AM 1.5G illumination, showing the figure-of-merit characteristics.

solar cell yields an apparent efficiency of 40%. To understand the extreme photon collection boost in free-standing single GaAs nanowires, we used a finite-difference time-domain (FDTD) method to model a 2.5-μm-long nanowire embedded in SU-8 as a function of its diameter and of the wavelength of the plane-wave radiation propagating along the nanowire axis[30–32]. Figure 2a shows the wavelength and diameter dependence of the absorption rate of such a nanowire. Note that the absorption is zero for wavelengths larger than 900 nm where the absorption coefficient of GaAs goes to zero. Two dominant branches for low and high diameters are observed, corresponding to resonances similar to the Mie resonances observed in nanowires lying on a substrate[25]. Light absorption in the standing nanowire is enhanced by a factor of between 10 and 70 with respect to the equivalent thin film. Another way to express this enhancement in absorption is through the concept of an absorption cross-section. The absorption cross-section is defined as $A_{abs} = a\eta$, where a is the physical cross-section of the nanowire and η is the absorption efficiency. It is largely accepted that the absorption cross-section in nanoscale materials is larger than their physical size. In systems such as quantum dots, the absorption cross-section can exceed the physical size by a factor of up to 8 (ref. 33). We calculated the absorption cross-section of the nanowires as a function of the nanowire diameter and incident wavelength (Fig. 2b). The absorption cross-section is, in all cases, larger than the physical cross-section of the nanowire. It is interesting to note that the absorption of photons from an area larger than the nanowire itself is equivalent to a built-in light concentration C. Light concentration has an additional benefit in that it increases the open-circuit voltage with a term $kT \ln C$, thereby increasing the efficiency[34–36]. The largest absorption cross-section in Fig. 2b is 1.13×10^6 nm^2 for a nanowire diameter of 380 nm ($a = 9.38 \times 10^4$ nm^2), corresponding to an overall built-in light concentration of ~12.

Measurements of the external quantum efficiency (EQE) normalized by the physical area for both lying and standing nanowire devices are shown in Fig. 3a (see Supplementary Section S1 for

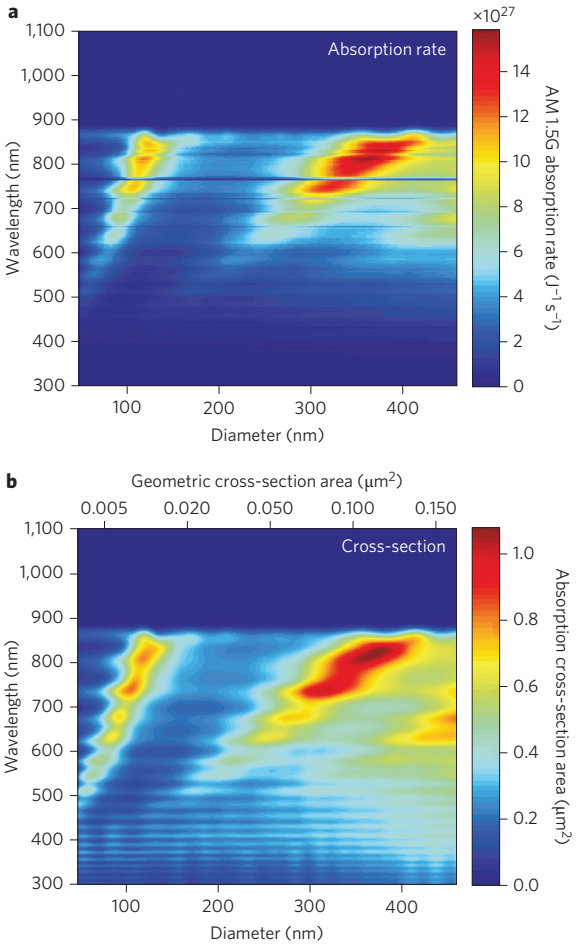

Figure 2 | Optical simulations of a single nanowire solar cell. **a**,**b**, Simulations of light absorption in a 2.5 μm standing GaAs nanowire that is fully embedded in SU-8 ($n = 1.67$) on a silicon substrate: the absorption rate of solar AM 1.5G radiation (**a**) and simulated absorption cross-section (**b**) exhibit two main resonant branches, similar to Mie resonances observed in nanowires lying on a substrate. The periodic modulation with wavelength is a result of Fabry–Pérot interference in the polymer layer and not an artefact of the simulation.

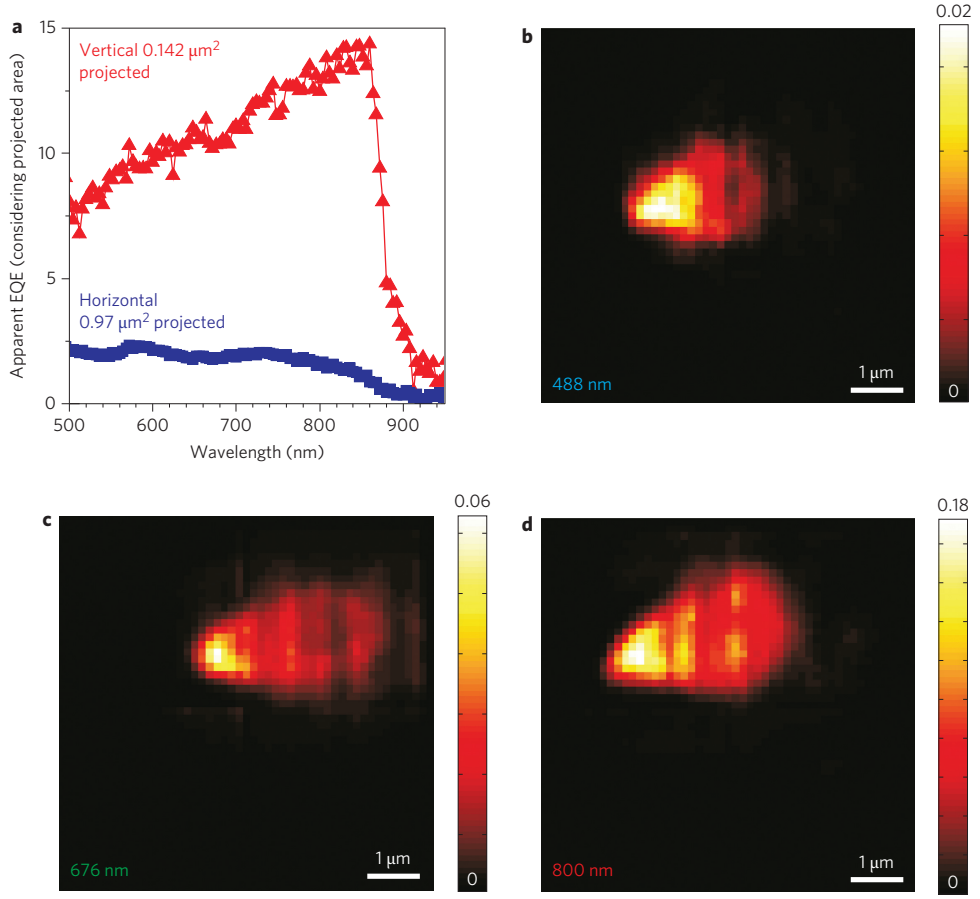

Figure 3 | Optical characterization of a single nanowire solar cell (device 2). a, EQE normalized by indicated projected area, comparing vertical and horizontal nanowire solar cells. For the vertical standing solar cell, a 15-fold increase in photon collection is obtained close to the bandgap. EQE becomes negligible for photon wavelengths below the bandgap of GaAs, meaning that there is no contribution from absorption in the silicon substrate[45]. **b–d**, Scanning photocurrent measurements on our single vertical nanowire device for three different excitation laser wavelengths, normalized to the incident photon flux. Scale bar, 1 μm.

more details). Lying nanowires exhibit EQE values up to 2 due to Mie resonances[37], while for standing nanowires values of up to ~14.5 are reached. This further confirms that the absorption cross-section is several times larger than the apparent cross-section of the wire, especially at wavelengths close to the bandgap.

To further understand the absorption boost in our devices, we spatially mapped the photocurrent generated by a vertical nanowire device for three different excitation wavelengths: 488 nm, 676 nm and 800 nm. The results presented in Fig. 3b–d are deconvoluted with the point-spread function of the diffraction-limited laser spot. As seen in the figure, a photocurrent from an area much larger than the size of the laser spot appears for all three wavelengths. A fit to the data allows the estimation of an effective absorption cross-section diameter of 1.2 μm (488 nm), 1.0 μm (676 nm) and 1.3 μm (800 nm), respectively. Hence, the absorption boost in our device is due to an unexpectedly large absorption cross-section of the vertical nanowire geometry. This is equivalent to a built-in light concentration of ~8, which is in good agreement with our theoretical predictions. In addition, we speculate that the top-contact geometry further contributes to the resonant absorption effect, thereby increasing the absorption cross-section and the boost in photogenerated current.

Finally, we put our results into perspective by comparing them to the best existing technologies and to the design principles for increasing efficiency. In Table 1 we list the best values for leading technologies such as single-junction crystalline silicon (c-Si) and GaAs, as well as triple-junction devices. The highest efficiency is provided by the triple-junction solar cell (34.1%), with a short-circuit current of 14.7 mA cm^{-2}. In this case the short-circuit current is kept relatively low as it has to be matched between the three cells connected in series, and it is the high efficiency that generates the increase in V_{OC}. The highest short-circuit current is obtained in the c-Si solar cell, where light management techniques result in a boost in the photogenerated current of 42.7 mA cm^{-2}. The record efficiency recorded by Alta Devices with GaAs was obtained with a relatively thin film (a few micrometres, rather than a few hundred micrometres as in standard cells). This brings us to the discussion of what determines high efficiency. A solar cell operates at a voltage that maximizes the generated power, dictated by the short-circuit current, FF and V_{OC}. Designing with a view to achieving higher efficiencies requires strategies for increasing these values[38,39]. Improving the first two parameters – short-circuit current and FF – mainly involves device 'engineering', while obtaining the ultimate V_{OC} is dictated by the thermodynamics of solar energy conversion into electrical work. Within the Shockley–Queisser model, V_{OC} is limited as follows[36]:

$$V_{oc} = \frac{E_g}{q}\left(1 - \frac{T}{T_{sun}}\right) - \frac{kT}{q}\left(\ln\frac{\Omega_{emit}}{\Omega_{sun}} + \ln\frac{4n^2}{C} - \ln QE\right)$$

where T and T_{sun} are the temperatures of the cell and the sun, respectively, Ω_{emit} and Ω_{sun} correspond to the solid angle of

Table 1 | J_{SC}, FF, V_{OC}, area and efficiency of the best photovoltaic technologies compared with the standing nanowire configuration presented in this work.

Technology	J_{SC} (mA cm^{-2})	FF (%)	V_{OC} (V)	Area (cm^2)	η (%)
c-Si	42.7	82.8 (ref. 47)	0.706	4	25.0
GaAs	29.68	86.5	1.122	1	28.8 (ref. 48)
Triple junction	14.57	86.0	3.014	30	37.7
This work	180	52	0.43	1.42×10^{-9}	40*

The low V_{OC} and FF values indicate the potential for improvement of the nanowire cell presented. See main text for discussion.
*Apparent efficiency calculated with the projected area of the cell.

emission and collection, n is the refractive index of the material, and QE is the emission quantum efficiency. The first term is related to the Carnot efficiency, which reduces V_{OC} by ~5%. The second term corresponds to the entropic losses occurring during work generation. The first entropy loss is due to non-reciprocity in the angle of light absorption and emission. Light-resonant structures such as nanowires can reduce the contribution of this term[36]. The second entropy loss takes account of the concentration factor, given by the refractive index and any external concentration: V_{OC} increases by implementing light-trapping strategies, with the additional benefit of increasing absorption close to the bandgap[40,41]. The last entropic term refers to non-radiative losses. It can be reduced to zero by increasing QE to 1. The impressive result for GaAs cells achieved by Alta Devices was obtained thanks to increasing the QE in a GaAs thin film to 1. Our results provide a further path for higher-efficiency solar cells. Even though the electrical characteristics shown are not yet ideal, we observe a light concentration effect plus a significant increase in absorption rate close to the bandgap, similar to that proposed in ref. 36. These two effects are such that nanowire structures can reduce the entropy in the conversion of solar energy into electrical work, thereby providing a path for increasing the efficiency of solar cells. It is also important to note that the unexpected increase in the absorption cross-section enables nanowires to be further separated from one another, resulting in major cost reductions for the final device. Our experiments indicate that a good interwire distance would be ~1.2 μm. A nanowire solar cell consisting of nanowires similar to the device shown in Fig. 1, positioned in a hexagonal array with a pitch of 1 μm (optical cross-section with a diameter of ~1.2 μm), would have an optical FF of 1, and it would only use a material volume equivalent to that of a 546 nm film and exhibit a conversion efficiency of 4.6%. By using devices with a smaller area (see left branch in Fig. 2a,b), one could further reduce the amount of material used by a factor of up to 72. By improving the electrical characteristics of the p–n junction, higher efficiencies could be obtained. By considering an effective light concentration of only 15, an array of GaAs nanowires with ideal characteristics would exhibit an efficiency of 33.4%, thereby overcoming the Shockley–Queisser limit for planar GaAs solar cells illuminated by 1.5 AM radiation, according to the discussion presented in the foregoing text[34,42]. Even higher efficiencies could be achieved if the device design were tailored for higher light concentrations and QE. Note that axial junctions, which have the same junction area as the projected area, would obtain the full benefit from such a concentrator effect, and it would be possible to directly compare the performance of GaAs nanowire solar cells under 1 sun with planar GaAs cells under 10 suns. We demonstrate here that single-nanowire devices generate several-fold higher power than their projected areas suggest when they are standing upright, a configuration that also minimizes their footprint. It should be noted that if one were to build a single-nanowire solar cell, then a flat-lying nanowire would exhibit ~15 times lower power density compared to the standing nanowire device due to the light concentration effect. This enhancement in energy conversion at the nanoscale will make standing nanowires useful as energy harvesters, with minimum footprint, for feeding other devices on the same chip. This is already the case for nanowire-based p–n junctions with non-ideal characteristics such as the one demonstrated in this work. Last, but not least, the improvement in photon collection renders them (in general) ideal for use as photodetectors.

In conclusion, we have observed a remarkable boost in absorption in single-nanowire solar cells that is related to the vertical configuration of the nanowires and to a resonant increase in the absorption cross-section. These results open a new route to third-generation solar cells, local energy harvesters on nanoscale devices and photon detectors.

Methods

Nanowire growth. Nanowires were grown on oxidized Si(111) with 100 nm apertures using a self-catalysed method. The gallium nominal growth rate was 900 nm h^{-1}, the substrate temperature was 630 °C and the V/III ratio was 4 (refs 43,44). The p-doping of the core was achieved by adding a flux of beryllium during axial growth[45]. Cores were annealed for 10 min at 630 °C. The shell was obtained at 465 °C, a growth rate of 300 nm h^{-1} and with a V/III ratio of 50. The n-type doping was obtained by adding silicon to the growth step[46].

Device fabrication and characterization. SU-8 was spun onto the substrate at 4,000 r.p.m. for 45 s and cured with 1 min ultraviolet light and 3 min on a hotplate at 185 °C. An etch-back with a 1–3 min oxygen plasma etch was then performed to free the nanowire tip. The top contact was defined by electron-beam lithography followed by evaporation of indium tin oxide (ITO) (for more details see Supplementary Section S1). The bottom contact was obtained by silver gluing to the back-side of the wafer. Current–voltage characteristics were measured in the dark and under 1.5 G conditions with a standard solar simulator (LOT – Oriel 150 W xenon lamp) with a 1-inch beam diameter and an AM 1.5G filter. A photocurrent map of the devices was collected by scanning the contacted sample under the laser spot focused with a ×63 and 0.75 NA lens.

FDTD method simulations. The absorption of standing 2.5 μm GaAs nanowires of different diameters, standing on silicon and surrounded by SU-8, was calculated by solving Maxwell equations in three dimensions for an incident plane-wave radiation normal to the substrate. The wave equation was solved in the time domain according to refs 30 and 27.

Received 6 November 2012; accepted 28 January 2013; published online 24 March 2013

References

1. Tian, B. Z. *et al.* Coaxial silicon nanowires as solar cells and nanoelectronic power sources. *Nature* **449,** 885–888 (2007).
2. Law, M., Greene, L. E., Johnson, J. C., Saykally, R. & Yang, P. D. Nanowire dye-sensitized solar cells. *Nature Mater.* **4,** 455–459 (2005).
3. Kayes, B. M., Atwater, H. A. & Lewis, N. S. Comparison of the device physics principles of planar and radial *p–n* junction nanorod solar cells. *J. Appl. Phys.* **97,** 114302 (2005).
4. Spurgeon, J. M. *et al.* Flexible, polymer-supported, Si wire array photoelectrodes. *Adv. Mater.* **22,** 3277–3281 (2010).
5. Fan, Z. *et al.* Three-dimensional nanopillar-array photovoltaics on low-cost and flexible substrates. *Nature Mater.* **8,** 648–653 (2009).
6. Kempa, T. J. *et al.* Single and tandem axial *p–i–n* nanowire photovoltaic devices. *Nano Lett.* **8,** 3456–3460 (2008).
7. Chuang, L. C. *et al.* Critical diameter for III–V nanowires grown on lattice-mismatched substrates. *Appl. Phys. Lett.* **90,** 043115 (2007).
8. Glas, F. Critical dimensions for the plastic relaxation of strained axial heterostructures in free-standing nanowires. *Phys. Rev. B* **74,** 121302 (2006).
9. Tsakalakos, L. *et al.* Silicon nanowire solar cells. *Appl. Phys. Lett.* **91,** 233117 (2007).
10. Goto, H. *et al.* Growth of core–shell InP nanowires for photovoltaic application by selective-area metal organic vapor phase epitaxy. *Appl. Phys. Express* **2,** 035004 (2009).

11. Garnett, E. C. & Yang, P. Silicon nanowire radial p–n junction solar cells. *J. Am. Chem. Soc.* **130,** 9224–9225 (2008).
12. Wallentin, J. *et al.* InP nanowire array solar cells achieving 13.8% efficiency by exceeding the ray optics limit. *Science* **339,** 1057–1060 (2013).
13. Tian, B. Z. & Lieber, C. M. Design, synthesis, and characterization of novel nanowire structures for photovoltaics and intracellular probes. *Pure Appl. Chem.* **83,** 2153–2169 (2011).
14. Dalmau-Mallorqui, A., Epple, F. M., Fan, D., Demichel, O. & Fontcuberta i Morral, A. Effect of the *pn* junction engineering on Si microwire-array solar cells. *Phys. Status Solidi* **209,** 1588–1591 (2012).
15. Tsakalakos, L. *et al.* Strong broadband optical absorption in silicon nanowire films. *J. Nanophot.* **1,** 013552 (2007).
16. Zhu, J. *et al.* Optical absorption enhancement in amorphous silicon nanowire and nanocone arrays. *Nano Lett.* **9,** 279–282 (2009).
17. Mariani, G. *et al.* Patterned radial GaAs nanopillar solar cells. *Nano Lett.* **11,** 2490–2494 (2011).
18. Muskens, O. L., Gomez-Rivas, J., Algra, R. E., Bakkers, E. P. A. M. & Lagendijk, A. Design of light scattering in nanowire materials for photovoltaic applications. *Nano Lett.* **8,** 2638–2642 (2008).
19. Kosten, E. D., Warren, E. L. & Atwater H. A. Ray optical light trapping in silicon microwires: exceeding the $2n^2$ intensity limit. *Opt. Express* **19,** 3316–3331 (2011).
20. Callahan, D. M., Munday, J. N. & Atwater H. A. Solar cell light trapping beyond the ray optic limit. *Nano Lett.* **12,** 214–218 (2012).
21. Kelzenberg, M. D. *et al.* Enhanced absorption and carrier collection in Si wire arrays for photovoltaic applications. *Nature Mater.* **9,** 239–244 (2010).
22. Diedenhofen, S. *et al.* Strong geometrical dependence of the absorption of light in arrays of semiconductor nanowires. *ACS Nano* **5,** 2316–2323 (2011).
23. Kwanyong, S. *et al.* Multicolored vertical silicon nanowires. *Nano Lett.* **11,** 1851–1856 (2011).
24. Van Vugt, L. L., Zhang, B., Piccione, B., Spector, A. A. & Agarwal, R. Size-dependent waveguide dispersion in nanowire optical cavities: slowed light and dispersionless guiding. *Nano Lett.* **9,** 1684–1688 (2009).
25. Cao, L. *et al.* Engineering light absorption in semiconductor nanowire devices. *Nature Mater.* **8,** 643–647 (2009).
26. Brönstrup, G. *et al.* A precise optical determination of nanoscale diameters of semiconductor nanowires. *Nanotechnology* **22,** 385201 (2011).
27. Heiss, M. & Fontcuberta i Morral A. Fundamental limits in the external quantum efficiency of single nanowire solar cells. *Appl. Phys. Lett.* **99,** 263102 (2011).
28. Kempa, T. *et al.* Coaxial multishell nanowires with high-quality electronic interfaces and tunable optical cavities for ultrathin photovoltaics. *Proc. Natl Acad. Sci. USA* **109,** 1407–1412 (2011).
29. Nelson, J. *The Physics of Solar Cells* (Imperial College, 2003).
30. Oskooi, A. F. *et al.* MEEP: a flexible free-software package for electromagnetic simulations by the FDTD method. *Comp. Phys. Comm.* **181,** 687–702 (2010).
31. Kupec, J. & Witzigmann, B. Dispersion, wave propagation and efficiency analysis of nanowire solar cells. *Opt. Express* **17,** 10399–10410 (2009).
32. Cao, L. Y. *et al.* Semiconductor nanowire optical antenna solar absorbers. *Nano Lett.* **10,** 439–445 (2010).
33. Leatherdale, C. A., Woo, W. K., Mikulec, F. V. & Bawendi, M. G. On the absorption cross section of CdSe nanocrystal quantum dots. *J. Phys. Chem. B* **106,** 7619–7622 (2002).
34. Henry, C. H. Limiting efficiencies of ideal single and multiple energy gap terrestrial solar cells. *J. Appl. Phys.* **51,** 4494–4500 (1980).
35. Araújo, G. L. & Marti, A. Absolute limiting efficiencies for photovoltaic energy-conversion. *Solar Ener. Mater. Solar Cells* **33,** 213–240 (1994).
36. Polman, A. & Atwater H. A. Photonic design principles for ultrahigh-efficiency photovoltaics. *Nature Mater.* **11,** 174–177 (2012).
37. Kempa, T. *et al.* Coaxial multishell nanowires with high-quality electronic interfaces and tunable optical cavities for ultrathin photovoltaics. *Proc. Natl Acad. Sci. USA* **109,** 1407–1412 (2012).
38. Campbell, P. & Green, M. A. The limiting efficiency of silicon solar cells under concentrated sunlight. *IEEE Trans. Electron. Device Lett.* **33,** 234–239 (1986).
39. Nelson, J. *The Physics of Solar Cells* (Imperial College Press, 2003).
40. Luque, A. The confinement of light in solar cells. *Solar Ener. Mater.* **23,** 152–163 (1991).
41. Yablonovitch, E. & Cody, G. D. Intensity enhancement in textured optical sheets for solar cells. *IEEE Trans. Electron. Device Lett.* **29,** 300–305 (1982).
42. Shockley, W. & Queisser H. J. Detailed balance limit of efficiency of *p–n* junction solar cells. *J. Appl. Phys.* **32,** 510–519 (1961).
43. Uccelli, E. *et al.* Three-dimensional twinning of self-catalyzed GaAs nanowires on Si substrates. *Nano Lett.* **11,** 3827–3832 (2011).
44. Krogstrup, P. *et al.* Structural phase control in self-catalyzed growth of GaAs nanowires on silicon (111). *Nano Lett.* **10,** 4475–4482 (2010).
45. Casadei, A. *et al.* Doping incorporation paths in catalyst-free Be-doped GaAs nanowires. *Appl. Phys. Lett.* **102,** 013117 (2013).
46. Colombo, C., Heiß, M., Graetzel, M. & Fontcuberta i Morral, A. Gallium arsenide p–i–n radial structures for photovoltaic applications. *Appl. Phys. Lett.* **94,** 173108 (2009).
47. Zhao, J. *et al.* 19.8% efficient 'honeycomb' textured multicrystalline and 24.4% monocrystalline silicon solar cells. *Appl. Phys. Lett.* **73,** 1991–1993 (1998).
48. Green, M. A., Emery, K., Hishikawa, Y., Warta, W. & Dunlop, E. D. Solar cell efficiency tables (version 41). *Prog. Photovolt.* **21,** 1–11 (2013).

Acknowledgements

This research was funded by the ERC starting grant UpCon and by SNF (project nos 137648, 143908) and NCCR-QSIT. A.F.i.M. thanks STI for the 2011 end-of-year fund for MiBoots robots used in the scanning photocurrent experiment. A.F.i.M. and M.H. thank A. Dalmau-Mallorqui and F.M. Epple for experimental support. The authors also thank C.B. Sørensen and M.H. Madsen for assistance with MBE growth. This work was supported by the Danish National Advanced Technology Foundation (project 022-2009-1), a University of Copenhagen Center of Excellence, and by the UNIK Synthetic Biology project.

Author contributions

P.K. grew the nanowire p–n junctions. H.I.J. performed *I–V* characterization and fabricated the device, with help from J.V.H. and M.A. M.H. and O.D. performed the FDTD calculations. M.H. realized the photocurrent mappings and the external quantum efficiency measurements. A.F.i.M. and P.K. conceived and designed the experiments. A.F.i.M., J.N. and M.A. supervised the project. A.F.i.M., H.I.J., P.K. and M.H. composed the figures and wrote the manuscript. All authors discussed the results and commented on the manuscript.

Additional information

Supplementary information is available in the online version of the paper. Reprints and permissions information is available online at www.nature.com/reprints. Correspondence and requests for materials should be addressed to P.K. and A.F.i.M.

Competing financial interests

The authors declare no competing financial interests.

nature photonics

SUPPLEMENTARY INFORMATION

DOI: 10.1038/NPHOTON.2013.32

Supplementary Materials:

Single nanowire solar cells beyond the Shockley-Queisser limit

.

Peter Krogstrup[1,*], Henrik Ingerslev Jørgensen[2,*], Martin Heiss[3,*], Olivier Demichel[3], Jeppe V. Holm[2], Martin Aagesen[2], Jesper Nygard[1], Anna Fontcuberta i Morral[3,†]

[1] Nano-Science Center, Niels Bohr Institute, University of Copenhagen, Denmark

[2]SunFlake A/S, Nano-Science Center, Universitetsparken 5, DK-2100 Copenhagen, Denmark

3 Laboratoire des Matériaux Semiconducteurs, Ecole Polytechnique Fédérale de Lausanne, 1015 Lausanne, Switzerland

*equal contribution

† Corresponding Author: anna.fontcuberta-morral@epfl.ch

The supplement includes more details on:

1. Fabrication of the single nanowire solar cells
2. Measurements on another single nanowire solar cell (device 2) fabricated as device 1 with ITO top contact.
3. Measurements on two more devices (device 2 and 3) contacted with an Au-Ge-Au top contact.
4. Extraction of ideality factor and series and shunt resistor for device 1 and 2.
5. EQE measurements and calculated absorption efficiency spectra for single vertical nanowire in air and embedded in SU8 photoresist.

DOI: 10.1038/NPHOTON.2013.32

1. Fabrication of the single nanowire solar cells:

We first outline the main steps for the nanowire solar cell fabrication procedure used in this work, and which is illustrated in Fig. S1. Scanning electron micrograph (SEM) images of various steps are shown in Fig. S2:

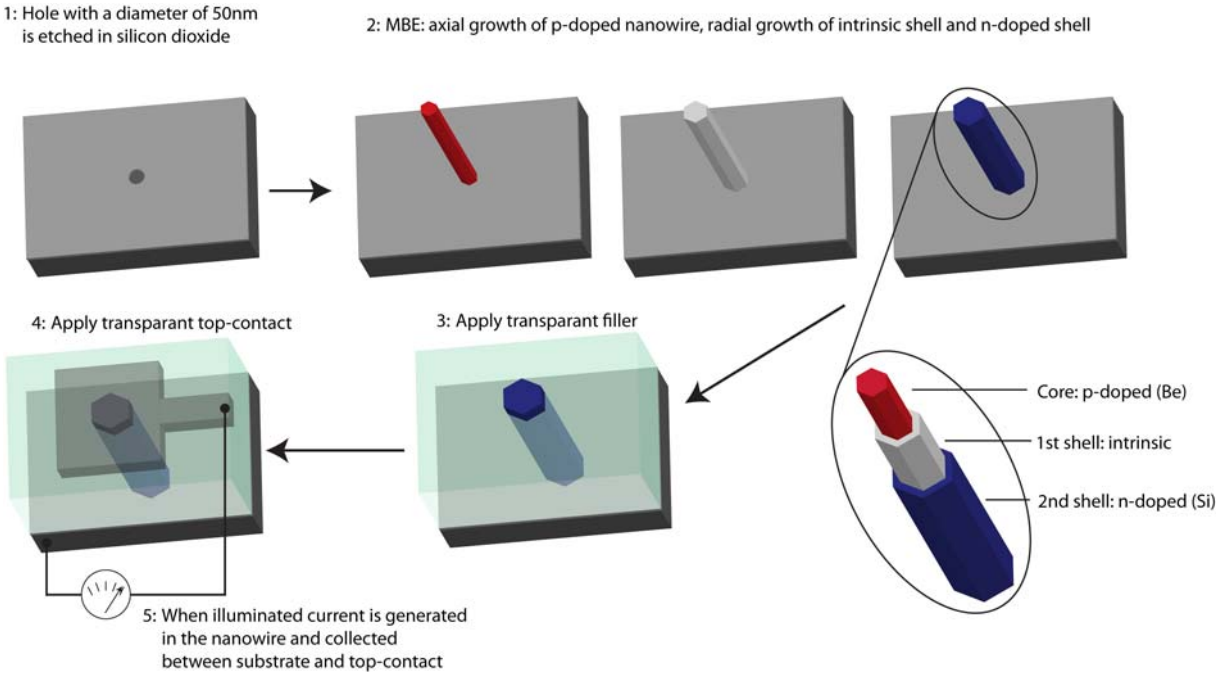

Figure S1. Sketch of the main steps of the nanowire solar cell fabrication described in detail below.

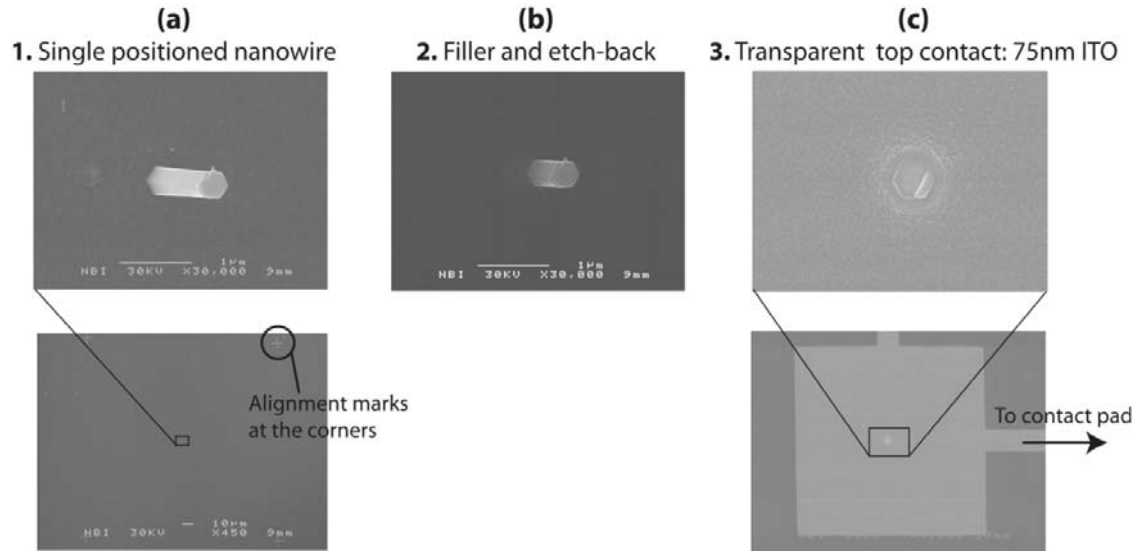

Figure S2: Fabrication of single nanowire solar cells. The SEM images in (a) and (b) are tilted 20deg and are all images are of the same device.

1) A heavily p-type doped silicon 111 substrate with a layer of 30 nm thermal SiO_2 with nanoscale holes is used to predefine positions for single GaAs nanowire growth. The holes in the oxide are defined by e-beam lithography and BHF etch and exhibit a diameter of about 50-70nm. The substrate is patterned also with larger alignment markers for the identification of the nanowires, as shown in Fig. S2 (a)
2) The GaAs nanowires are grown in a molecular beam epitaxy (MBE) chamber, where the axial core growth where grown by a 60 min Ga assisted vapor-liquid-solid growth mechanism at a temperature of $T = 630°C$. During this step the Be shutter was open (Be is a p-type dopant in GaAs). A gallium rate of $\sim 0.9\mu m/hr$ and a V-III ratio of 4 was used.
3) We finished the p-part of the cell with radial growth step at $T = 460°C$ with a corresponding planar growth rate of $\sim 0.3\mu m/hr$, and with a beam flux ratio of $V/III \sim 50$, followed by an annealing step of 10 min at 630C to inter-diffuse Be atoms into the core in order to ensure that the p-part is doped till the interface with the silicon substrate.
4) The Be flux used in the growth of the core and p-type shell corresponded to a planar nominal doping concentration of $3.5\times10^{17}\,cm^{-3}$ and $7\times10^{18}\,cm^{-3}$ for the given Ga flux.
5) Then, we continued with the growth of of an undoped and n-type shell at 460°C. The n-type doping was equivalent to a planar doping level of $7\times10^{18}\,cm^{-3}$ and had a thickness of 50 nm.
6) After crystal growth, SU-8 was spun-on the substrate at 4000rpm for 45s and cured with 1min UV light and 3min on a hotplate at 185°C. Then an etch-back with 1-3min oxygen plasma etch was performed to leave the top of the nanowire free of any filler (Fig. S2(b)).
7) The top contact was further defined by e-beam lithography. After the development the sample is etched 30s in oxygen plasma, 5-10s in BHF, and then quickly transferred (within 1min) to a high vacuum chamber for evaporation of the top contact. This is done in order to get a clean and oxide free nanowire top.
8) We have fabricated devices with Au-Ge-Au and indium-tin-oxide (ITO) as top contacts (Fig. S2(c)). Device 1 and 2 are made with 75nm ITO. The ITO is after liftoff heat treated at 185°C for 3min to obtain higher transparency. Device 3 and 4 (see Figure S4) are made with 5nmAu, 6nmGe, and 30nmAu. The Au-Ge-Au contact gives a good N-type contact. Contact to the back side of the silicon wafer is done by standard silver glue.

DOI: 10.1038/NPHOTON.2013.32

2. Measurements on another single nanowire solar cell (device 2) fabricated as device 1 with ITO top contact

Figure S3 shows measurements on a second device fabricated just as device 1 discussed in the main letter.

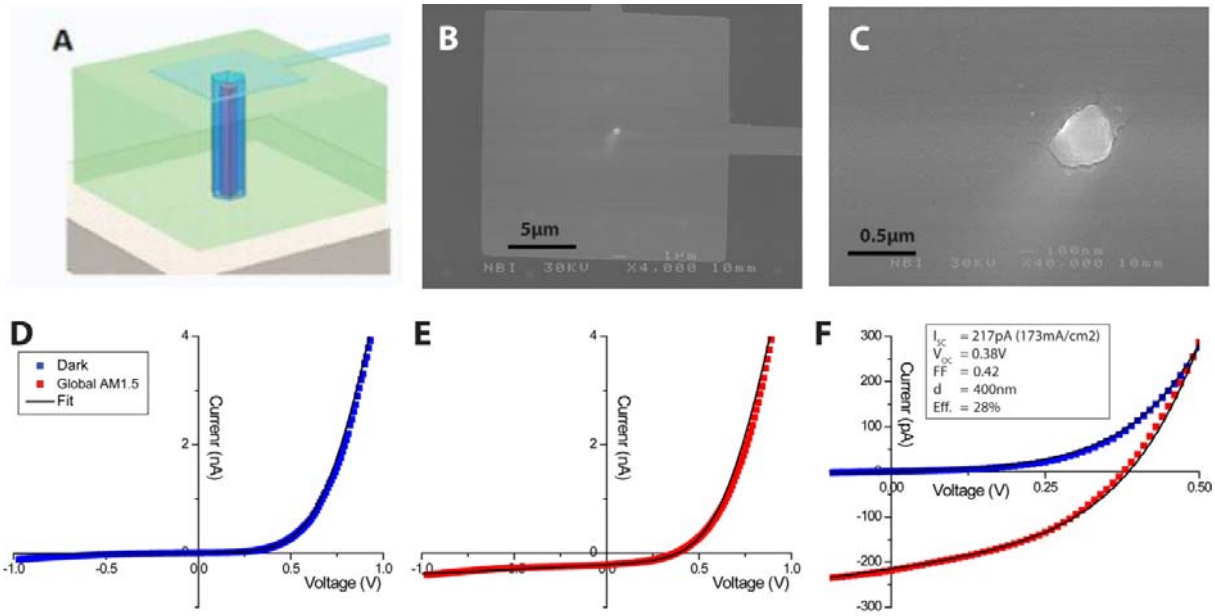

Figure S3: Electrical characterization of a single nanowire solar cell (device 2): (A) Sketch of the vertical single nanowire radial p-i-n-device. (B,C) Scanning electron micrographs of the device. The nanowire is 2µm high and has a diameter of about 400nm. (D) Current voltage characteristics of the device in the dark, (E) under globalAM1.5 illumination and (F) comparison of the device in the dark and under illumination, showing the figure of merit characteristics.

3. Measurements on two more devices (device 2 and 3) contacted with an Au-Ge-Au top contact.

Here we show measurements on two different single-wire solar cells contacted with 5nm Au, 6nm Ge, 30nm Au (device 3 and 4). Figure S4 shows I-V curves for the devices illuminated with global 1.5AM light generated with our solar generator and no light (dark). The key parameters for the devices are shown in the inserts of the middle figures: Device 3 I_{SC}=42pA, V_{OC}=0.35V, FF=0.53. Device 4 I_{SC}=43pA, V_{OC}=0.3V, FF=0.51.

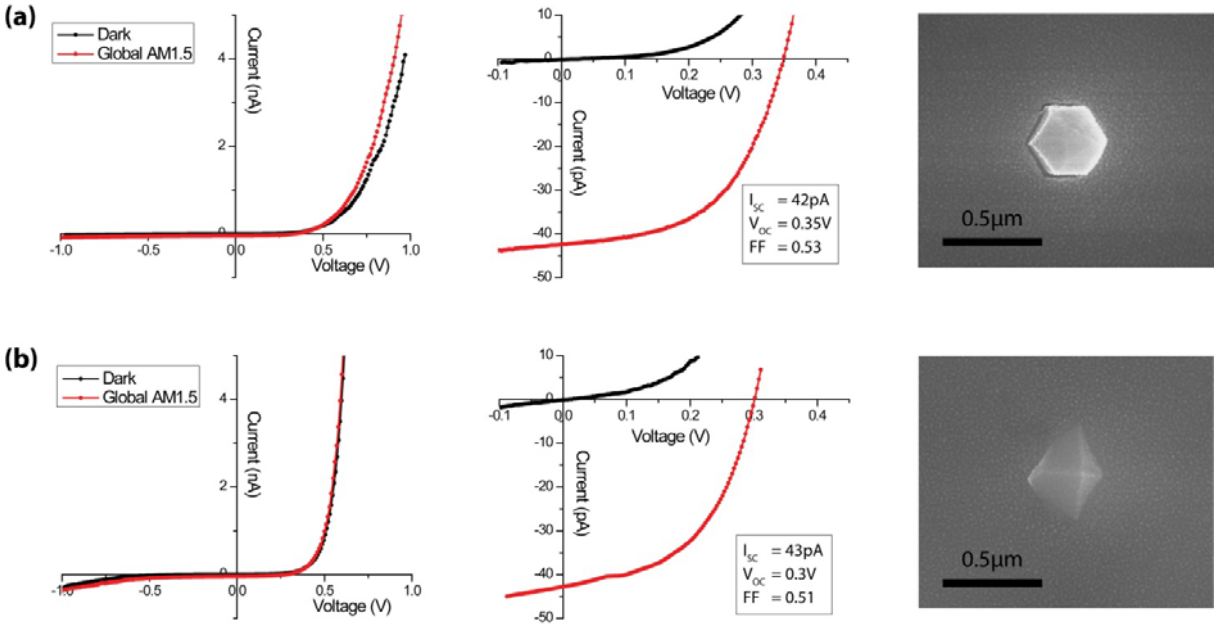

Figure S4: Electrical characterization of two single nanowire solar cells (device 3 and 4) contacted with 5nm Au, 6nm Ge, and 30nmAu, and SEM images of the top of the nanowire. (a) device 3, and (b) device 4.

These two devices have a much lower I_{SC} compared to device 1 and 2 which is what can be expected since the Au-Ge-Au top contact is much less transparent than the ITO. The V_{OC} is also lower but only slightly, probably due to the large decrease in I_{SC}.

DOI: 10.1038/NPHOTON.2013.32

4. Extraction of ideality factor and series and shunt resistor for device 1 and 2.

We extract the ideality factor, series resistor and shunt resistor of our devices by fitting their I-V curves to the model schematically shown below. It consists of a diode with ideality factor n and photo current I_{ph} and a series and shunt resistor (R_{Se}, and R_{Sh}). The source-drain current (I_{Sd}) versus source-drain voltage (V_{Sd}) can be found via a parameterization in the diode voltage (V_d) using the following three equations:

$$I_d(V_d) = I_0\left(\exp\left(\frac{eV_d}{\eta k_B T}\right) - 1\right) - I_{ph}$$

$$I_{sd}(V_d) = \frac{V_d}{R_{Sh}} + I_d(V_d)$$

$$V_{sd}(V_d) = R_{Se}\left(\frac{V_d}{R_{Sh}} + I_d(V_d)\right) + V_d$$

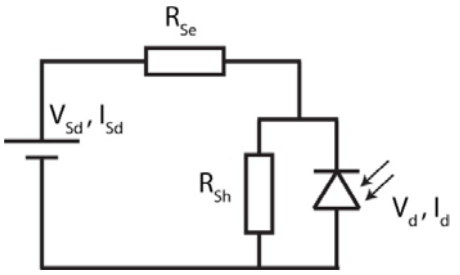

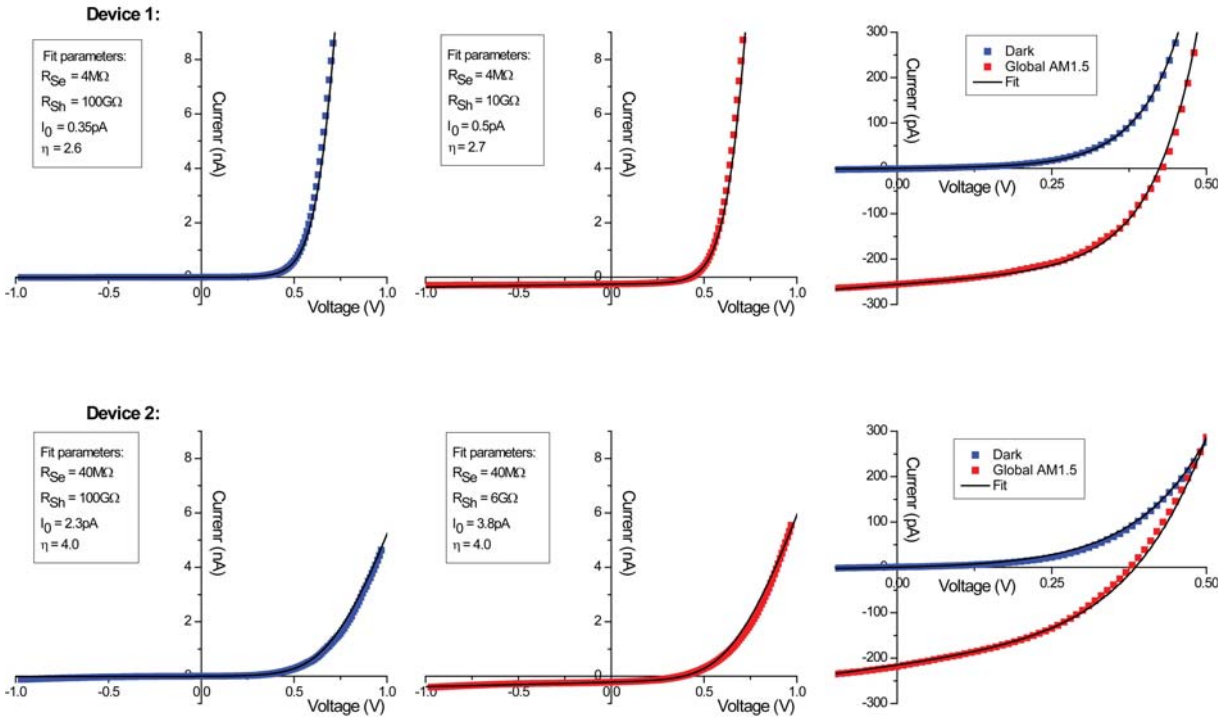

Figure S5. Measurements and fits (solid lines) of IV curves in the dark (blue squares), and illuminated by global AM1.5 light (red squares). We extracted for device 1 (2) an ideality factor of about 2.6 (4.0), and series resistances of 4MΩ (40MΩ). The shunt resistance depends on the light intensity; at no light it is 100GΩ for both devices.

5. EQE measurements and calculated absorption efficiency spectra for single vertical nanowire in air and embedded in SU8 photoresist.

The spectral response measurements were realized with a halogen lamp coupled to a grating monochromator (PI acton SP2150). The light from the monochromator exit slit was guided through a multimode optical fibre and projected to the sample by means of a microscope lens. The photocurrent was measured by a Keithley 6487 ampermeter. We calibrated the spectral power density by measuring the transmission through pinholes of known sizes (20 μm and 75 μm diameter) that are mounted at the exact position where the sample is placed for the measurements. Normalizing the measured short circuit current to the geometrically incident photon flux density we obtain apparent EQE above one as detailed in the main manuscript.
It is important to note that as expected, macroscopic photovoltaic devices (no single nanowires) measured with the same setup yield an EQE < 1.[1]

We simulate the spectra of absorption efficiency by means of Finite Difference Time Domain method using the MEEP software package. For the calculations we consider a vertical cylindrical GaAs nanowire with a length of 2000 nm and diameter of 400 nm on a silicon substrate. We perform separate calculations for a wire embedded in SU8 photoresist and one surrounded by vacuum. For this configuration the calculated absorption enhancement averaged to an incident AM1.5G spectrum is 2.86 (SU8) and 3.77 (air) respectively.

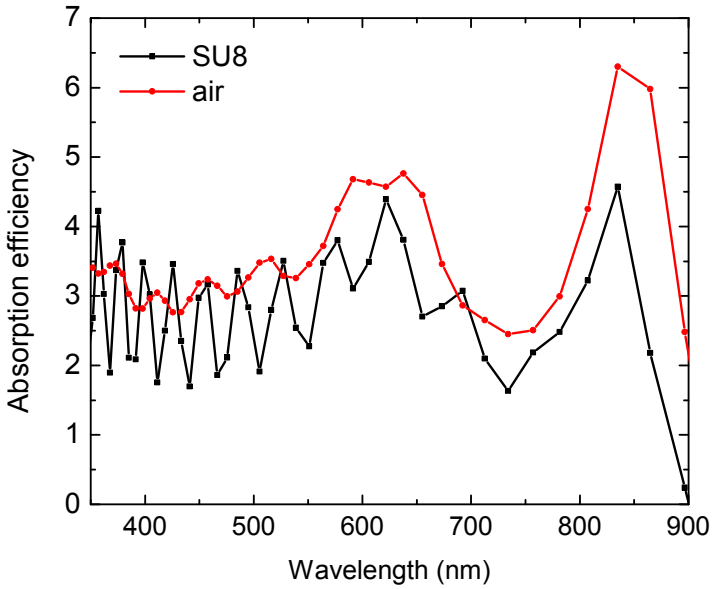

Figure S.6. Calculated absorption spectra of a standing GaAs nanowire embedded in SU8 or in air.

1. A. Dalmau Mallorquí, F. M. Epple, D. Fan, O. Demichel, A. Fontcuberta i Morral (2012), Phys. Status Solidi A.

III: Self-Catalyzed GaAsP Nanowires Grown on Silicon Substrates by Solid-Source Molecular Beam Epitaxy

Yunyan Zhang*, Martin Aagesen*, **Jeppe V. Holm**, Henrik I. Jørgensen, Jiang Wu, & Huiyun Liu

Reprinted with permission from *Nano Letters*, **13**, 3897–3902 (2013).

NANO LETTERS

Letter

pubs.acs.org/NanoLett

Self-Catalyzed GaAsP Nanowires Grown on Silicon Substrates by Solid-Source Molecular Beam Epitaxy

Yunyan Zhang,*[,†,∥] Martin Aagesen,*[,‡,§,∥] Jeppe V. Holm,[‡] Henrik I. Jørgensen,[‡] Jiang Wu,[†] and Huiyun Liu*[,†]

[†]Department of Electronic and Electrical Engineering, University College London, London WC1E 7JE, United Kingdom

[‡]SunFlake A/S, Universitetsparken 5, Copenhagen DK-2100, Denmark

[§]Gasp Solar ApS, Gregersensvej 7, Taastrup DK-2630, Denmark

ABSTRACT: We realize the growth of self-catalyzed GaAsP nanowires (NWs) on silicon (111) substrates using solid-source molecular beam epitaxy. By optimizing the V/III and P/As flux ratios, as well as the Ga flux, high-crystal-quality GaAsP NWs have been demonstrated with almost pure zinc-blende phase. Comparing the growth of GaAsP NWs with that of the conventional GaAs NWs indicates that the incorporation of P has significant effects on catalyst nucleation energy, and hence the nanowire morphology and crystal quality. In addition, the incorporation ratio of P/As between vapor−liquid−solid NW growth and the vapor−solid thin film growth has been compared, and the difference between these two growth modes is explained through growth kinetics. The vapor−solid epitaxial growth of radial GaAsP shell on core GaAsP NWs is further demonstrated with room-temperature emission at ∼710 nm. These results give valuable new information into the NW nucleation mechanisms and open up new perspectives for integrating III−V nanowire photovoltaics and visible light emitters on a silicon platform by using self-catalyzed GaAsP core−shell nanowires.

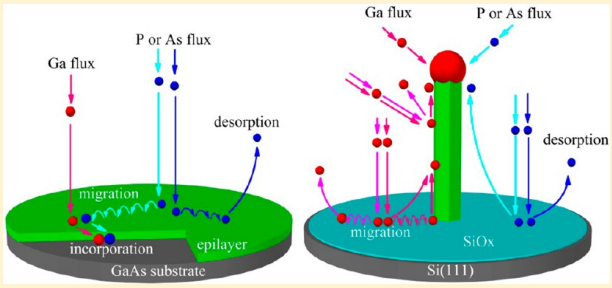

KEYWORDS: *Nanowire, GaAsP, core−shell, self-catalyzed, solid-source molecular beam epitaxy, room-temperature emission*

Ternary GaAsP is one of the most promising III−V compound semiconductors for photovoltaics (PV) and visible emitters, because the GaAsP compound band gap can be tuned between the band gaps of the two binary compounds, GaP (548 nm at 300 K) and GaAs (864 nm at 300 K), by adjusting the P content.[1] Especially, the 1.7/1.1 eV GaAsP/silicon two-junction tandem solar cell has theoretical efficiencies of 34% at 1 sun AM0 and 44% under 500 suns concentration AM1.5G.[2,3] However, the lattice and thermal expansion mismatch between GaAsP and silicon substrates have hindered the effective implementation of GaAsP for high efficiency photovoltaic cells.[4−7] In recent years, one-dimensional III−V nanowires (NWs) have gained great attention due to their unique geometries and functional properties.[8−11] Compared with thin film growth, NWs could enable straightforward integration between lattice-mismatched material systems, such as III−V compounds on silicon. The strain induced at the heterointerface between the GaAsP NWs and silicon substrates can be elastically relieved over a thickness of a few monolayers due to a small contact area and large surface-to-volume ratio,[12] which promises an ideal marriage between the high performance GaAsP optoelectronic devices and the mature low-cost, large-scale silicon microelectronic technologies. In addition, the radial core−shell NW structure allows carrier separation in the radial direction within a distance smaller than or comparable to the minority carrier diffusion length.[13,14] As a result, carriers can be effectively separated and collected with marginal recombination and hence high efficiency is expected for devices. A lot of limitations of conventional planar solar cells can be eliminated by this orthogonalized pathway for light absorption and carrier collection in nanowire solar cells.[15]

Despite all these advantages, there are great challenges in growing the ternary GaAsP nanowires on silicon substrates. In the III−V compounds, there are hexagonal wurtzite (WZ) and cubic zinc blende (ZB) structures.[16] Materials with high iconicity, such as nitrides,[17,18] tend to form the WZ phase, while materials with low iconicity, such as GaAsP, are more likely to adopt the ZB phase.[19] When the material dimension is in the nanometer scale, the WZ phase is more efficient in reducing the surface energy caused by the large surface-to-volume ratio.[16,19−21] Because of this, the GaAsP NWs with ZB phase often have lots of WZ structure defects such as twin defects, stacking faults, and ZB−WZ polytypism. These defects will degrade the material quality of GaAsP NWs and adversely impact the optical and electronic properties of III−V nanowires, for instance, by reducing the quantum efficiency, carrier lifetime, and carrier mobility.[22] Moreover, the difference

Received: May 30, 2013
Published: July 30, 2013

in the properties of As and P can also add difficulties in the control of NW growth. Consequently, there are only a few reports about the GaAsP NWs in the literature so far.[23−28] Most of these reports were carried out via the vapor−liquid−solid (VLS) growth mode with the help of Au catalyst by gas-source molecular beam epitaxy (MBE) or metalorganic chemical vapor deposition (MOCVD).[29] However, gold is a fast-diffusing metal that significantly impairs the properties of semiconductors.[30,31] Although a self-catalyzed approach for NW growth will be ideal to avoid the use of Au, the control of uniformity, composition, and morphology of NWs is still a challenge for the design of complex device structures. Solid-source MBE has its advantages in precise control of growth parameters and is more environmentally friendly compared with the gas-source MBE and MOCVD due to the lower vapor pressure and toxicity. However, there are no reports on the important growth mechanisms regarding self-catalyzed GaAsP NWs by solid-source MBE in the literature, although the good PV properties of GaAsP nanowires grown on a silicon substrate by solid-source MBE have been demonstrated recently.[28]

In this letter, we have systemically studied the VLS growth of catalyst-free GaAsP NWs and the vapor−solid (VS) epitaxial growth of their shell structure on silicon (111) substrates with different V/III ratios and Ga fluxes by a solid-source MBE. Scanning electron microscope (SEM) and transmission electron microscope (TEM) studies show that GaAsP NWs under optimized growth conditions have a uniform diameter along the whole NW length and almost pure ZB crystal with only a few defects. The content of P in GaAsP NWs was studied as a function of source flux ratio with the help of energy-dispersive X-ray spectroscopy (EDX). A good composition control of NWs with P content ranging from 10 to 75% has been achieved by adjusting the P/As flux ratio. After the core NW growth, a high-crystal-quality GaAsP shell with room-temperature emission was demonstrated under the VS epitaxial growth mode.

GaAsP NWs were fabricated by a solid-source MBE with a solid Ga source and As_4 and P_2 cracker cells. 380 μm thick B-doped silicon (111) substrates were used in the experiments. The silicon (111) substrates were annealed at 640 °C for 5−8 min before the NW growth. The core NW growth started with the assistance of Ga droplets that formed on the silicon surface during the first few seconds of the growth procedure. To grow GaAsP NWs, Ga and As sources were supplied first for 5 min, resulting in the growth of phosphorus-free nucleation nanostems. Phosphorus was subsequently introduced to perform the GaAsP NW growth on the GaAs nanostems. If not particularly indicated, the NW growths were performed at a substrate temperature ranging between 620 and 650 °C measured by a pyrometer. The Ga flux and the V/III flux ratio were varied between growths but kept within the range of 4×10^{-8} to 9×10^{-8} Torr and 40−80, respectively.

The growth of GaAsP NWs is first compared with that of conventional GaAs NWs. Figure 1 shows GaAs and GaAsP NWs grown under the optimized V/III flux ratio of 122 for GaAs NWs. The only difference between them is that the group V flux has 50% P flux for the GaAsP growth. Long and thin GaAs NWs have been observed in Figure 1a, while there are only some thick and short GaAsP pillars in Figure 1b. Therefore, it was probably not a droplet assisted growth for GaAsP under this V/III ratio and P/As flux ratio but was instead driven by the same kind of surface energy anisotropy, with GaAsP growth on preferred crystal orientations, as

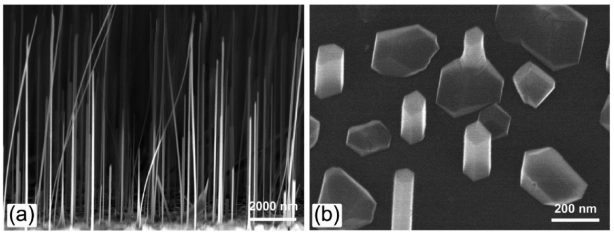

Figure 1. SEM images of (a) GaAs NWs grown with a V/III ratio of 122 and (b) GaAsP pillars grown with a V/III flux ratio of 122 and P/As flux ratio of 1.

selective area MOVPE growth.[32,33] This suggests that the nucleation rate of GaAsP increases so dramatically that no Ga droplets can form at the beginning of the growth, or that any formed droplet was quickly consumed, when half of the As flux was replaced by the P flux. This clearly indicates the growth of GaAsP NWs is significantly different from that of GaAs NWs.

To get a suitable nucleation rate of GaAsP for NW growth, the morphology of GaAsP nanostructures is first studied by varying the V/III ratios from 50 to 100 while keeping a constant Ga flux of 8.72×10^{-8} Torr, as shown in Figure 2. When the V/III flux ratio is 50, the diameter is homogeneous over the whole length (Figure 2a). At this V/III flux ratio, the replenishment and consumption of Ga in the droplets can lead to a dynamical steady state so as to maintain a constant Ga droplet size over the nanowire length. As the droplet defines the boundary where nanowire growth occurs,[16,34,35] the NWs on this sample show a very uniform diameter along the whole NW length. When the V/III flux ratio is increased to 75, all the NWs exhibit a tapered shape, which is caused by the shrinkage of Ga droplets (Figure 2b). In this case, the balance of the optimum growth environment got disturbed because of the enhanced nucleation rate which is governed by the chemical potential of the elements in the liquid droplet which increases with the V/III ratio.[36,37] The consumption of Ga in the droplets at a high V/III flux ratio is so fast that the Ga source cannot provide enough replenishment, causing the shrinkage of the droplet during the growth and an increase in VS growth on the lower NW facets. Further increasing the V/III flux ratio to 100, the droplets can only survive for a very short time and the VLS process is terminated rapidly because of the consumption of the droplets. As a result, only some cone-shaped nanobuds have been observed in Figure 2c.

The Ga flux is another important parameter, which plays an important role on the growth of self-catalyzed GaAsP nanowires. GaAsP NWs were thus studied by varying the Ga flux from 4.62×10^{-8} to 8.72×10^{-8} Torr with a constant V/III flux ratio of 50 and a P/As flux ratio of ∼0.14. It is interesting to see that these three samples shown in Figure 3 have a similar morphology. A majority of the NWs stand vertically on the substrate without measurable tapering. There is a round Ga droplet on the tip of each NW. The NW density increases with the Ga flux. This could be explained by an increased nucleation at higher Ga flux, which provides more Ga droplets for NW growth.

The structural properties of GaAsP NWs were further studied by TEM. Figure 4a shows TEM images of NWs from the sample in Figure 3b. Here, it should be noted that the structural properties of NWs obtained from TEM measurements of all these samples displayed in Figure 3 are similar. As shown in Figure 4a, the NW has a uniform diameter along its

dx.doi.org/10.1021/nl401981u | Nano Lett. 2013, 13, 3897−3902

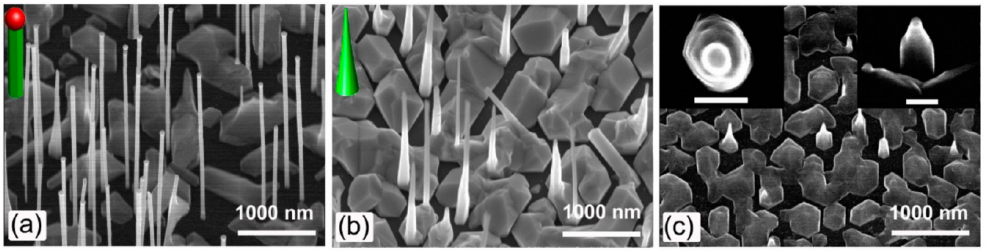

Figure 2. SEM images (tilt angle = 25°) of GaAsP NWs with the same Ga flux (8.72×10^{-8} Torr) and P/As flux ratio (~0.14) but different V/III ratios: (a) V/III = 50, (b) V/III = 75, (c) V/III = 100. The insets in parts a and b show the illustrations of NW shapes. The insets in part c show the top view and side view of one nanobud. The scale bars in the insets of part c are 100 nm.

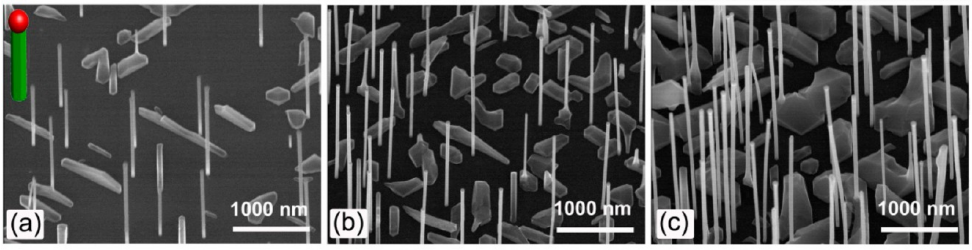

Figure 3. SEM images (tilt angle = 25°) of GaAsP NWs with the same V/III ratios (50) and P/As flux ratio (~0.14) but different Ga flux: (a) Ga = 4.62×10^{-8} Torr, (b) Ga = 6.78×10^{-8} Torr, (c) Ga = 8.72×10^{-8} Torr. The inset in part a shows the illustrations of NW shape of these three samples.

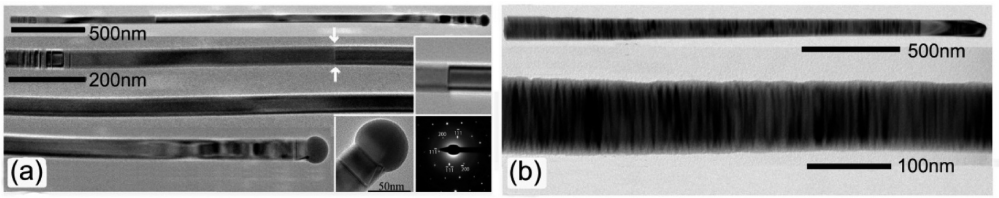

Figure 4. (a) TEM images of the overall and section views of NW with Ga flux of 6.78×10^{-8} Torr and V/III flux ratio of 50. Three insets in part a show the NW tip, the twin plane indicated by white arrows, and the electron diffraction pattern from the middle defect free location, respectively. (b) TEM images of the overall and section views of GaAsP NW with Ga flux of 8.72×10^{-8} Torr and V/III flux ratio of 75.

entire length. There are only a few defects at the bottom and top parts of the NW. The defects at the bottom, in the form of twins or WZ crystal segments, are caused by the unoptimized GaAs stem. These defects could be eliminated by optimizing the growth parameters of GaAs stems. The defects at the tip of the NW may be caused by the depletion of group V sources at the end of NW growth.[19,35,38] The middle part of the NW is almost defect-free except a few single twin planes which are indicated by the white arrows. The electron diffraction pattern from the defect-free part verifies that the NW is the ZB crystal structure. At the tip of the NW, there is a round Ga droplet which clearly shows that the NW growth adopts the Ga-assisted VLS mode. Figure 4b shows an example of the NW from the Figure 2b sample with a V/III flux ratio of 75 during the growth. It is apparent that there are a large number of defects in the NW. This may be due to the increased group V element saturation level and chemical potential in the droplets, which facilitates the formation of WZ structure in the NW during the growth.[8,16,21,37] According to Krogstrup et al., the relative nucleation probability of WZ and ZB structures can be influenced by reshaping the droplet with high V/III flux ratio for GaAsP NWs, which leads to the formation of defects.[35] Several growths with different V/III flux ratio (70, 75, 80, and 100) and different Ga flux (6.78×10^{-8} and 8.72×10^{-8} Torr) were also carried out. These samples might have some differences from each other, but they have one common feature, which is the large amount of defects in the NWs. All these suggest that, when the V/III flux ratio is higher than 50, the morphology and the crystal quality of GaAsP NWs deteriorate drastically.

All the above results suggest that the V/III flux ratio plays a more important role than Ga flux in the morphology and structural quality of GaAsP NWs. In general, the V/III flux ratio controls the Ga consumption in the droplets, and as we will show, the P/As ratio appears to be at least as important. With an optimized V/III flux ratio, the Ga droplet size and the group V element saturation level in the droplet can be maintained constant during the growth. As a result, the GaAsP NW can keep a uniform diameter and good crystal quality along its entire length.

The control of NW material composition is another important factor for the construction of various devices. In order to investigate the incorporation ratio of P/As so as to obtain the correlation between the P content in the NW and the P flux ratio, GaAsP NWs were grown with different P/(P + As) flux ratios of 7.2, 10, 20, 30, 40, and 50%. The percentages of P within GaAsP NWs, obtained by EDX measurement, are shown in Figure 5. Here, we define the P flux ratio as

dx.doi.org/10.1021/nl401981u | *Nano Lett.* 2013, 13, 3897−3902

$$x = \frac{F(\mathrm{P})}{F(\mathrm{P}) + F(\mathrm{As})} \quad (1)$$

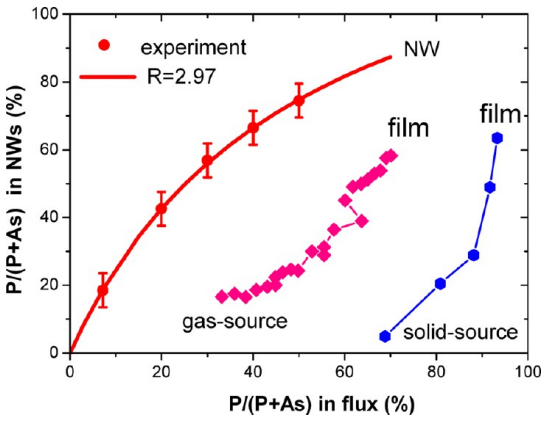

Figure 5. P content in NWs as a function of P/(P + As) beam flux ratio. The red dots show the experimental results, and the red line indicates the fitted result. The blue and pink dots show the planar GaAsP film growth by solid-source[39] and gas-source MBE,[41] respectively.

where $F(\mathrm{P})$ and $F(\mathrm{As})$ are the flux pressures of P and As, respectively. The P content, P/(P + As), in the NW can be described by the following equation:

$$\mathrm{P}\% = \frac{\beta x}{\beta x + \alpha(1 - x)} \quad (2)$$

where β and α are the incorporation coefficients of P and As, respectively. We define the incorporation ratio of P/As as $R = \beta/\alpha$, and eq 2 can be expressed as

$$\mathrm{P}\% = \frac{Rx}{Rx + (1 - x)} = \frac{Rx}{1 + (R - 1)x} \quad (3)$$

When R is 2.97, eq 3 fits well with the experimental results, as shown in Figure 5. The fitting links the P flux ratio to P content in the NW ranges from 10 to 75%, which is of great use in the control of the NW composition. The fitting also indicates that the P incorporation coefficient in NWs is about 2 times higher than that of As in the VLS growth of NWs. This is quite different from the planar epitaxial growth in which As has preferential incorporation into the epitaxial layer grown by gas-source or solid-source MBE.[39−41] The schematic illustration of the film and the NW growth model by MBE can be seen in Figure 6. In the VS epitaxial growth mode, the growth is under group V rich conditions and the growth rate is controlled by group III, such as Ga. If the group V adatoms are unable to meet the group III adatoms, they cannot incorporate into the lattice and will desorb from the substrate surface back into the vapor. Although P has a higher chemical activity than that of As,[42,43] its incorporation coefficient is lower because As adatoms have a larger sticking coefficient and hence longer surface lifetime and migration length than those of P adatoms, which increase the As adatoms' chance of meeting Ga adatoms and incorporating into the lattice.[39,41,44] By contrast, NWs are grown via the VLS growth mode, which is under a group III rich environment. The growth is group V element limited, and the incorporation ratio of P/As is nucleation determined. The effect of using P in Au-catalyzed GaP nanowire growth has been

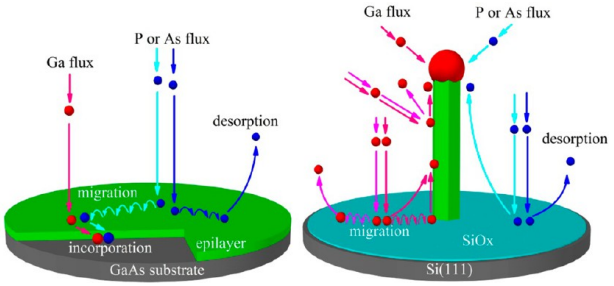

Figure 6. Schematic illustration of the MBE growth model for the thin film via vapor−solid epitaxial growth mode and the NW via vapor−liquid−solid mode.

modeled theoretically and shown to result in a higher chemical potential in the catalyst particle than that for GaAs growth.[37] This modeling also suggests that As atoms will be favored above the P atoms in catalyzed GaAsP growth, since the inclusion of As atoms in the catalyst will require a smaller increase in chemical potential of the catalyst. These results presented here however demonstrate that the extra increase in catalyst chemical potential does not prohibit P atoms from being absorbed in the catalyst. The results also show that the higher chemical potential of the catalyst, created by the absorbed P atoms, results in a much higher nucleation rate of GaP relative to GaAs. Therefore, the incorporation ratio of P/As is controlled by the physical property of P and As for the planar film growth and by the chemical property of P and As for the NW growth.

In order to further study the effect of P on NW structural properties, TEM measurement was performed with GaAsP NWs with an increasing percentage of P along the NW growth direction, as shown in Figure 7. The NW is defect free at low

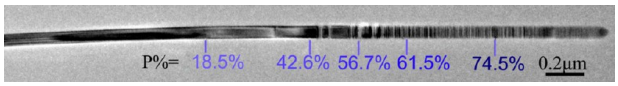

Figure 7. TEM image of one NW with different P% along the NW length.

percentages of P, but the defect density increases with the percentage of P in the NW. When the As flux is gradually replaced by P flux, the nucleation rate, which is governed by the chemical potential of the elements in the liquid droplet,[36,37] is accelerated due to a higher chemical potential in the droplet when P is added compared with that of only As.[37] This will reshape the droplet and change the relative nucleation probability of WZ and ZB structures.[35] The increase in chemical potential in the droplet can therefore promote the formation of WZ structure.[37] This could be the reason why there are dense defects at the part of the NW with a high percentage of P. These defects could be eliminated by optimizing the V/III flux ratio, which has been discussed above for a P/As flux ratio of ∼0.14.

The growth of shells on core NWs is another crucial step to achieve radial composition and doping modulation in NW structures which will enable the design of complex optoelectronic devices.[11] The growth of a GaAsP shell was further developed in this work. Following core-NW growth, the Ga shutter was closed while keeping the group V fluxes to consume the Ga droplets, which will stop axial growth. After that, the GaAsP shell is grown around the as-grown NWs by the VS

dx.doi.org/10.1021/nl401981u | Nano Lett. 2013, 13, 3897−3902

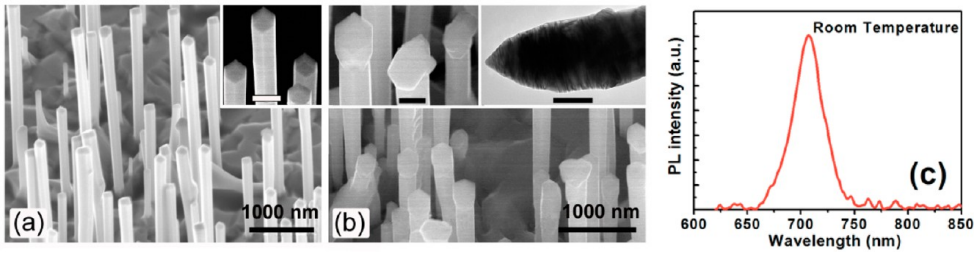

Figure 8. SEM figures of core−shell NWs grown with Ga flux of (a) 8.72×10^{-8} Torr, tilt angle = 45°, and (b) 2.77×10^{-7} Torr, tilt angle = 25°. The inset in part a shows the tip of some NWs. The scale bar in the inset in part a is 200 nm. The insets in part b show the SEM and TEM images of some NW tips. The scale bars in the insets of part b are 200 nm. (c) Photoluminescence spectrum measured for the core−shell NWs shown in part a.

epitaxial growth mode. X-ray diffraction was used for adjusting the shell composition to ensure lattice matching to the core wire. For the ideal core−shell NW, the peak intensities from the GaAsP core and shell should be at the same angle.[28] Two shell growths, on two identical as-grown core NWs at a growth temperature of about 500 °C, were carried out with a Ga flux of 8.72×10^{-8} and 2.77×10^{-7} Torr, respectively. As shown in Figure 8a, the sample with lower Ga flux has a much better morphology. Core−shell NWs on this sample show very clean hexagonal tips and uniform diameter along the whole NW. By contrast, NWs grown under higher Ga flux, shown in Figure 8b, have much more extra deposition at the tips, looking like matchsticks. The effusion cells in the MBE system are angled 33° relative to the substrate normal. This large angle makes the side facets suffer from a shadow effect caused by neighboring NWs blocking the source beams. In this case, the tip of NWs can get much more source supply. When the NW shell is grown under a lower Ga flux, Ga adatoms have a longer diffusion length, which is beneficial for uniform VS growth and gives a better shell morphology, as shown in Figure 8a. When the deposition rate is high during the shell deposition, Ga adatoms do not have a high enough diffusion length to get enough migration before they are incorporated into the lattice. As a result, the shell growth at the tip is much faster and a lot of defects are formed at this part, as can be seen in the insets in Figure 8b. Therefore, a slow growth rate is very important in the shell growth because adatoms need much more time to get a uniform distribution compared to planar film growth. These results indicate, although both the planar film epitaxy and the NW shell growth adopt the VS growth mode, there is a significant difference between them.

We characterized the optical properties of core−shell GaAsP nanowires using photoluminescence (PL) spectroscopy. PL measurements were obtained under 532 nm excitation from a diode-pumped solid-state laser. A 0.25 m monochromator was used to disperse the PL spectra, which were then detected by a TE-cooled Ge detector. The room-temperature PL spectrum shown in Figure 8c is obtained from the core−shell GaAsP NW sample shown in Figure 8a. Its peak emission intensity is around 710 nm with a full width at half-maximum of about 33 nm. The room-temperature emission from GaAsP NWs without any surface-passivated layers reveals a good crystal quality of NWs.[45,46]

In summary, the growth of high-quality, self-catalyzed GaAsP NWs as well as the core−shell structure on silicon (111) substrates by solid-source MBE have been demonstrated. In the core-NW growth, both the V/III and P/As flux ratios play important roles in the NW morphology and crystal quality. By optimizing the P/As and V/III flux ratios, all the NWs with different Ga fluxes show a uniform diameter along the whole NW length and an almost pure ZB phase with only a few defects. Through studying the incorporation as a function of source flux ratios, the incorporation of P is identified as ~2 times higher than that of As at the nanowire growth temperature used in this study. In the NW shell growth, a low Ga flux is required to ensure a sufficient adatom diffusion length in order to obtain a uniform shell growth. The optimized core−shell NWs show regular shape with room-temperature emission. The results not only demonstrate the feasibility in growing GaAsP NWs by solid-source MBE but also open up new perspectives for nanowire photovoltaics and visible light emitters on silicon substrates by using self-catalyzed GaAsP core−shell nanowires.

AUTHOR INFORMATION

Corresponding Author

*E-mail: yunyan.zhang.11@ucl.ac.uk (Y.Z.), martin.aagesen@gaspsolar.com (M.A.), huiyun.liu@ucl.ac.uk (H.L.).

Author Contributions

‖Y.Z., M.A.: These authors contributed equally to this work.

Notes

The authors declare no competing financial interest.

REFERENCES

(1) Vurgaftman, I.; Meyer, J. R.; Ram-Mohan, L. R. *J. Appl. Phys.* **2001**, *89*, 5815.
(2) LaPierre, R. R. *J. Appl. Phys.* **2011**, *110*, 014310.
(3) Geisz, J. F.; Friedman, D. J. *Semicond. Sci. Technol.* **2002**, *17*, 769.
(4) Geisz, J. F.; Olson, J. M.; Romero, M. J.; Jiang, C. S.; Norman, A. G. In *Lattice-mismatched GaAsP solar cells grown on silicon by OMVPE*, Photovoltaic Energy Conversion, Conference Record of the 2006 IEEE 4th World Conference on, 2006; IEEE: pp 772−775.
(5) Demeester, P.; Ackaert, A.; Coudenys, G.; Moerman, I.; Buydens, L.; Pollentier, I.; Van Daele, P. *Prog. Cryst. Growth Charact. Mater.* **1991**, *22*, 53.
(6) Dupuy, M.; Lafeuille, D. *J. Cryst. Growth* **1975**, *31*, 244.
(7) Watkins, G. D. In *Lattice defects in semiconductors 1974*, Inst. Phys. Conf. Ser, 1975; p 1.
(8) Gudiksen, M. S.; Lauhon, L. J.; Wang, J.; Smith, D. C.; Lieber, C. M. *Nature* **2002**, *415*, 617.
(9) Lauhon, L. J.; Gudiksen, M. S.; Wang, D.; Lieber, C. M. *Nature* **2002**, *420*, 57.
(10) Samuelson, L. *Mater. Today* **2003**, *6*, 22.
(11) Li, Y.; Qian, F.; Xiang, J.; Lieber, C. M. *Mater. Today* **2006**, *9*, 18.
(12) Joyce, H. J.; Gao, Q.; Hoe Tan, H.; Jagadish, C.; Kim, Y.; Zou, J.; Smith, L. M.; Jackson, H. E.; Yarrison-Rice, J. M.; Parkinson, P. *Prog. Quantum Electron.* **2011**, *35*, 23.

(13) Kayes, B. M.; Atwater, H. A.; Lewis, N. S. *J. Appl. Phys.* **2005**, *97*, 114302.
(14) Lewis, N. S. *Science* **2007**, *315*, 798.
(15) Tian, B.; Kempa, T. J.; Lieber, C. M. *Chem. Soc. Rev.* **2009**, *38*, 16.
(16) Glas, F.; Harmand, J.-C.; Patriarche, G. *Phys. Rev. Lett.* **2007**, *99*, 146101.
(17) Abu-Farsakh, H.; Qteish, A. *Phys. Rev. B* **2007**, *75*, 085201.
(18) Christensen, N. E.; Satpathy, S.; Pawlowska, Z. *Phys. Rev. B* **1987**, *36*, 1032.
(19) Dick, K. A.; Caroff, P.; Bolinsson, J.; Messing, M. E.; Johansson, J.; Deppert, K.; Wallenberg, L. R.; Samuelson, L. *Semicond. Sci. Technol.* **2010**, *25*, 024009.
(20) Johansson, J.; Dick, K. A.; Caroff, P.; Messing, M. E.; Bolinsson, J.; Deppert, K.; Samuelson, L. *J. Phys. Chem. C* **2010**, *114*, 3837.
(21) Yamashita, T.; Akiyama, T.; Nakamura, K.; Ito, T. *Phys. E (Amsterdam, Neth.)* **2010**, *42*, 2727.
(22) Woo, R. L.; Xiao, R.; Kobayashi, Y.; Gao, L.; Goel, N.; Hudait, M. K.; Mallouk, T. E.; Hicks, R. F. *Nano Lett.* **2008**, *8*, 4664.
(23) Mohseni, P. K.; Rodrigues, A. D.; Galzerani, J. C.; Pusep, Y. A.; LaPierre, R. R. *J. Appl. Phys.* **2009**, *106*, 124306.
(24) Tchernycheva, M.; Rigutti, L.; Jacopin, G.; de Luna Bugallo, A.; Lavenus, P.; Julien, F. H.; Timofeeva, M.; Bouravleuv, A. D.; Cirlin, G. E; Dhaka, V. *Nanotechnology* **2012**, *23*, 265402.
(25) Mohseni, P. K.; LaPierre, R. R. *Nanotechnology* **2009**, *20*, 025610.
(26) Mohseni, P. K.; Maunders, C.; Botton, G. A.; LaPierre, R. R. *Nanotechnology* **2007**, *18*, 445304.
(27) Svensson, C. P. T.; Seifert, W.; Larsson, M. W.; Wallenberg, L. R.; Stangl, J.; Bauer, G.; Samuelson, L. *Nanotechnology* **2005**, *16*, 936.
(28) Holm, J. V.; Jørgensen, H. I.; Krogstrup, P.; Nygård, J.; Liu, H.; Aagesen, M. *Nat. Commun.* **2013**, *4*, 1498.
(29) Wagner, R. S.; Ellis, W. C. *Appl. Phys. Lett.* **1964**, *4*, 89.
(30) Breuer, S.; Pfüller, C.; Flissikowski, T.; Brandt, O.; Grahn, H. T.; Geelhaar, L.; Riechert, H. *Nano Lett.* **2011**, *11*, 1276.
(31) Bar-Sadan, M.; Barthel, J.; Shtrikman, H.; Houben, L. *Nano Lett.* **2012**, *12*, 2352.
(32) Hua, B.; Motohisa, J.; Kobayashi, Y.; Hara, S.; Fukui, T. *Nano Lett.* **2009**, *9*, 112.
(33) Hertenberger, S.; Rudolph, D.; Bichler, M.; Finley, J. J.; Abstreiter, G.; Koblmuller, G. *J. Appl. Phys.* **2010**, *108*, 114316.
(34) Wacaser, B. A.; Dick, K. A.; Johansson, J.; Borgström, M. T.; Deppert, K.; Samuelson, L. *Adv. Mater.* **2009**, *21*, 153.
(35) Krogstrup, P.; Curiotto, S.; Johnson, E.; Aagesen, M.; Nygård, J.; Chatain, D. *Phys. Rev. Lett.* **2011**, *106*, 125505.
(36) Markov, I. V.; Markov, I. V. *Crystal growth for beginners: fundamentals of nucleation, crystal growth and epitaxy*; World Scientific: Singapore, 2003.
(37) Glas, F. *J. Appl. Phys.* **2010**, *108*, 073506.
(38) Joyce, H. J.; Wong-Leung, J.; Gao, Q.; Tan, H. H.; Jagadish, C. *Nano Lett.* **2010**, *10*, 908.
(39) Shu-Dong, W.; Li-Wei, G.; Wen-Xin, W.; Zhi-Hua, L.; Ping-Juan, N.; Qi, H.; Jun-Ming, Z. *Chin. Phys. Lett.* **2005**, *22*, 960.
(40) LaPierre, R. R.; Robinson, B. J.; Thompson, D. A. *J. Appl. Phys.* **1996**, *79*, 3021.
(41) Hou, H. Q; Liang, B. W.; Chin, T. P.; Tu, C. W. *Appl. Phys. Lett.* **1991**, *59*, 292.
(42) Vasil'ev, V. P.; Gachon, J.-C. *Inorg. Mater.* **2006**, *42*, 1176.
(43) Van Vechten, J. A. *J. Electrochem. Soc.* **1975**, *122*, 423.
(44) Matsushima, Y.; Gonda, S.-i. *Jpn. J. Appl. Phys.* **1976**, *15*, 2093.
(45) Couto, O., Jr.; Sercombe, D.; Puebla, J.; Otubo, L.; Luxmoore, I. J.; Sich, M.; Elliott, T. J.; Chekhovich, E. A.; Wilson, L. R.; Skolnick, M. S. *Nano Lett.* **2012**, *12*, 5269.
(46) Titova, L. V.; Hoang, T. B.; Jackson, H. E.; Smith, L. M.; Yarrison-Rice, J. M.; Kim, Y.; Joyce, H. J; Tan, H. H.; Jagadish, C. *Appl. Phys. Lett.* **2006**, *89*, 173126.